

Finite-size effects and spin-orbit coupling in low-dimensional systems

Von der Fakultät für Mathematik und Physik
der Gottfried Wilhelm Leibniz Universität Hannover
zur Erlangung des Grades

Doktor der Naturwissenschaften

Dr. rer. nat.

genehmigte Dissertation

von

M. Sc. Monika Quentin geb. Jäger

2019

Referent: Prof. Dr. Christoph Tegenkamp (Leibniz Universität Hannover, Germany)
Korreferent: Prof. Dr. Harold Zandvliet (University of Twente, Enschede, Netherlands)
Korreferent: Prof. Dr. Herbert Pfnür (Leibniz Universität Hannover, Germany)

Tag der Promotion: 23.08.2019

Keywords: atomic wires, spin-orbit coupling, metal-insulator transition
Schlagworte: atomare Drähte, Spin-Bahn-Wechselwirkung, Metall-Isolator Übergang

Abstract

Materials with reduced dimensionalities, such as 2D and quasi-1D systems, are associated with a variety of instabilities accompanied by a wealth of phase transitions. This thesis treats four systems, each consisting of a metal layer evaporated on a silicon substrate, which reversely undergoes a metal-insulator transition depending on temperature. It is often caused by the interplay between electronic correlation effects and spin-orbit coupling in these systems. Besides, spatial confinement is able to tune both SOC strength and the phase transition temperature or it even leads to a suppression of the insulating phase.

For the (4×1) -In reconstruction on Si(111), it is found that the critical temperature of its Peierls-like phase transition is significantly affected by confinement due to surface steps. Transport experiments point towards destabilization of the low-temperature (8×2) phase in the vicinity of step edges, which lowers the phase transition temperature upon heating. During cooling the (8×2) phase nucleates inside the (4×1) domains, thus the critical temperature decreases only for a sufficiently high density of steps, i.e., with merely three (4×1) chains per terrace.

The α -Sn reconstruction on Si(111) is a prototype system for a two-dimensional Mott phase. By means of spin-resolved photoemission experiments, the spin-structure of the electronically correlated insulating surface state was explored in detail. The analysis of the spin-integrated bands, as well as the spin-texture of the surface state along different crystallographic directions, provide clear evidence for the formation of collinear antiferromagnetic $(2\sqrt{3} \times \sqrt{3})$ domains, while the Sn reconstruction structurally reveals a $(\sqrt{3} \times \sqrt{3})$ symmetry. The Rashba-splitting of the highest occupied Mott state was found to be $\Delta k = 0.05 \text{ \AA}^{-1}$, i.e., the α -Sn phase should rather be termed a weakly spin-orbit coupled Mott system.

In order to investigate finite-size effects such an electronically correlated system, a detailed feasibility study was done on the growth of Sn nanowires on Si(557). Depending on the Sn submonolayer coverage, various Sn-nanowires were identified. For Sn-coverages above 0.5 ML, $(\sqrt{3} \times \sqrt{3})$ and $(2\sqrt{3} \times 2\sqrt{3})$ reconstructions were found. In particular, these phases cover extended (111)-areas, thus leading to an inhomogeneous refacetting of the Si(557) surface. The (223) facets between the (111) terraces reveal structures, which resemble a $\times 2$ reconstruction along the edges. The initial step structure of the Si(557) surface is maintained for Sn-coverages below 0.5 ML, showing the α -Sn phase on 3 nm wide (111)-terraces. In contrast to the 2D Mott state of α -Sn/Si(111), this confinement quenches the correlated electronic phase yielding metallic surface states at 40 K, as seen by photoemission.

Furthermore, the low-temperature spin-orbit density phase of Pb on Si(557) was investigated, where the surface orientation is well-known to change to local (223) facets separated by (111) terraces yielding in a nesting condition of the Fermi wavevector in the direction across the nanowires. Structural models are proposed based on high-resolution scanning tunneling microscopy images. Concerning the nanowires, spectroscopic data allowed the determination of the insulating gap size induced by the formation of a spin-orbit density wave below 78 K. Evaporation of surplus Pb atoms up to 0.2 monolayers adds an extra row of Pb atoms on the mini-(111) terraces in addition to the filling up of the step edge adsorption sites. These atoms induce a metallic state located at the step edge at low temperature. The insulating phase completely collapses as a second Pb layer is added on the nanowires.

Acronyms

1D	One-dimensional
2D	Two-dimensional
2pp	Two-point probe
4pp	Four-point probe
ARPES	Angle-resolved photoemission spectroscopy
BC	Bandwidth controlled
BCS	Bardeen-Cooper-Schrieffer
CDW	Charge density wave
CEM	Constant energy map
COPHEE	Complete Photoemission Experiment
DCA	Dynamical cluster approximation
DFT	Density functional theory
DOS	Density of states
EDC	Energy distribution curve
FC	Filling controlled
FFT	Fast Fourier transformation
FIM	Field ion microscope
HSE	Heyd-Scuseria-Ernzerhof
LDA	Local density approximation
LDOS	Local density of states
LEED	Low energy electron diffraction
LHB	Lower Hubbard band
LHe	Liquid Helium
LN₂	Liquid Nitrogen
LT	Low temperature
LT-STM	Low temperature STM
MDC	Momentum distribution curve
MIT	Metal-insulator transition
ML	Monolayer
QPP	Quasi-particle peak
RT	Room temperature
SARPES	Spin- and angle-resolved photoemission spectroscopy

SBZ	Surface Brillouin zone
SCL	Space charge layer
SDW	Spin density wave
SEM	Scanning electron microscope
SIC	Striped incommensurate
SIS	Surface and interface spectroscopy
SOC	Spin-orbit coupling
SODW	Spin-orbit density wave
SPALEED	Spot profile analysis low energy electron diffraction
STM	Scanning tunneling microscope
STS	Scanning tunneling spectroscopy
UHB	Upper Hubbard band
UHV	Ultra-high vacuum
VT-STM	Variable temperature STM
XPS	X-ray photoemission spectroscopy

List of symbols

2Δ	Band gap
α	Rashba parameter
$\delta\theta$	Amount of excess coverage
$\Delta_{\mathbf{B}}$	Activation energy of the isotropic bulk hopping channel
$\Delta_{\mathbf{SO}}$	Spin-orbit gap
$\epsilon(\vec{k})$	Tight-binding energy
$\hat{c}_{\vec{R},\sigma}$	Annihilation operator for an electron in a Wannier orbital
$\hat{c}_{\vec{R},\sigma}^\dagger$	Creation operator for an electron in a Wannier orbital
\hat{D}	Operator for the number of double occupancies on lattice sites
\hat{H}	Hamilton operator
\hat{J}	Total angular momentum
\hat{L}	Angular momentum
\hat{S}	Spin
λ	Atomic SOC
μ	Chemical potential
$\mu_{\mathbf{n}, \mathbf{p}}$	Mobility of electrons (n) or holes (p)
ϕ	Work function
$\phi_{\vec{k},\sigma}(\vec{R})$	Wannier orbital
ρ	Resistivity
σ	Conductivity
τ	Tunneling probability
θ	Coverage
\vec{E}	Electric field vector
\vec{R}	Lattice site
ξ	Coherence length
a	Lattice constant
$a_{\mathbf{B}}$	Bohr radius
d	Number of dimensions
E	Energy
$E_{\mathbf{B}}$	Binding energy

$E_{\mathbf{F}}$	Fermi energy
$E_{\mathbf{Kin}}$	Kinetic energy
I	Current
$k_{\mathbf{F}}$	Fermi wavenumber
L	Number of lattice sites
N	Number of electrons
n	Number of electrons per lattice site
$N_{\mathbf{A, D}}$	Acceptor or donor concentration
R	Resistance
T	Temperature
t	Tight-binding matrix element
$t_{\mathbf{SCL}}$	Thickness of the SCL
T_c	Phase transition temperature
U	Coulomb repulsion, “Hubbard U ”
V	Bias voltage
$v_{\mathbf{F}}$	Fermi velocity
W	Bandwidth
$W_{\mathbf{H}}$	Hysteresis width
Z	Atomic number
$Z_{\mathbf{N}}$	Number of nearest neighbors

Contents

I	Introduction and Physical Background	1
1	Introduction	3
2	Metal-insulator transitions	7
2.1	Mott transition	8
2.1.1	Hubbard model	8
2.1.2	Influence of spin-orbit coupling on Mott insulators	10
2.1.3	Influence of doping on Mott insulators	11
2.2	Peierls instability	14
2.2.1	Influences of surface steps on the Peierls transition	18
2.3	Spin-orbit density wave	20
3	Experimental methods	23
3.1	Scanning tunneling microscopy	23
3.1.1	Tunneling current	24
3.1.2	Scanning tunneling spectroscopy	24
3.1.3	4pp transport measurements	25
3.2	Low energy electron diffraction	30
3.3	Spin- and angle-resolved photoelectron spectroscopy	31
3.3.1	Rashba effect	32
3.3.2	Influence of light polarization	32
3.3.3	Spin-resolved measurements along a mirror axis	34
4	Experimental setup	37
4.1	Scanning tunneling microscope	37
4.1.1	Variable temperature STM	37
4.1.2	Low temperature STM	38
4.2	COPHEE endstation at SIS beamline	39
4.2.1	Calculation of the spin polarization	41
4.3	4pp STM/SEM	41
II	Self-Assembled Low-Dimensional Systems on Silicon Substrates	45
5	In/Si(111)-(4 × 1) reconstruction	47
5.1	Influence of spatial confinement on the Peierls transition	47
5.1.1	Characterization of the samples	48
5.1.2	Temperature-dependent transport investigations	50
5.2	Summary and conclusion	55
6	α-Sn phase on Si(111)	57
6.1	Phase diagram of Sn submonolayer structures on Si(111)	57

6.2	Structural properties of α -Sn	58
6.3	Low temperature phase of α -Sn	60
6.3.1	Spin-integrated constant energy and band maps	62
6.3.2	Spin-resolved band structure	64
6.3.3	Model for the spin-texture of the α -Sn phase	68
6.4	Summary and conclusion	69
7	Formation of Sn-induced nanowires on vicinal silicon surfaces	71
7.1	Growth of Sn on Si(557)	72
7.1.1	Intermediate and high coverage nanowires	73
7.1.2	Low coverage nanowires: a pseudo-gapped Mott state?	77
7.2	Summary and conclusion	78
8	Pb nanowires on a vicinal silicon substrate	81
8.1	Structural properties	82
8.1.1	Pb phases on (111) terraces	83
8.1.2	Nanowires on (223) facets	86
8.2	Electronic properties	90
8.2.1	Tunability via Pb excess coverage	93
8.3	High coverage nanowires	94
8.4	Summary and conclusion	95
III	Conclusion	97
9	Summary and outlook	99
IV	Appendix	105
A	Bibliography	107
B	Publication List	133
C	Curriculum Vitae	135

Part I

Introduction and Physical Background

Chapter 1

Introduction

The progress in information and computer technology proceeds at an exceptional constant pace during the last 50 years [1–3]. As the shrinking of transistor size nowadays tackles the nanoscale, new approaches beyond the classic silicon transistor are recently developed. Promising attempts are single-atom transistors [4–6], whose switching units are in the order of a few nanometers [6, 7].

The ongoing miniaturization is not solely restricted to electronic devices but affects the circuits as well, increasing the demand for nanoscale interconnects. It paves the way for extensive research on so-called nanowires, which diameters are in the nanometer range. Apart from being merely a substitution for conventional wires [8], they have attracted intense attention for building transparent electrodes. In optoelectronic devices, transparent conducting films are utilized for collecting charges from adjacent functional layers, like in the case of solar cells, or supplying charge carriers, e.g., in light emitting diode displays or touchscreens. Percolation networks of metallic nanowires arranged in a random mesh structure are promising candidates as a replacement for indium tin oxide films [9, 10], that is so far the most efficient and widely used but gets more expensive owing to the rarity of indium [11, 12]. Beside their electrical conductivity and optical transparency, a major advantage of, e.g., silver or copper nanowires is the high flexibility [9, 10, 13], which satisfies the current need for bendable electronics, such as flexible smartphone displays [14], or transparent heaters suitable as window defrosters and medical equipment [15].

From a fundamental research point of view, the confinement of systems to low dimensions offers the opportunity to investigate a wealth of exotic phenomena. These systems do not necessarily preserve the characteristics of the bulk material but come along with a variety of new physical properties, such as electronic interactions and correlations effects due to the finite size. For instance, two-dimensional (2D) electron gases realized by adsorption of metallic films on semiconductor surfaces are well-known to show quantum-size effects [16], which may influence their growth mode [17]. If spin-orbit coupling (SOC) is effective, the electronic effects are intimately related to magnetic phases [18]. Besides, the frustration of spin-1/2 systems on 2D triangular lattices favors complex spin-textures [19, 20], like the Mott-insulating low-temperature ground state with a row-wise antiferromagnetically ordering for the submonolayer α -Sn phase on Si(111) [21]. It is one aim of this work to provide a detailed description of its spin-split surface state dispersion.

However, the realization of truly one-dimensional (1D) atomic chains remains very demanding, requiring, e.g., either laser cooling [22, 23] or the gradual withdrawal of a scanning tunneling microscope tip dipped in a gold cluster [24]. The wires produced in this way are quite unstable and consist of just a few atoms. Both atomic wires and 2D films can be stabilized by embedding in a three-dimensional environment, i.e., they are grown on substrate surfaces. In the scope of this thesis, preparation of such systems is done via self-assembly on either flat or vicinal silicon wafers, resulting, e.g., in nanowires that are one atom high and several atoms wide. It leads to an inevitable coupling between the wires and the underlying substrate, as well as interactions between adjacent nanowires. This cannot be neglected in most cases and influences their properties, e.g., by adding another transport channel present in the sub-surface layer, which can have a significant impact on acquired transport data [25–27]. Besides, the interchain coupling can be altered by the presence of substrate steps, providing the possibility of growing defined amounts of interacting wires on top of substrates with a slight miscut angle. Thus, this kind of nanowires is often termed as “quasi-1D”.

During the last decades, much effort was put in research on metallic nanowires arranged on semiconducting substrates. The benchmark system in this context is the (4×1) -In/Si(111) reconstruction, which is one of the most comprehensively studied atomic chain systems. Although the substrate surface itself has a 2D symmetry, the In nanowires arrange in a 1D fashion on top due to preferential growth directions on the underlying silicon crystal. This typically results in the formation of multiple rotational domains. Upon cooling, it reversely shows a Peierls-like instability going along with a charge-density wave (CDW) on account of strong electron-phonon coupling accompanied by charge redistribution and periodic lattice distortions [28, 29], leading to an insulating ground state with a periodicity doubling both along and across the nanowires [30–32]. However, there are still open questions, e.g., regarding possible ways to tune the phase transition temperature T_c . So far, investigations mainly focused on the impact of additional atoms adsorbed on the indium chains, leading to a shift of T_c to either higher or lower temperatures, depending on the atom species [33–39], while the influence of step edges got significantly less attention [26].

Another approach for controlling size-induced effects is the use of vicinal surfaces as a template for nanowire growth. Substrates like Si(557) already display an inherent anisotropy due to its regular arrangement of atomic steps. In this case, a parallel array of nanowires are formed on top of small terraces between the steps. This opens up the possibility for a gradual tuning of the interaction strength between the nanowires by changing the terrace width, i.e., by employing differently inclined surfaces [40]. Some types of nanowires even induce a surface refacetting in order to relax the system into an energetically more favorable state. In particular, for 1.3 monolayers (ML) Pb on Si(557), the arising local (223) orientation introduces a new reciprocal lattice vector that exactly meets the spin-polarized nesting condition in the direction perpendicular to the nanowires. It gives rise to an insulating ground state caused by a delicate interplay of SOC and electronic interactions, which forms a so-called spin-orbit density wave (SODW) [41] while preserving the metallic conductance along the wires [42–44]. Therefore, this system can be reversely switched between 1D and 2D conductance by changing the temperature. Interestingly, Pb atoms added as surplus on the surface primarily tend to decorate the step edges [45], maintaining the spin-ordering up to an excess coverage of 0.2 ML Pb [41]. However, an important information for the understanding of the delicate interplay between the surface periodicity and the electronic structure is still missing up to

now, since the actual atomic structure of these nanowires is still under debate, suggesting either a densely packed ($\sqrt{3} \times \sqrt{3}$) reconstruction [43] or a domain structure similar to the devil's staircase phases observed for Pb/Si(111) [45].

Concerning peculiar electronic correlation effects, a promising candidate for nanowire growth is the Sn/Si(557) system. The element Sn is isoelectronic to Pb, but correlation effects are much stronger due to the smaller orbital size, while the spin-orbit coupling is weaker on account of the lower atomic number Z . As previously mentioned, the 2D α -Sn/Si(111) phase exhibits a Mott metal-insulator transition [21], where a metallic quasi-particle state can be introduced in the Mott insulating gap via doping [46]. Hence, the use of a vicinal substrate, as done in the scope of this thesis, offers the unique opportunity for investigating a spatially confined Mott state.

Structure of this thesis

After this introduction, Part I continues with a detailed description of various types of metal-insulator transitions feasible in low dimensional systems (chapter 2). It includes theoretical descriptions of the Mott transition existing in the α -Sn/Si(111) phase, the Peierls instability present in the In/Si(111) reconstruction, and the SODW, which is the insulating ground state of the Pb/Si(557) nanowires. Afterward, the experimental methods (chapter 3) used in the course of this thesis are introduced, as well as the setup of the utilized vacuum chambers (chapter 4). Primarily, scanning tunneling microscopy (STM) was used in order to obtain atomically resolved images of the surface reconstructions. Apart from this, a four-point-probe (4pp) STM was employed for transport experiments, and band structure investigations were done by spin- and angle-resolved photoemission (SARPES), while low energy electron diffraction (LEED) mainly ensured a consistently high sample quality.

Part II discusses in detail finite-size and SOC effects in low-dimensional systems. First, the influence of confinement on the phase transition temperature of In/Si(111) due to substrate steps is examined in chapter 5, causing a lack of interchain interactions in the vicinity of the step edge. Next, the spin structure of the electronically correlated surface state of the α -Sn reconstruction on Si(111) is probed using SARPES and a model for an in-plane spin-ordering is proposed (chapter 6). This is followed by a detailed study on the formation of Sn-induced nanowires on Si(557) (chapter 7). Three distinct nanowire phases at different Sn coverages are identified, one of them being the confined Mott state resulting in the quenching of the insulating gap. The last experimental chapter 8 treats the structural and electronic properties of the low-temperature SODW phase of the Pb/Si(557) system.

Finally, in Part III, all experimental findings are summarized (chapter 9), and an outlook about further research possibilities is given in chapter 9.

Metal-insulator transitions

In the course of this thesis, several material systems were investigated. Regardless of whether they showed one- or two-dimensional behavior, all of them exhibited a common feature: a phase transition from a metallic to an insulating state depending on temperature. The following chapter gives insight into the different types of metal-insulator transitions (MIT). It is based on the book *The Mott Metal-Insulator Transition* by F. Gebhard [47].

In general, in the approximation of zero temperature and small external fields, two basic categories of insulating states can be identified:

1. insulators due to electron-ion interaction, and
2. insulators due to electron-electron interaction.

Considering only static ion configurations, the first category includes insulators that can be described by a single-electron theory. Most prominent examples are

- Bloch-Wilson or band insulators [48–50] due to the electrons' interaction with the periodic potential of the ions;
- Peierls insulators [30] due to the electrons' interaction with phonons, and
- Anderson insulators [51] due to the presence of disorder, e.g., the electrons' interaction with impurities and other lattice imperfections.

On the other hand, for insulators of the second category, a many-electron problem has to be solved. It includes

- Mott insulators [52] due to the electrons' mutual interaction.

In the scope of this work, insulators and the associated metal-insulator transition of both categories were studied. The isostructural Mott transition occurring in α -Sn/Si(111) is introduced in chapter 2.1, as well as how this transition is influenced by means of either SOC or doping. The In/Si(111)-(4 × 1) phase undergoes a Peierls-like transition to an insulating (8 × 2) reconstruction. The mechanism behind it is described in more detail in chapter 2.2. Besides, a more recently established theory is presented in chapter 2.3, namely the spin-orbit density wave (SODW). It explains the insulating ground state of Pb/Si(557), considering both electronic correlations and SOC.

2.1 Mott transition

Already back in 1937, it was pointed out that the theoretical description of metals and insulators with a model of non-interacting electrons does not always reproduce the experimentally observed characteristics. For instance, materials like nickel oxide with partially filled $3d$ bands show semiconducting or insulating behavior, although theory predicts them to be metallic [49, 53].

Nevill Mott solved this apparent contradiction by arguing that the electrons in transition metal oxides may not be considered free as done in the nearly-free electron model. Instead, they experience strong local Coulomb repulsions [52, 54–56]. A few years later, this postulation led to the *Hubbard model*, a lattice fermion model which includes the simplest many-body Hamiltonian that can describe the interplay between kinetic energy and Coulomb repulsion. M. C. Gutzwiller [57] independently proposed it in order to describe the metal-insulator transition, J. Kanamori concerning itinerant ferromagnetism, and the namesake J. Hubbard [58] regarding transition metals. It will be introduced in more detail in the following section, as well as the influences of both SOC and doping on Mott-insulating systems (chapters 2.1.2 and 2.1.3).

2.1.1 Hubbard model

The Hubbard model (or *one-band Hubbard model*) is based on two basic assumptions [59], namely

1. interactions are local, i.e., only between electrons on the same atom, and
2. it exists only one band at half filling.

A common example is a d -dimensional cubic lattice of hydrogen atoms with Bohr radius a_B and lattice constant a . The number of lattice sites L is equal to the amount of electrons N as each hydrogen atom provides one electron, resulting in a half filled band. In order to describe the potential energy of this system, the so-called “Hubbard U ” is introduced. It is defined as the intra-atomic energy or on-site Coulomb repulsion, thus ionization energy minus electron affinity,

$$U = E(\text{H} \rightarrow \text{H}^+) - |E(\text{H} \rightarrow \text{H}^-)| = E(\text{H}^-) + E(\text{H}^+) - 2E(\text{H}). \quad (2.1.1)$$

Assuming only hopping between nearest neighbors is allowed, the *tight-binding* approximation for independent electrons leads to a cosine dispersion relation of the tight-binding energy

$$\epsilon(\vec{k}) = -2t \sum_{j=1}^d \cos(k_j a). \quad (2.1.2)$$

Here the bandwidth is given by $W = 2Z_N t$, with the number of nearest neighbors $Z_N = 2d$ and the tight-binding matrix element $t > 0$, that is related to the electron hopping probability from its lattice site to the nearest neighbor site and depends on a/a_B . Hence as a increases, the orbital overlap as well as the bandwidth decreases. However, in this case it remains a metallic state even for very large distances in between the atoms. The inconsistency can be solved taking into account the Hubbard U . A critical value of a can now be found, where

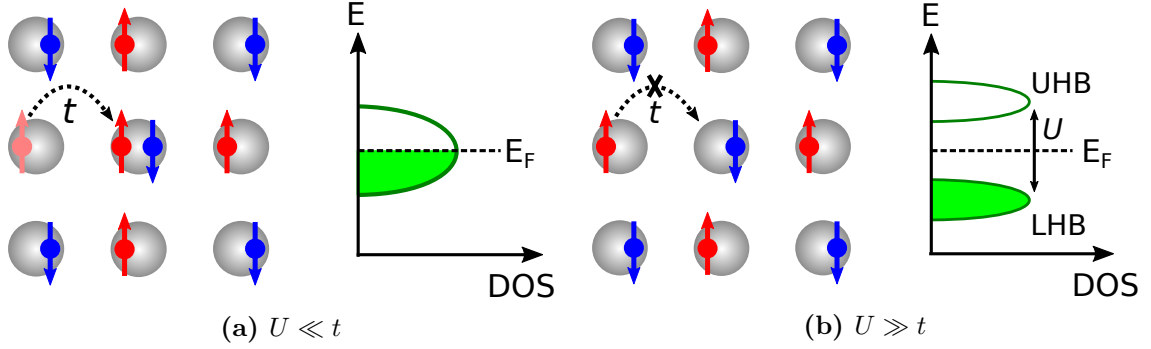


Figure 2.1: Schematic illustration of the structure and the density of states (DOS) above and below a Mott MIT. (a) Weakly correlated metallic state $U \ll t$: electron conductivity is possible via hopping. (b) Strongly correlated insulating state $U \gg t$: electrons are highly localized at single-occupied lattice sites.

the energy gained by hopping is smaller than the energy needed to overcome the Coulomb repulsion. This results in the Hamiltonian operator of the Hubbard model,

$$\hat{H} = \hat{H}_{\text{Band}} + \hat{H}_U = -t \sum_{\vec{R}_1 \neq \vec{R}_2} \sum_{\sigma} \hat{c}_{\vec{R}_1, \sigma}^{\dagger} \hat{c}_{\vec{R}_2, \sigma} + U \sum_{\vec{R}} \hat{n}_{\vec{R}, \uparrow} \hat{n}_{\vec{R}, \downarrow} \quad (2.1.3)$$

describing the interplay between the kinetic energy band term \hat{H}_{Band} and the Coulomb repulsion term \hat{H}_U in second quantization [57, 60]. \hat{H}_{Band} defines the electron hopping between neighboring lattice sites \vec{R}_1 and \vec{R}_2 . The operators $\hat{c}_{\vec{R}, \sigma}^{\dagger}$ and $\hat{c}_{\vec{R}, \sigma}$ create or annihilate an electron in the Wannier orbital $\phi_{\vec{R}, \sigma}(\vec{R})$, that is a well-localized state in order to fulfill the assumption of local interactions. \hat{H}_U comprises the operator for the number of double occupancies

$$\hat{D} = \sum_{\vec{R}} \hat{n}_{\vec{R}, \uparrow} \hat{n}_{\vec{R}, \downarrow} \quad \text{with} \quad \hat{n}_{\vec{R}, \sigma} = \hat{c}_{\vec{R}, \sigma}^{\dagger} \hat{c}_{\vec{R}, \sigma}, \quad \sigma = \uparrow, \downarrow. \quad (2.1.4)$$

According to Eq. 2.1.3 two limiting cases are found, namely weak and strong correlations:

$U \ll t$: In the weakly correlated case, the Coulomb repulsion experienced by the electrons is much lower than the hopping probability. Hence the electrons are free to move to other lattice sites, and double occupancies are possible as depicted in Fig. 2.1 (a). This delocalization of the electrons leads to a half-filled state at the Fermi energy E_F making the system metallic.

$U \gg t$: In the strongly correlated case hopping is suppressed by strong on-site Coulomb repulsion. Thus electrons are localized on single-occupied lattice sites as shown in Fig. 2.1 (b). This results in an insulating system characterized by the formation of the occupied lower Hubbard band (LHB) and the unoccupied upper Hubbard band (UHB). These bands are filled for $N = L$ electrons each, in contrast to conventional insulating bands with $N = 2L$. The LHB and UHB are separated by the energy U needed to remove one electron from a single-occupied site and hop to an adjacent single-occupied site.

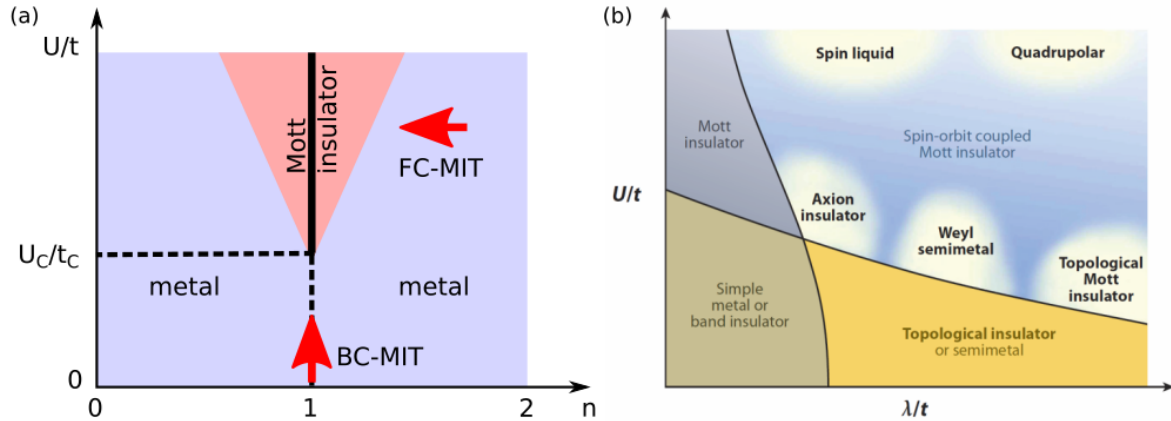


Figure 2.2: (a) Phase diagram of a Mott MIT showing the ratio U/t in dependence of the electron density n ; at $n = 1$ the band is half filled. For $n \neq 1$ and/or a correlation strength less than U_c/t_c the system is metallic. The triangular-shaped pink area highlights the fluctuation regime at values close to the Mott-insulating phase. Two ways for the MIT are indicated by red arrows: the BC-MIT and the FC-MIT. Adapted from [61, 62]. (b) Schematic phase diagram displaying U/t in dependence of the spin-orbit coupling strength λ/t . It can be divided into four quadrants with weak or strong correlation regimes and weak or strong SOC regions. Image is taken from Ref. [18].

For intermediate values of U and t , the system undergoes a metal-insulator transition. This happens at a critical ratio U_c/t_c , at which the Hubbard U is small enough and the bandwidth W ($\propto t$) large enough for the Hubbard bands to "overlap". The phase diagram of a Mott MIT is plotted in Fig. 2.2 showing the U/t ratio in dependence of the number of electrons per lattice site $n = N/L$. As mentioned before, the insulating phase is present only at half filling ($n = 1$) and above the critical value U_c/t_c . Doping the system by adding either electrons or holes changes the electron density and leads to a metallic state. For sufficient high correlations, an unstable fluctuation regime exists, which exhibits a strong coupling of the insulating phase, while it is generally assumed to be metallic [61, 62].

In total there are two different way to drive a system into a Mott insulating state as highlighted with red arrows in Fig. 2.2 (a). In case of a half-filled band ($n = 1$), a change in U/t that results in a value above a finite U_c/t_c is called a *bandwidth controlled-* (BC-)MIT. A *filling controlled-* (FC-)MIT is possible for systems with a sufficient high U/t ratio and a non-integer filling n close to $n = 1$. Thus, changing the electron density by carrier doping yields a Mott insulating phase as well (cf. chapter 2.1.3) [61].

2.1.2 Influence of spin-orbit coupling on Mott insulators

Up to now, the systems considered here were only allowed to experience electronic correlations in between the electrons. However, especially in heavy elements, an interaction between orbital angular momentum and electrons is observable. This effect scales with Z^4 with Z being the atomic number, and it is known as spin-orbit coupling (SOC). For a detailed description and the derivation of the following equations refer to, e.g., [63]. In this section, the combination of these two central topics in quantum material research will be discussed

based on a review paper by W. Witczak-Krempa et al. [18].

Compared to the previously considered Hamilton operator in Eq. 2.1.3, the inclusion of SOC adds a third component, namely

$$\hat{H}_{\text{SOC}} = \lambda \sum_{\vec{R}} \vec{L}_{\vec{R}} \vec{S}_{\vec{R}}. \quad (2.1.5)$$

In this equation λ is the atomic SOC, which entangles spin ($\vec{S}_{\vec{R}}$) and angular momentum ($\vec{L}_{\vec{R}}$). It depends on the quantum numbers n and l of the electrons' orbital. Hence the entire Hamilton operator yields

$$\hat{H} = \hat{H}_{\text{Band}} + \hat{H}_U + \hat{H}_{\text{SOC}} = -t \sum_{\vec{R}_1 \neq \vec{R}_2} \sum_{\sigma} \hat{c}_{\vec{R}_1, \sigma}^{\dagger} \hat{c}_{\vec{R}_2, \sigma} + U \sum_{\vec{R}} \hat{n}_{\vec{R}, \uparrow} \hat{n}_{\vec{R}, \downarrow} + \lambda \sum_{\vec{R}} \vec{L}_{\vec{R}} \vec{S}_{\vec{R}}. \quad (2.1.6)$$

The interplay of electronic correlation strength U/t and SOC strength λ/t gives rise to a variety of different phases. A schematic phase diagram is displayed in Fig. 2.2 (b). It should be emphasized that the lines shown are not necessarily meant as sharp boundaries and it is not claimed to be complete. Roughly it can be divided into four quadrants. If both ratios are small, the system is a simple metal or a band insulator, depending on the band filling. As already discussed in the previous section, increasing U/t leads to a Mott insulating state. Regarding strong SOC strength and weak electronic correlations, the system turns into a topological insulator or a semimetal. The largest regime drawn in the phase diagram is characterized by high values of both U/t and λ/t . It is termed as *spin-orbit coupled Mott insulator* and includes a wide range of different phases, e.g. spin liquids and topological Mott insulators.

The strength of SOC can be quantified by calculating the resulting spin-orbit gap Δ_{SO} using the Landé interval rule [64]. It is defined as the splitting between neighboring atomic fine structure levels with a total angular momentum J and $J-1$, respectively, and $\hat{J} = \hat{L} + \hat{S}$:

$$\Delta_{\text{SO}} = \Delta E_J - \Delta E_{J-1} \propto \frac{\lambda}{2} (J(J+1) - (J-1)J) = \lambda J \quad (2.1.7)$$

Here, ΔE_J and ΔE_{J-1} are the energy shifts of the respective energy level due to SOC [65].

So far the α -Sn/Si(111) phase was considered as a prototypical 2D Mott system with a phase transition temperature of ~ 70 K [66]. Density functional theory (DFT) calculations yield a Hubbard $U = 0.60$ eV and the electronic hopping parameter $t = 52.7$ meV, confirming the strong electronic correlations of this system [21]. Influences of SOC were not taken into account because the spin-orbit gap scales with Z^4 . Thus, $\Delta_{\text{SO}} = 0.8$ eV for Sn atoms is relatively small compared to, e.g., Pb atoms, which are well-known to show a pronounced effect of SOC ($\Delta_{\text{SO}} = 2.0$ eV) [67, 68]. However, as described in chapter 6, it turned out that indeed it is not negligible but gives rise to a small *Rashba*-type spin splitting of the surface state (cf. chapter 3.3.1). Therefore the α -Sn phase should rather be termed a weakly spin-orbit coupled Mott insulator.

2.1.3 Influence of doping on Mott insulators

As already pointed out in chapter 2.1, for a Mott transition, a half-filled band is essential. Any deviation in the electron density may lead to a collapse of the insulating state resulting in

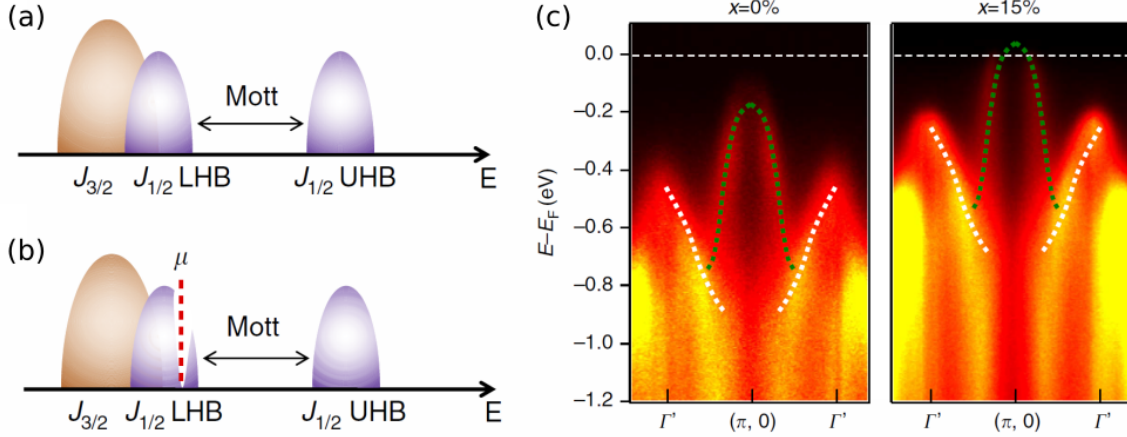


Figure 2.3: Schematic picture showing (a) the Mott insulating gap of Sr_2IrO_4 and (b) the evolution of the chemical potential with Rh doping. (c) ARPES band maps of Sr_2IrO_4 (left) and $\text{Sr}_2\text{Ir}_{0.85}\text{Rh}_{0.15}\text{O}_4$ (right) showing a chemical potential shift of $\Delta\mu \sim 200$ meV due to doping. All images are taken from [69].

a metallic ground state. This topic has been intensely studied for more than 20 years in order to take advantage of this behavior. Prominent examples are cuprate oxides which can be hole doped to induce a Mott-type MIT and turn into high-temperature superconductors upon even further doping. An extensive review on these materials and their investigation with angle-resolved photoemission spectroscopy (ARPES) experiments can be found elsewhere, e.g., [70]. Other oxide compounds such as titanium oxides show similar phase transitions from Mott insulators to a Fermi-liquid behavior, eventually resulting in charge-transfer insulators [71]. In all of these cases, the doping was carried out via changing the stoichiometry of the oxide compounds.

A different approach was made by Cao et al. [69]. They doped the Mott insulator Sr_2IrO_4 by substitution of iridium atoms with rhodium atoms forming a hole-doped $\text{Sr}_2\text{Ir}_{(1-x)}\text{Rh}_x\text{O}_4$ compound series. The hole-doping is not a result of a difference in electrons as Ir and Rh are isovalent since they are in the same group in the periodic system. It is rather caused by the reduced SOC of Rh that is due to the lower atomic number Z and leads according to Eq. 2.1.7 to a reduced fine structure splitting [72]. A concentration of 4% Rh is sufficient for a drop in resistivity of 10^4 , although the long-range magnetic order survives until 15% Rh. The mechanism behind the phase transition to a metallic state is a shift in chemical potential μ . For the parent compound, μ is in the Mott insulating gap opened up between LHB and UHB. Upon doping with Rh, μ shifts to lower energies, eventually reaching the LHB. These situations are schematically visualized in Figs. 2.3(a) and (b). It was verified by ARPES measurements that confirm a shift of $\Delta\mu \sim 200$ meV resulting in a metallic state for a doping concentration of 15% Rh (see Fig. 2.3(c)).

Up to now, only hole-doping was considered. However, doping with electrons is also possible as seen in the case of the weakly spin-orbit coupled Mott insulating parent compound $\text{Sr}_3\text{Ir}_2\text{O}_7$. It is done by substitution Sr^{2+} ions with La^{3+} ions leading to a $(\text{Sr}_{(1-x)}\text{La}_x)_3\text{Ir}_2\text{O}_7$ compound series. A robust metallic state is observed at a doping concentration of 4% La [74] or 5% La [75]. At intermediate concentrations $0 < x < 4\%$ La the Mott insulating state

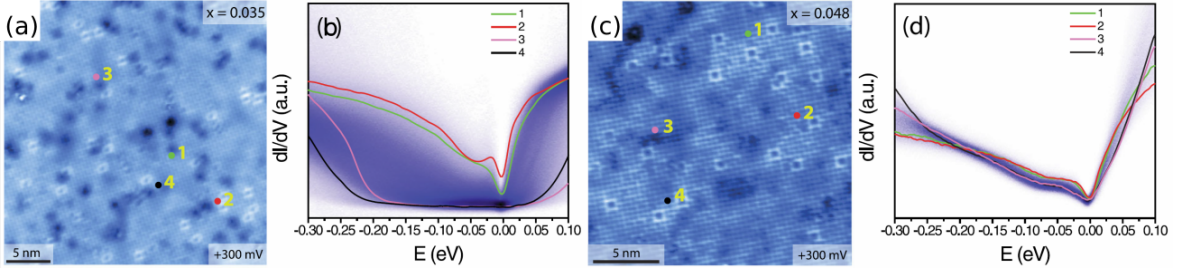


Figure 2.4: STM topography of $(\text{Sr}_{(1-x)}\text{La}_x)_3\text{Ir}_2\text{O}_7$ at $U = 300$ mV and dI/dV spectra obtained on a grid in each topography for (a), (b) partly insulating $x = 3.5\%$ and (c), (d) metallic $x = 4.8\%$ samples. Representative numbered points are labeled in each map and the corresponding dI/dV spectra are emphasized as solid lines. For the $x = 3.5\%$ sample both fully gapped and gapless spectra are observed, while for $x = 4.8\%$ the surface exhibits homogeneous gapless states. Images are taken from [73].

is fragmented into nanoscale regions showing either metallic or insulating character. This was shown in scanning tunneling spectroscopy (STS) measurements obtained on a grid in STM topographies of $(\text{Sr}_{(1-x)}\text{La}_x)_3\text{Ir}_2\text{O}_7$ samples with $x = 3.5$ and $x = 4.8$, as displayed in Fig. 2.4. For the lower dopant concentration, both fully gapped and gapless spectra are observed, which confirm a phase-separated ground state. At concentrations above $x \approx 4\%$, a homogeneous metallic ground state is present, and only gapless spectra are measured [73].

Recently, the α -Sn/Si(111) system studied in this thesis got attention regarding the effect of doping. Ming et al. [46] successfully hole-doped the half-filled dangling bond orbitals of the Sn atoms. To accomplish their goal, they introduced excess charges by using differently n - and p -type doped Si(111) substrates resulting in identical STM images of the α -Sn phase no matter which substrate was used. However, even for highly n -doped samples electron doping was suppressed by a subsurface region where dopant conversion took place during high-temperature annealing in an ultra-high vacuum (UHV) environment [27, 76–78]. Instead, the highly n -doped samples show a STS spectrum as it would be expected for an undoped Mott insulator featuring LHB and UHB with a 0.2 V Mott gap in between. Thus the excess electrons of the substrate are partially compensated by localized defect states (see supplemental material of [46]). At low n -doping concentrations a quasi-particle peak (QPP) evolves centered about 0.1 eV above E_F . Its intensity increases with increasing hole-doping, as displayed in Figs. 2.5(a). It reaches a maximum for p -doped substrates with a room-temperature (RT) resistivity of 0.001 Ωcm that corresponds to a hole-doping level of about 10%, where segregated boron atoms form a $(\sqrt{3} \times \sqrt{3})$ superstructure below the topmost silicon layer (labeled as “ $B\sqrt{3}$ ” in Fig. 2.5(a)). For this high dopant concentration, the spectral features (UHB, LHB, and QPP) are spatially uniform, and hence they do not show any competing nanophases like the intermediately-doped iridate oxides [73]. The dispersion relation along the $\bar{\Gamma}\text{KM}$ and $\bar{\Gamma}\text{M}$ directions for the QPP on the $B\sqrt{3}$ determined both experimentally and theoretically is depicted in Figs. 2.5(b) and (c), respectively. Furthermore, a distinctive hallmark of a Mott insulator is observed in the STS spectra, namely the spectral weight transfer from LHB and UHB to the QPP upon hole-doping (see Fig. 2.5(d)) [46].

In chapter 7 another approach was chosen for doping the α -Sn/Si(111). The 2D Mott-insulating phase was confined to small stripes by the use of a vicinal substrate as a template.

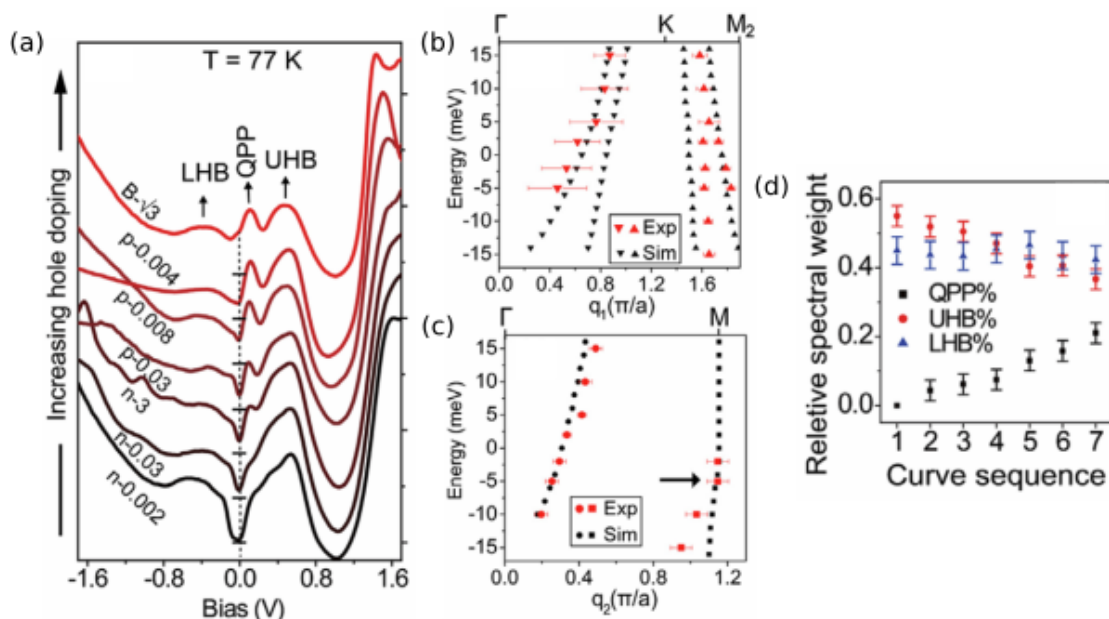


Figure 2.5: (a) dI/dV spectra measured at 77 K for the α -Sn phase grown on differently doped Si(111) substrates. The labels refer to their doping type and resistivity, e.g. “n-0.002” is n -doped with a RT resistivity of 0.002 Ωcm . “B- $\sqrt{3}$ ” is the substrate with the highest p -doping, where segregated boron atoms form a $(\sqrt{3} \times \sqrt{3})$ superstructure below the topmost Si layer. The spectra are offset vertically for clarity; horizontal tick marks on the dashed vertical line at zero bias indicate the origin for each curve. Dispersion relation of the QPP extracted from Fourier transformed bias-dependent differential conductance maps along the (b) $\bar{\Gamma}\text{KM}$ and (c) $\bar{\Gamma}\text{M}$ directions. Red dots refer to experimental measurements, black dots represent theoretical results. (d) Relative intensities of the UHB, LHB, and QPP highlighting the spectral weight transfer. Numbering refers to the curves in (a), counted from bottom to top. All pictures are taken from [46].

By this means, the structure is doped by Sn excess coverage adsorbed in the step edges which provide binding sites with electronic properties different from the flat surface, leading to partially ionized atoms. Similar doping characteristics have been reported in the case of Ag nanowires on Si(557), resulting in an effective electron-doping of the surface [79].

2.2 Peierls instability

The Peierls metal-insulator transition leads to an insulating phase with a periodic lattice distortion below a certain transition temperature. The mechanism behind the transition will be explained in the following, based on the book of Rudolf Peierls [30].

The Peierls MIT can be visualized most easily by a 1D atomic chain. The atoms are equidistant with a lattice constant a , which means the boundaries of the surface Brillouin zone (SBZ) are at $k = \pm\pi/a$. Assuming one electron per lattice site and a sufficient overlap between neighboring electron orbitals results in a half-filled cosine conduction band, as shown in Fig. 2.6(a). Coulomb interaction is neglected in this case. The Fermi wavenumber is $k_F = \pi/2a$. If electron-phonon interaction is present, decreasing the temperature leads to a

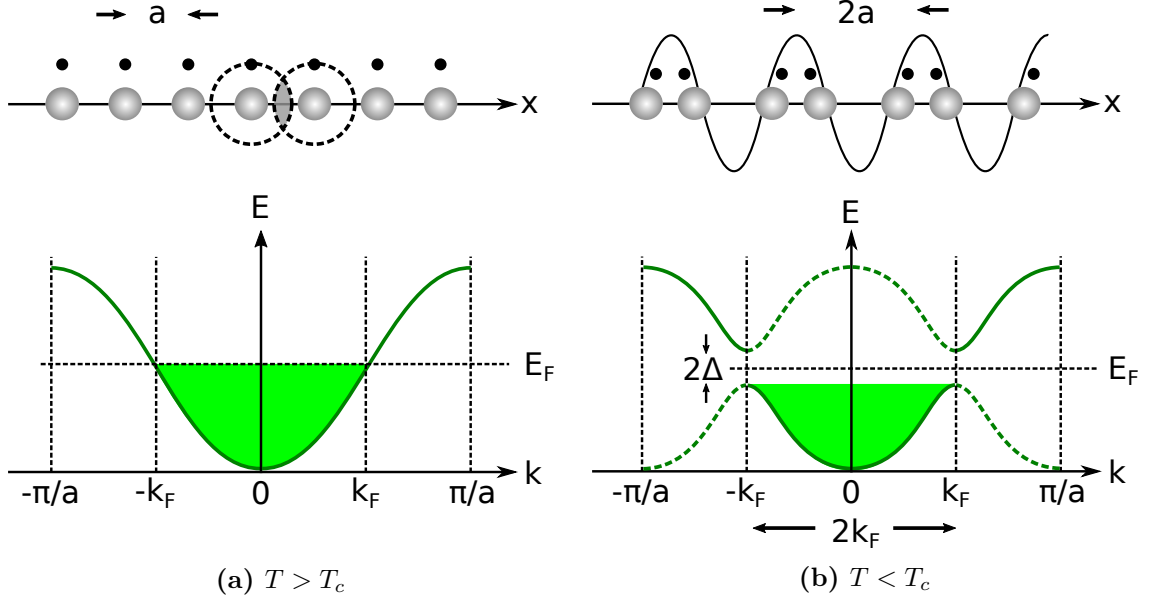


Figure 2.6: Model of a one-dimensional atomic chain (a) above and (b) below the transition temperature T_c , and the corresponding bandstructures. Grey circles denote atoms, black circles are electrons. Below T_c a lattice distortion occurs leading to a charge-density modulation. The SBZ is resized and a band gap 2Δ opens up. The back-folded bands are depicted by dashed green lines. Adapted from [80].

periodic lattice distortion of the chain. Thus a charge density modulation arises. It forms a new unit cell with a size of $2a$ containing two electrons. Concerning the bandstructure, this means a resizing of the SBZ to $k = \pm\pi/2a$. Hence the boundaries of the SBZ coincide with k_F and a band gap 2Δ opens up at E_F (see Fig. 2.6 (b)). Consequently, the system turns into an insulator [80].

This kind of metal-insulator transition takes place only if the gain in energy due to the band gap outweighs the energy loss by the distortion of the chain. A detailed analysis of the energetic contributions can be found elsewhere, e.g., [81]. Furthermore, it is not restricted to half-filled bands. The transition may as well occur for $k_F = \pi n/2a$ with the number of electrons per unit cell $n < 2$. The resulting insulating chain develops a periodic lattice distortion with a wavelength of $2a/n$ [30].

One of the systems showing a temperature dependent Peierls transition from a conducting RT to an insulating low-temperature (LT) state is the In/Si(111)-(4 × 1) reconstruction. This reversible change was first reported by Yeom et al. [31], whose STM images display a structural change of the indium reconstruction during cooling. Compared to RT, the LT phase imaged at ~ 65 K features a pronounced $\times 2$ periodicity in the direction along the chains. Furthermore, the interaction of neighboring chains leads to an additional periodicity doubling in the direction perpendicular to the chains, that was formerly misinterpreted as a random phase mismatching. Hence, the (4 × 2) phase, as Yeom et al. termed it, actually is a (8 × 2) reconstruction. Nevertheless, this was a pioneering work that paved the way for a comprehensive and still ongoing characterization of the phase transition. For instance, the possibility of photo-inducing the MIT was recently shown [82, 83].

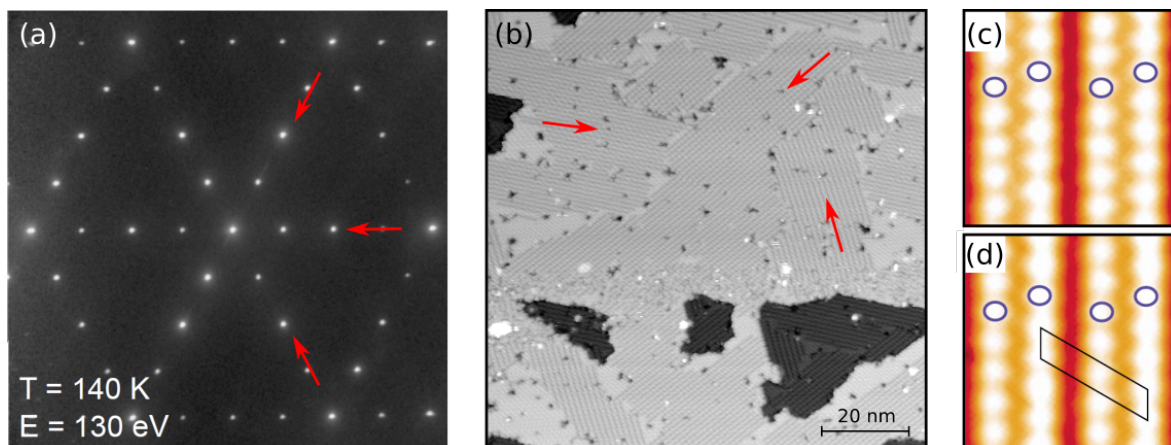


Figure 2.7: (a) SPALEED pattern taken from Ref. [84] and (b) STM image of the RT (4×1) phase. Three rotational domains are indicated with red arrows. (c) Filled and (d) empty states high resolution STM images taken at $T = 135$ K, $V = \mp 0.15$ V and $I = 20$ pA, both taken from Ref. [85]. Open circles mark charge-density maxima of the empty state image.

In Fig. 2.7(a) the spot profile analysis LEED (SPALEED) pattern [84] of the (4×1) reconstruction is displayed. Red arrows indicate three domains rotated against each other by 120° , due to the C_{3v} symmetry of the underlying Si(111) substrate. These domains are separated by domain boundaries that are visible in a large scale STM image, as seen in Fig. 2.7(b). In order to get a closer insight in the atomic structure, high resolution STM images were taken at bias voltages close to E_F , measuring either filled or empty states (Figs. 2.7(c) and (d), respectively). They reveal that one chain of the (4×1) reconstruction consists of two indium rows parallel to each other. Charge density maxima (marked by circles) are located at the same position for both filled and empty states. It indicates gapless states and thus a metallic nature of the surface [85].

Cooling down the sample well below the critical temperature $T_c \approx 120$ K, the In surface reconstruction undergoes a phase transition to the LT phase. In the SPALEED image (see Fig. 2.8(a)) pronounced $\times 8$ diffraction spots appear in the direction perpendicular to the chains. It accompanied by $\times 2$ -streaks in the parallel direction, that do not appear as sharp spots due to the coexistence of two degenerate (8×2) structures [87, 88]. The high resolution STM images clearly show the periodicity doubling along the chains (cf. Figs. 2.8(b) and (c)). Besides, especially in the filled state's image, it becomes evident that across the chains, the unit cell is doubled in size as well compared to the RT phase. The oval-shaped charge density maxima of adjacent chains are tilted against each other due to interchain interactions. Comparing charge density maxima of filled and empty states, it is noteworthy that they are not at the same positions, like at RT. This already hints towards an insulating behavior of the surface.

The structural phase transition is accompanied by an electronic phase transition, which can be verified by STS and transport data. $I(V)$ curves taken at different temperatures above and below the MIT are displayed in Fig. 2.8(d). At RT the system clearly shows metallic behavior, whereas at LT, i.e., 40 K, it is an insulator. For a moderate temperature of ~ 110 K,

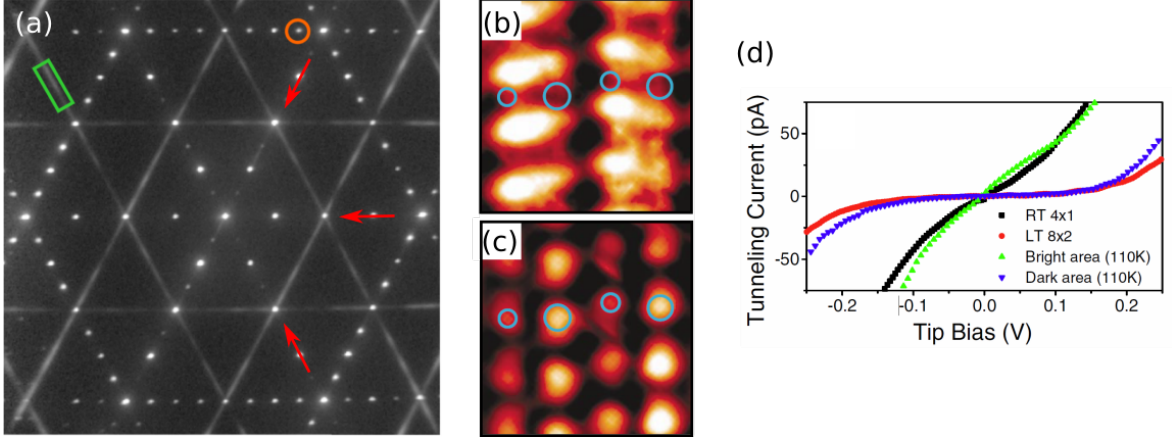


Figure 2.8: (a) SPALEED pattern of the LT (8×2) phase with $T = 80$ K and $E = 130$ eV. The $\times 8$ diffraction spot and the $\times 2$ streak are highlighted in orange and green, respectively. Three rotational domains are indicated with red arrows. Image is taken from Ref. [84]. (b) Filled and (c) empty states high resolution STM images measured at $T = 135$ K, $V = \mp 0.30$ V and $I = 30$ pA, both taken from Ref. [85]. Open circles mark charge-density maxima of the empty state image. (d) STS spectra taken at RT (black), 40 K (red) showing the metallic or insulating behavior of the (4×1) or (8×2), respectively. The green and blue $I(V)$ curve are measured at 110 K, where both phases were present on the surface; taken from Ref. [86].

both phases are simultaneously present on the surface. They are easily distinguishable due to a different contrast in STM and their STS spectra resemble either the ones taken at RT or LT, respectively [86]. Furthermore, the electrical conductivity observed in 4pp measurements exhibits a sharp decrease upon cooling below T_c [89]

According to the structural model presented in Fig. 2.9 [90], the (4×1) reconstruction of the RT phase consists of two zigzag-shaped indium rows, as well as a chain of silicon atoms, which separates these nanowires. This incorporation of substrate atoms into the indium reconstruction leads to the formation of bilayer-deep holes on the formerly flat surface, with a flat bottom that is covered with the (4×1) phase as well [91, 92]. It is visible in large scale STM images, e.g. in Fig. 2.7(b). During cooling below the phase transition temperature, the zigzag arrangement of the indium atoms gets slightly deformed. Instead, a hexagonal structure develops with a (8×2) unit cell. This rearranging leads to a Peierls-like periodicity doubling, and thus it is accompanied by the opening of a fundamental band gap [90]. Further studies reveal that this transition involves not only one surface band but in total three of them. ARPES data show a Peierls-like gap opening of one band that is half-filled above T_c . Additionally, two other quasi-1D metallic bands evolve into a single insulating band during the phase transition [93].

The phase transition, as described so far, is well-known to rather occur in a certain temperature range than on a specific value. For instance, in STM measurements, both phases can be observed at the same temperature on a nanometer scale [86, 94, 95]. Besides, T_c strongly depends on the sign of the temperature change, i.e., if the sample is heated or cooled across the MIT. A high-resolution LEED study reported a hysteresis of the (8×2) diffraction spot intensities during thermal heating and cooling cycles, which has a width of

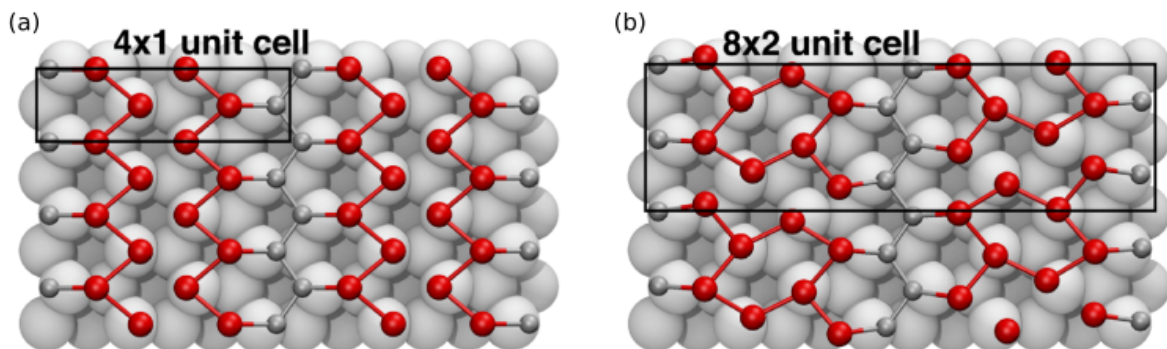


Figure 2.9: Schematic picture showing the atomic structure of the (a) (4×1) zigzag chains and (b) (8×2) hexagonal phase of In/Si(111). Red and gray balls indicate indium and silicon atoms, respectively. Images taken from Ref. [90].

$W_H \approx 10$ K, independent from the rate of temperature change [84]. This was confirmed by conductivity measurements done with a 4pp system in a linear arrangement using as well different temperature changing rates, i.e., ∓ 1 K/min and ∓ 2.5 K/min [88]. Upon cooling, the sheet conductivity exhibits a rapid increase below $T_1 \approx 119.1$ K, while during heating, the threshold phase transition temperature is significantly higher, namely $T_2 \approx 127.5$ K. This results in a thermal hysteresis with $W_H \approx 8$ K, as shown in Fig. 2.10 (a) and in its close-up of the region around $T \sim 120$ K in Fig. 2.10 (b). By comparison with previous data [96], the actual value of T_c , where both phases have equal free energies, was calculated to be 126.5 K. Moreover, the presence of surface steps may influence the apparent phase transition temperatures, which will be addressed in the next section in more detail.

2.2.1 Influences of surface steps on the Peierls transition

Surface steps play an important role for the In/Si(111)- (4×1) reconstruction. Already at RT, their influence is visible, since a preferred growth direction for the (4×1) domains can be induced even for samples with just a slight miscut from the flat Si(111) orientation. For a miscut in $[11\bar{2}]$ direction, the three rotational (4×1) domains remain approximately equally distributed on the surface despite the presence of step edges, as shown in the STM images in Figs. 2.11 (a). However, if the opposite miscut direction is chosen, i.e., $[\bar{1}\bar{1}2]$, only a single domain is observed, which runs parallel to the surface step [97], see Fig. 2.11 (b). This is attributed to the nearest distance between an In adatom on a chain running parallel to the step edge and the adjacent Si atom on the step edge. It was calculated to be 0.442 nm or 0.558 nm for the $[\bar{1}\bar{1}2]$ or $[11\bar{2}]$ miscut direction, respectively, with the single-domain growth favored for the closer proximity case. Structural models of both miscut types are provided in Fig. 2.11 (c) and (d). If the terrace size exceeds ~ 30 nm, the influence of the step edges is no longer noticeable, and the formation of all three rotational domains sets in [97]. This behavior is often exploited to grow large single-domain In/Si(111) samples, using miscut angles between 1° and 4° [25, 98, 99].

The question now arises, whether the substrate steps influence the phase transition temperature as well. Hatta et al. [88] already suggested the presence of step edges alters the thermal hysteresis of the sheet conductivity seen on indium chains grown on a flat Si(111) substrate.

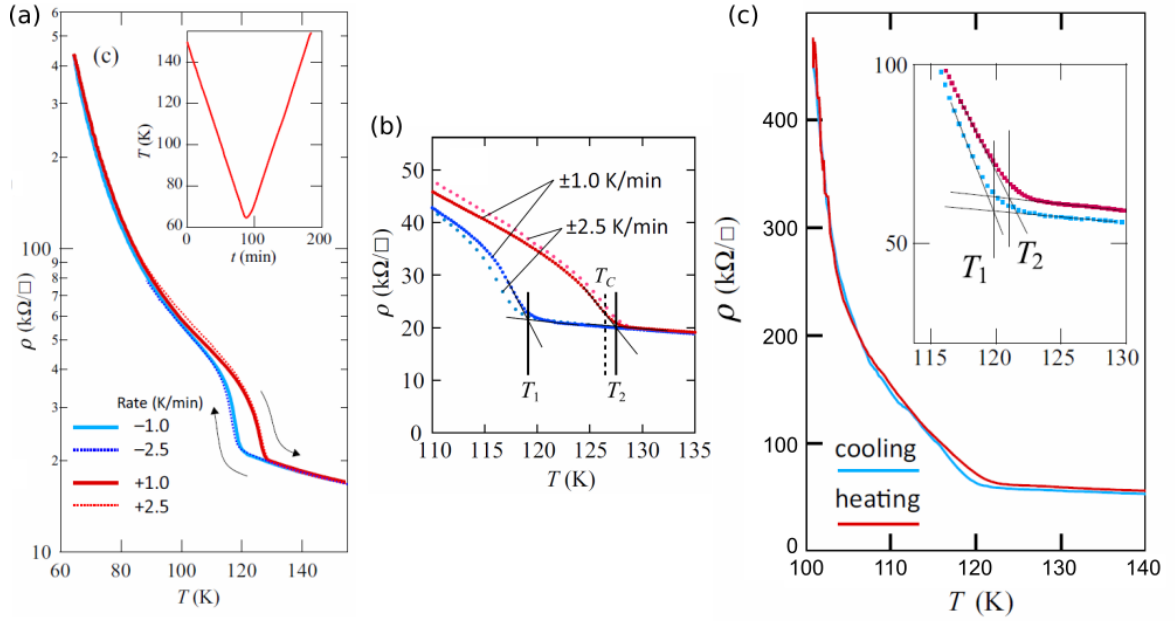


Figure 2.10: (a) Transport data acquired on a triple-domain In/Si(111) sample during cooling (blue) and heating (red) at rates of ∓ 1.0 K/min (solid curves) and ∓ 2.5 K/min (dotted curves). Inset shows the temperature change for ∓ 1.0 K/min. (b) Closeup of (a) around $T = 120$ K. The temperatures of the rising edges are highlighted (solid black lines) as well as $T_c \approx 126.5$ K (dashed black line). (c) $\rho(T)$ curves for a single-domain sample with a substrate miscut of 2° measured at a rate of 1.2 K/min. The inset shows a closeup around $T = 120$ K and the positions of T_1 and T_2 . All images are taken from Ref. [88].

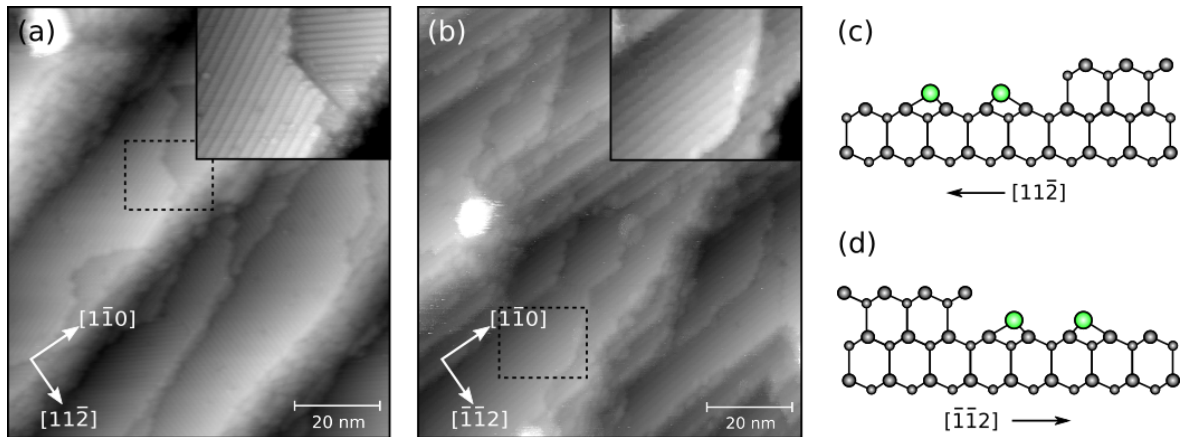


Figure 2.11: RT STM images of (4×1) -In on vicinal substrates with opposite miscut direction, namely (a) 4° in $[11\bar{2}]$ ($V = -1.1$ V, $I = 60$ pA) and (b) 6° in $[\bar{1}12]$ ($V = -1.5$ V, $I = 100$ pA). Insets are close-up images of the areas indicated by dashed rectangles displaying either three rotational domains or a single-domain structure. (c) and (d) Structural models corresponding to the two miscut directions, adapted from [97]. Green and gray balls are indium or silicon atoms, respectively.

In general, the thermal hysteresis behavior in first-order phase transitions is due to the slow kinetics relative to the quick change in temperature during the measurement [96]. Hence, for a homogeneous nucleation process of both the high- and low-temperature phase, the onset of the phase transition shifts to lower temperatures during cooling, i.e., supercooling, and to higher temperatures during heating, leading to a superheating behavior.

In the case of In/Si(111), the supercooling is indeed observed, since the (8×2) reconstruction nucleates homogeneously inside the (4×1) domains. On the other hand, upon heating, the phase transition starts significantly below T_c , and it is almost completed at T_c ; thus, the superheating is mostly suppressed [88]. Therefore, the shift of T_2 to a value close to T_c (see Fig. 2.10 (b)) occurs due to a heterogeneous nucleation process during heating. Surface steps that are present even at nominally flat surfaces act as a source for this heterogeneity. In the vicinity of steps, the interchain coupling between neighboring (4×1) chains is altered, which leads to a local destabilization of the (8×2) phase. Thus upon heating, the chains close to a step undergo the phase transition at lower temperatures compared to flat areas, and with increasing temperature, the (4×1) domains gradually expand into the terraces [88, 100].

As a proof for this assumption, transport measurements with a linear probe arrangement were carried out using a slightly vicinal substrate, i.e., 2° miscut from $[111]$ towards the $[\bar{1}\bar{1}2]$ direction, that exhibits a single-domain (4×1) -In reconstruction at RT (see Fig. 2.10 (c)). Indeed, due to the higher density of steps compared to the nominally flat surface (Fig. 2.10 (b)), the phase transition temperature during heating T_2 decreases significantly by more than 6 K to value of 121 K, while T_1 stays almost constant. Hence the hysteresis width decreases as well [88].

The research on this topic was continued in the course of this thesis. Using an even more inclined substrate with a miscut of 4° towards the $[\bar{1}\bar{1}2]$ direction, transport measurements revealed an additional effect of the surface steps on the formation of the (8×2) phase during cooling (see chapter 5). Since the low-temperature phase preferentially nucleates inside the (4×1) domains, this influence is only detectable for sufficiently small terraces.

2.3 Spin-orbit density wave

A rather exotic and yet quite unacquainted phenomenon in surface science is the so-called spin-orbit density wave (SODW). The theoretical description was first proposed in 2012 by P. Riseborough [101, 102] and T. Das [103] as an explanation for the “hidden-order” phase of the heavy fermion metal URu₂Si₂ [104–106]. Subsequently, it was extended to 2D electron gases, such as the surface state of BiAg₂ [107, 108], and was eventually applied to quasi-1D nanowires like Pb/Si(557) [41, 109]. Basically, the theory predicts the formation of a finite insulating gap owing to the interplay of SOC and electronic interactions, which will be explained in more detail in the following, according to a review paper by T. Das [110].

The previous chapter 2.2 already gave insight into the formation of a CDW due to electron-phonon interaction. In this connection, a band gap is opened at the edge of the reduced SBZ obeying the relation $G = 2k_F$, where k_F is the Fermi wavenumber. G is the reciprocal wavevector corresponding to the potential V_G that deforms the lattice, which is called Fermi surface nesting vector.

The situation leading to the formation of a SODW as a ground state is similar to a certain degree. In this more exotic case, Fermi surface nesting occurs between two SOC split bands.

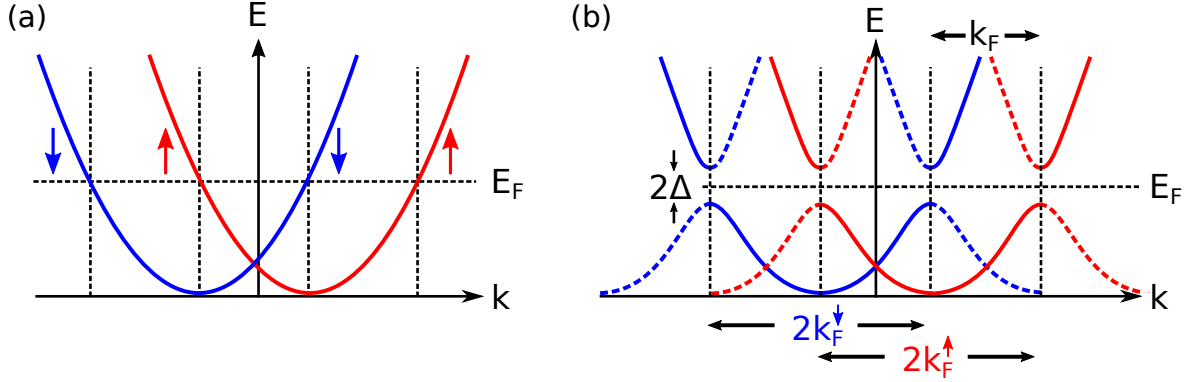


Figure 2.12: (a) Bandstructure of free Rashba bands with opposite spin polarization \uparrow (red) and \downarrow (blue). (b) Correlated bandstructure with SODW. If two Fermi surface nestings simultaneously occur between the two helical states, a band gap 2Δ is opened and the SBZ is resized. Backfolded bands are drawn with dashed lines. Adapted from [110].

The resulting distinct order parameter is the SODW, which breaks the translational symmetry while preserving time-reversal symmetry in most cases. The SODW arises in different orbitals which are entangled to each other by the intrinsic SOC of the system [109]. This scenario is schematically drawn in Fig. 2.12.

Thus, the occurrence of the SODW is limited to systems displaying intrinsic SOC with the presence of at least two spin-orbit split bands. Furthermore, SOC strength needs to be larger than the inter-orbital Coulomb strength in order to prevent the formation of a typical spin density wave (SDW). Nevertheless, the Coulomb interaction has to exceed a non-zero critical value [109]. The SODW strength is represented by the size of the band gap 2Δ . Unlike in, e.g., topological insulators, zero gapping does not exist. Instead, a finite gap protects the SODW phase against external perturbations and spin dephasing [107]. By this means, the spin order of the system is quite robust, while the spin polarization is tunable via electronic correlation strength [109].

A system hosting a SODW at low temperatures is Pb/Si(557), which switches reversely from a 2D weakly anisotropic temperature activated conductance regime to a quasi-1D metallic state in the direction parallel to the nanowires upon cooling below a critical temperature of $T_c \approx 78$ K [42, 111]. It is caused by the local (223) surface orientation induced by a Pb coverage of 1.3 ML. This introduces a new reciprocal lattice vector $g = 2\pi/d = 0.4 \text{ \AA}^{-1}$ in the direction perpendicular to the nanowires, with the distance $d = 1.58$ nm between adjacent Pb nanowires. It fulfills the nesting condition $2k_F = g$ between the spin-polarized bands. Furthermore, spin polarized ARPES measurements revealed the quasi-Fermi surface, i.e., the constant energy map (CEM) at finite energies close to E_F , is governed by Pb induced surface states, which are elliptically shaped and show an alternating spin texture with a pronounced Rashba-splitting of $\Delta k = 0.2 \text{ \AA}^{-1}$ in $[11\bar{2}]$ direction, that exactly corresponds to $g/2$ (see Figs. 2.13 (a) and (b)) [112, 113]. This leads the formation of a SODW, which opens up a transport gap in the order of $2\Delta = 20$ meV in the direction perpendicular to the nanowires [112]. The resulting SBZ shown in Fig. 2.13 (d) includes replica bands from all $\bar{\Gamma}$ points [41].

The robustness of the SODW phase against external perturbations was confirmed by adding small amounts of Pb excess coverage. As shown in Fig. 2.13 (c), the correlated spin-orbit

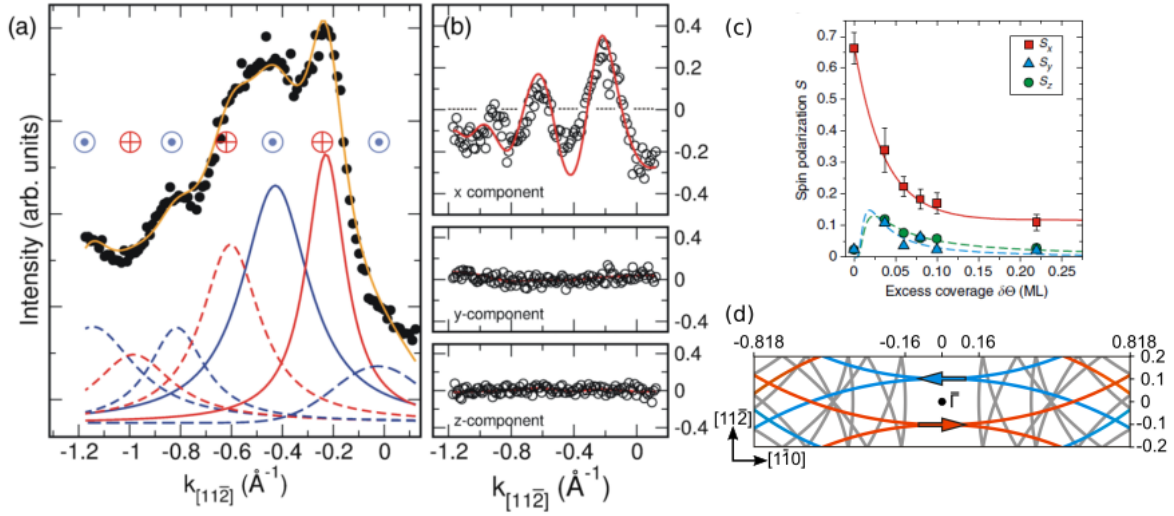


Figure 2.13: (a) Momentum distribution curve of Pb/Si(557) measured at $E = E_F - 100$ meV along the $[11\bar{2}]$ direction. (b) Spin polarization components obtained with Mott detectors. Panel (a) and (b) are taken from Ref. [113]. (c) Peak-to-peak maximum values of the three spin polarization components as a function of excess coverage; taken from Ref. [41]. (d) Quasi-Fermi surface of 1.3 ML Pb/Si(557) including replica bands from all $\bar{\Gamma}$ points; adopted from [41].

ordering remains robust up to $\Delta\theta = 0.2$ ML [41].

Within the scope of this thesis, the structural and electronic properties of the 1.3 ML Pb phase on Si(557) were further investigated by means of STM and STS (cf. chapter 8). A new structural model is proposed based on high-resolution STM images, which additionally gives insight into the adsorption sites of excess Pb atoms. The adsorption of $\Delta\theta = 0.2$ ML Pb induces a metallic state in the vicinity of the step edge, eventually leading to a break-down of the insulating SODW state at low temperatures.

Experimental methods

This chapter introduces the main experimental methods used in the course of this thesis. These are scanning tunneling microscopy (chapter 3.1), low energy electron diffraction (chapter 3.2), as well as spin- and angle-resolved photoemission spectroscopy (chapter 3.3).

3.1 Scanning tunneling microscopy

For gaining insight into structural properties on the atomic scale, the scanning tunneling microscope (STM) is a commonly used technique. Since its invention in 1981 by Binnig and Rohrer [114, 115], it has become indispensable for surface science investigations. The basic working principle will be explained in the following.

During STM measurements, a sharp metal tip scans at a defined distance above the sample, as shown in Fig. 3.1 (a). By applying a bias voltage V between tip and sample, a so-called tunneling current I is flowing. The electrons contributing to it overcome the potential barrier, caused by the finite distance separating tip and sample, due to the quantum mechanical tunnel effect. If a negative bias is applied, electrons tunnel from the sample's filled states to the empty states of the tip; for a positive bias, the current flows from the tip's filled states to the sample's empty states. The latter case is schematically depicted in Fig. 3.1 (b), assuming a distance d between tip and sample.

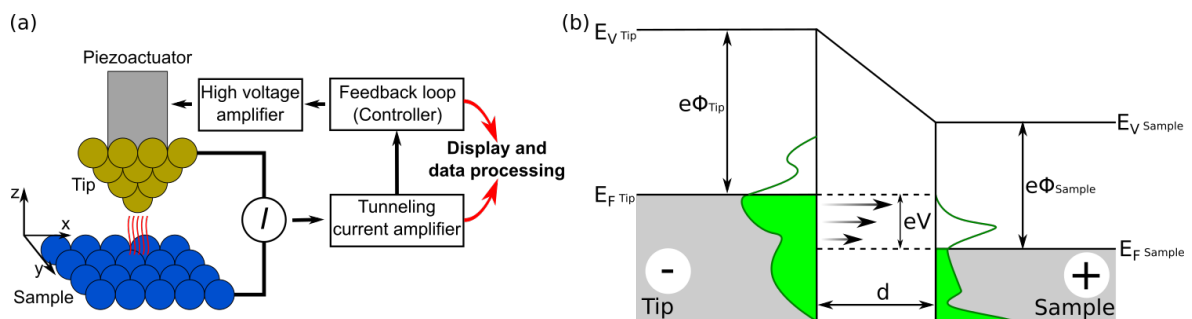


Figure 3.1: (a) Schematic drawing of the basic components of a STM. (b) Schematic potential diagram in case of a positive bias applied to the sample. Both pictures are adapted from [116]

3.1.1 Tunneling current

In order to calculate the tunneling current, the tunneling probability τ of elastic tunneling processes has to be considered. It depends on the tunneling matrix element $M_{\mu\nu}$ [117], which describes the electron's transition probability to change between states ψ_μ to ψ_ν with energies E_μ and E_ν , respectively, following the relation

$$\tau = \frac{2\pi}{\hbar} |M_{\mu\nu}|^2 \delta(E_\mu - E_\nu) \approx \frac{16E(\phi - E)}{\phi^2} \exp(-2\kappa d). \quad (3.1.1)$$

The right side of this equation approximates τ in terms of the quantum mechanical transmission probability of an electron with energy E tunneling through a barrier having a width d and a average height

$$\phi = \frac{\phi_{\text{tip}} + \phi_{\text{sample}}}{2}, \quad (3.1.2)$$

depending on the workfunctions ϕ_{tip} and ϕ_{sample} of tip and sample. The inverse decay length is given by

$$\kappa = \sqrt{\frac{2m\phi}{\hbar^2} - E + \frac{eV}{2}}. \quad (3.1.3)$$

It clearly shows the current's exponential dependence on the tip height, since this defines the barrier width in the case of a STM. The measuring mode that was mainly used within the scope of this thesis, the so-called constant current mode, is thus able to detect even small deviations in the distance between tip and sample. Accordingly, the tip height is adjusted via a feedback loop that regulates piezo elements in order to keep the current constant. Thus, the acquired STM image is based on the feedback loop signals.

Assuming low temperatures and small biases, I is simplified to [118–120]

$$I(V) = \frac{4\pi}{\hbar} e^2 V \sum_{\mu\nu} |M_{\mu\nu}|^2 \rho_{\text{tip}} \rho_{\text{sample}}. \quad (3.1.4)$$

Here, ρ_{tip} and ρ_{sample} are the local density of states (LDOS) of the tip or the sample at E_F , respectively. Further simplification is done by assuming ρ_{tip} to be constant, which is reasonable for single atomic metallic tips, resulting in [120]

$$I(V) \propto \int_0^{eV} \rho_{\text{sample}}(E) \tau(E, eV) dE. \quad (3.1.5)$$

Hence, the tunneling current depends only on the bias voltage V , energy E and the LDOS of the sample ρ_{sample} . Since the the tunneling parameters I and V can be accurately determined during STM measurements, the acquired topographic images resemble the spatially resolved integrated LDOS of the sample.

3.1.2 Scanning tunneling spectroscopy

A second technique a STM can be used for is scanning tunneling spectroscopy (STS). It gives more insight in the LDOS of the sample. For acquisition of STS data, the tip is placed at a specific position, and the bias voltage is ramped over a certain voltage range, while the

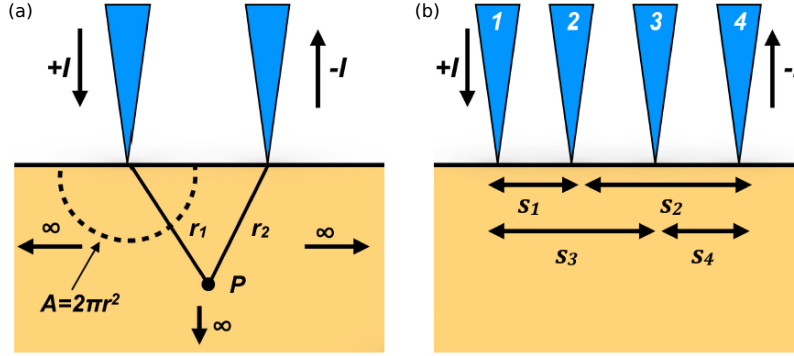


Figure 3.2: Sketch of the (a) 2pp and (b) 4pp transport measurement in a collinear arrangement with equidistant probe spacing. Images are taken from Ref. [122].

tunneling current I is measured. In this case, the feedback loop is open, since the tip is supposed to remain at the same height. According to Equation 3.1.5, the measured $I(V)$ curves are proportional to the integrated LDOS of the sample. Hence, its derivative

$$\frac{dI}{dV} \propto e\rho_{\text{sample}}(eV)\tau(eV, eV) + \int_0^{eV} \rho_{\text{sample}}(E) \frac{d}{d(eV)} \tau(E, eV) dE \quad (3.1.6)$$

gives access to the LDOS [120, 121]. It is usually acquired using a Lock-In technique, that yields a better signal-to-noise ratio than numerical calculations. However, it diverges exponentially both in V and d , which tends to mask the LDOS features [121]. In order to eliminate this, the ratio of differential to total conductivity is calculated,

$$\frac{dI/dV}{I/V} \propto \frac{\rho_{\text{sample}}(eV) + \int_0^{eV} \frac{\rho_{\text{sample}}(E)}{\tau(eV, eV)} \frac{d}{d(eV)} (\tau(E, eV)) dE}{\frac{1}{eV} \int_0^{eV} \rho_{\text{sample}}(E) \frac{\tau(E, eV)}{\tau(eV, eV)} dE}, \quad (3.1.7)$$

where $\tau(E, eV)$ and $\tau(eV, eV)$ appear as ratios and tend to cancel their exponential dependences on the voltage and distance [121]. The second term in the numerator is a background term, while the denominator provides a normalization of the LDOS. For $V > 0$, all terms of Equation 3.1.7 are in the same order of magnitude, resulting in a normalized LDOS with slowly varying background. In case of $V < 0$, both the denominator and the background term are in the same order of magnitude, which is larger than the LDOS term. Thus, especially low-lying filled surface states are difficult to probe by means of STS [121].

3.1.3 4pp transport measurements

A further application of STM is the use of the tips as an ohmic contact for measuring transport properties of solids. The data of the (4×1) -In/Si(111) reconstruction discussed in chapter 5 was acquired by a four-point probe (4pp) STM (cf. chapter 4.3), where either two or all four probes served as a contact in order to determine the resistance R of a sample.

Although two-point probe (2pp) measurements seem to be more intuitive as 4pp, the latter is more precise. During a 2pp measurement, the two probes simultaneously impinge a current I and measure the corresponding voltage drop V , as sketched in Fig. 3.2 (a). Indeed, this

method does not only measure the sample resistance R_{sample} , but includes the resistances of the probes R_{probe} and the contacts R_{contact} as well, following the relation

$$R = \frac{V}{I} = 2R_{\text{probe}} + 2R_{\text{contact}} + R_{\text{sample}}. \quad (3.1.8)$$

Hence, the knowledge of R_{probe} and R_{contact} is necessary for determining the exact value of R_{sample} . However, they usually can only be estimated as they differ for every contacting.

In the 4pp case, the probes only either serve as a current injecting probe, or they measure the voltage drop (see Fig. 3.2 (b)). As for the latter, the current flowing through is basically zero, and the measured resistance is equal to the R_{sample} . Therefore, with a 4pp configuration, the resistance of the sample can be determined much more precisely than in a 2pp measurement, and it will be preferentially used in the following.

Furthermore, if the geometry of the examined sample as well as R_{sample} is known, intrinsic properties such as the resistivity ρ or the conductivity $\sigma = 1/\rho$ can be calculated. For the systems investigated within this thesis, the surface was covered by quasi-1D nanowire-like structures, and thus it was highly anisotropic. This means, that ρ is not a scalar, but is rather represented by three values ρ_x , ρ_y and ρ_z oriented along the x -, y - and z -axis of the sample. Since the used silicon substrates are semi-conducting, the surface is considered to be an infinite 2D sheet. Depending on the arrangement of the four probes, i.e., if they are aligned linearly or as a square, the resistance measured in e.g. x -direction is described by the equations [122]

$$R_{x,\text{linear}} = \frac{\ln 2}{\pi t} \sqrt{\rho_x \rho_y} \quad (3.1.9)$$

$$R_{x,\text{square}} = \frac{\sqrt{\rho_x \rho_y}}{2\pi t} \ln \left(1 + \frac{\rho_x}{\rho_y} \right), \quad (3.1.10)$$

where t is the thickness of the sheet. In order to quantify the anisotropy present on the surface, the resistance ratios R_x/R_y are calculated. As evident from Equation 3.1.9, for the linear arrangement this value is always equal to 1, therefore this setup is not suitable for determining the anisotropy. For the square arrangement, it results in

$$\frac{R_x}{R_y} = \frac{\ln(1 + \rho_x/\rho_y)}{\ln(1 + \rho_y/\rho_x)}. \quad (3.1.11)$$

Because of that, in order to gain insight in the anisotropy degree of a 2D surface by 4pp measurements, the probes have to be arranged in a square geometry.

Rotational square method

For most samples measured by 4pp measurements, it is not easy to align the probes accurately along the principal axes of the anisotropic surface. However, this is needed for Equation 3.1.11. An advanced approach is the rotational square method [123], which is more suitable for calculating the correct values of the resistivity components even for unknown anisotropy orientations.

As depicted in Fig. 3.3 (a), for the rotational square method, a 4pp square arrangement is rotated by an arbitrary angle θ with respect to the orientation of the resistivity directions ρ_x

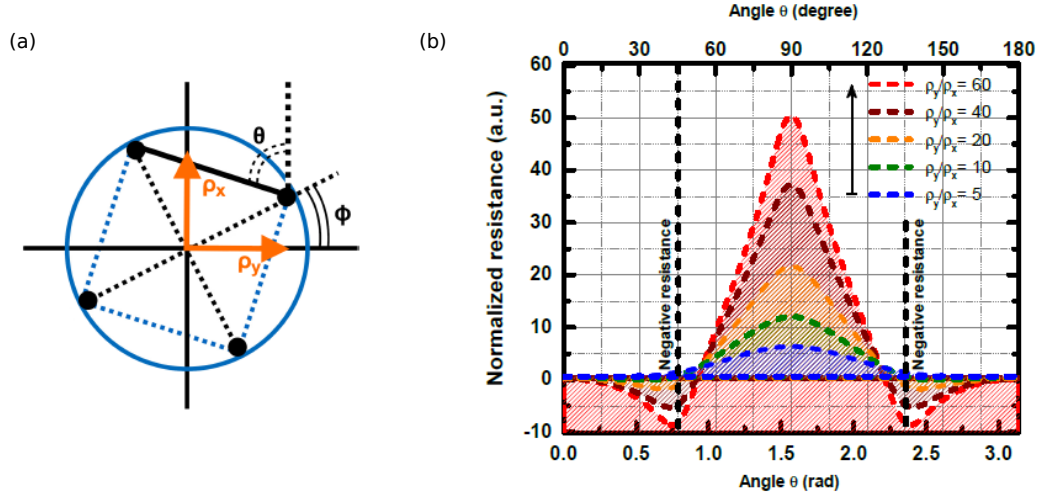


Figure 3.3: (a) Sketch of a 4pp square arrangement rotated by an angle $\theta = \phi + 45^\circ$ with respect to the orientation of the resistivity directions ρ_x and ρ_y [124]. (b) Dependence of the resistance on the angle θ for an anisotropic infinite 2D sheet with various anisotropy degrees ρ_y/ρ_x . Images are taken from Ref. [122].

and ρ_y . The measured resistance $R(\rho_x, \rho_y, \theta)$ is now defined by the equation [122, 123]

$$R(\rho_x, \rho_y, \theta) = \frac{\sqrt{\rho_x \rho_y}}{2\pi t} \ln \sqrt{\frac{\left(1 + \frac{\rho_y}{\rho_x}\right)^2 - 4 \cos^2 \theta \sin^2 \left(1 - \frac{\rho_y}{\rho_x}\right)^2}{\left(\sin \theta + \frac{\rho_y}{\rho_x} \cos^2 \theta\right)^2}}. \quad (3.1.12)$$

Exemplary for some resistivity anisotropy ratios, the resulting resistances are plotted in Fig. 3.3(b). As obvious, the highest anisotropy is expected, if the square is aligned with respect to the orientation of ρ_x and ρ_y , i.e., for $\theta = 0$ and $\theta = 90^\circ$. Furthermore, for high anisotropy ratios $\rho_y/\rho_x > 5 + 2\sqrt{6} \approx 9.9$, a negative resistance is present for some values of θ , which is explained by a deformation of the electrostatic potential [123].

Space charge layer

For n-type doped silicon substrates, which are used for the measurements presented in the course of this thesis, it is well-known that surface states are decoupled from the bulk due to the Schottky barrier [125]. However, it turned out that mobile excess charge carriers are accumulated in the region close to the surface, forming the so-called space charge layer (SCL), which alters the surface-near carrier concentration [25–27]. Especially for transport measurements performed on atomically thin films adsorbed on these surfaces, it can have a major impact on the acquired data, i.e., the conductivity of the sample. It will be explained in the following based on the description published in [27, 124].

In general, the measured conductivity σ is the sum of all contributing current channels [123, 126]

$$\sigma = \sigma_S + \sigma_{SCL} + \sigma_B. \quad (3.1.13)$$

Here, σ_S is due to the surface state bands originating from the topmost atomic layer, σ_{SCL} stems from the SCL, and σ_B is the bulk contribution. In the course of surface science investigations, primarily σ_S is desirable to determine. For quasi-1D systems such as the (4×1) -In/Si(111) reconstruction (cf. chapter 5), this is done by evaluating the conductivity σ_{\perp} , that is measured in the direction perpendicular to the nanowires. Thus, σ_{\perp} has no contribution from the surface state, i.e., $\sigma_S \approx 0$ in this direction, but is caused completely by the bulk and SCL components.

The bulk-related conductivity σ_B is characterized by activated transport via bulk defects. This isotropic hopping channel is modeled by a Boltzmann term,

$$\sigma_B \propto \exp\left(-\frac{\Delta_B}{k_B T}\right), \quad (3.1.14)$$

that includes the activation energy Δ_B . The second term needed for a precise determination of the surface state conductivity, namely the space charge layer contribution, is actually described by the sum of two parts,

$$\sigma_{SCL} = \sigma_{iSCL} + \sigma_{pSCL}. \quad (3.1.15)$$

The first one, σ_{iSCL} , is due to the intrinsic SCL, the latter one (σ_{pSCL}) is the contribution from the so-called parasitic sub-surface p-type SCL. The intrinsic SCL essentially depends on the substrate doping, i.e., on the donor or acceptor concentration. It is caused by the transferring of electrons from the bulk into the surface states or vice versa, depending on the Fermi level at the surface and the type of surface states, i.e., acceptor or donors. The resulting charge transfer is screened by an equivalent charge within the bulk material, hence the iSCL is formed in the sub-surface region. It is calculated using the formula

$$\sigma_{iSCL} = e(\mu_p \Delta p + \mu_n \Delta n), \quad (3.1.16)$$

where Δn and Δp are the electron and hole concentrations across the iSCL, namely

$$\Delta n = \int_0^{\infty} (n_i \exp(u(z)) - N_D) dz \quad (3.1.17)$$

and

$$\Delta p = \int_0^{\infty} (n_i \exp(-u(z)) - N_A) dz, \quad (3.1.18)$$

with the donor and acceptor concentration N_D and N_A , the intrinsic carrier concentration

$$n_i = 2 \left(\frac{m^* k_B T}{2\pi \hbar^2} \right)^{3/2} \exp\left(-\frac{E_g}{2k_B T}\right) \quad (3.1.19)$$

and the band gap energy E_g of the silicon substrate. Its mobilities, μ_n and μ_p , depend on the temperature T and, in case of n-doped silicon substrates, the donor concentration N_D (in cm^{-3}) present in the substrate, and are approximated by [127]

$$\mu_n(T, N_D) = 88 \left(\frac{T}{300} \right)^{-0.57} + \frac{7.4 \times 10^8 T^{-2.33}}{1 + \left(N_D / 1.26 \times 10^{17} \left(\frac{T}{300} \right)^{2.4} \right) 0.88 \left(\frac{T}{300} \right)^{-0.146}} \quad (3.1.20)$$

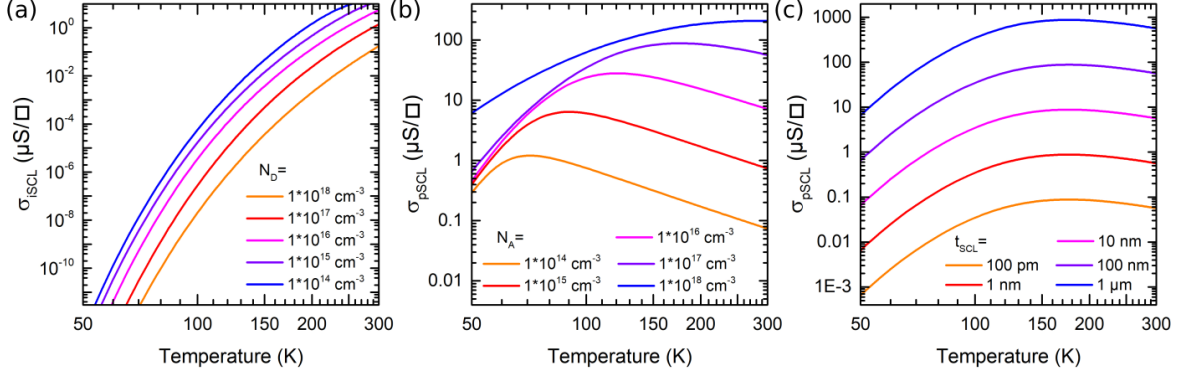


Figure 3.4: Exemplary plots showing the dependence of (a) σ_{iSCL} on the donor concentration of the bulk, N_{D} , and σ_{pSCL} on (b) the acceptor concentration in the sub-surface layer, N_{A} , with a given space charge layer thickness of $t_{\text{SCL}} = 100 \text{ nm}$ and (c) t_{SCL} with $N_{\text{A}} = 1 \cdot 10^{-17} \text{ cm}^{-3}$.

and

$$\mu_{\text{p}}(T, N_{\text{D}}) = 54.3 \left(\frac{T}{300} \right)^{-0.57} + \frac{1.36 \times 10^8 T^{-2.23}}{1 + \left(N_{\text{D}} / 2.35 \times 10^{17} \left(\frac{T}{300} \right)^{2.4} \right) 0.88 \left(\frac{T}{300} \right)^{-0.146}}. \quad (3.1.21)$$

In order to highlight the dependence of σ_{iSCL} on the donor concentration of the bulk, exemplary curves of $N_{\text{D}} = 1 \cdot 10^{18} - 1 \cdot 10^{14} \text{ cm}^{-3}$ are plotted in Fig. 3.4(a). For n-type doped Si substrates, the curves correspond to substrate resistivities in the range of 0.01 to 100 Ωcm .

The parasitic sub-surface p-type SCL is evoked by high temperature flash annealing of the bare Si substrate, mainly done as a cleaning step prior to the nanowire growth. This leads to irreversible changes of the doping type and its concentration [26], i.e., the former n-type doping is locally replaced by a p-type layer, due to either boron diffusion or incorporation of carbon contaminations as interstitial defects [77, 128]. The concentration of these acceptors $N_{\text{A}}(t)$ decays exponentially towards the bulk,

$$N_{\text{A}}(t) = N_{\text{A}} \exp\left(-\frac{t}{\lambda}\right), \quad (3.1.22)$$

with the concentration at the surface N_{A} , the thickness t , and the decay constant λ that is considered to be equal to the pSCL layer thickness t_{SCL} , if N_{A} is large compared to the intrinsic n-type concentration N_{D} . The hole concentration p as a function of t is modeled by [129]

$$p(T, t, N_{\text{A}}) = \frac{N_{\text{A}}(t)}{1 + \left(4 + 2 \exp\left(-\frac{\Delta}{k_{\text{B}}T}\right) \right) \exp\left(\frac{E_{\text{A}} - E_{\text{F}}}{k_{\text{B}}T}\right)}, \quad (3.1.23)$$

where E_{A} is the acceptor energy and Δ is an empiric constant of the type of contamination causing the p-type layer. By integration of the thickness t for capturing the depth distribution of the acceptor states, the sheet conductivity σ_{pSCL} yields

$$\sigma_{\text{pSCL}} = e \int_0^{\infty} \mu_{\text{p}}(T, t, N_{\text{A}}) p(T, t, N_{\text{A}}) dt. \quad (3.1.24)$$

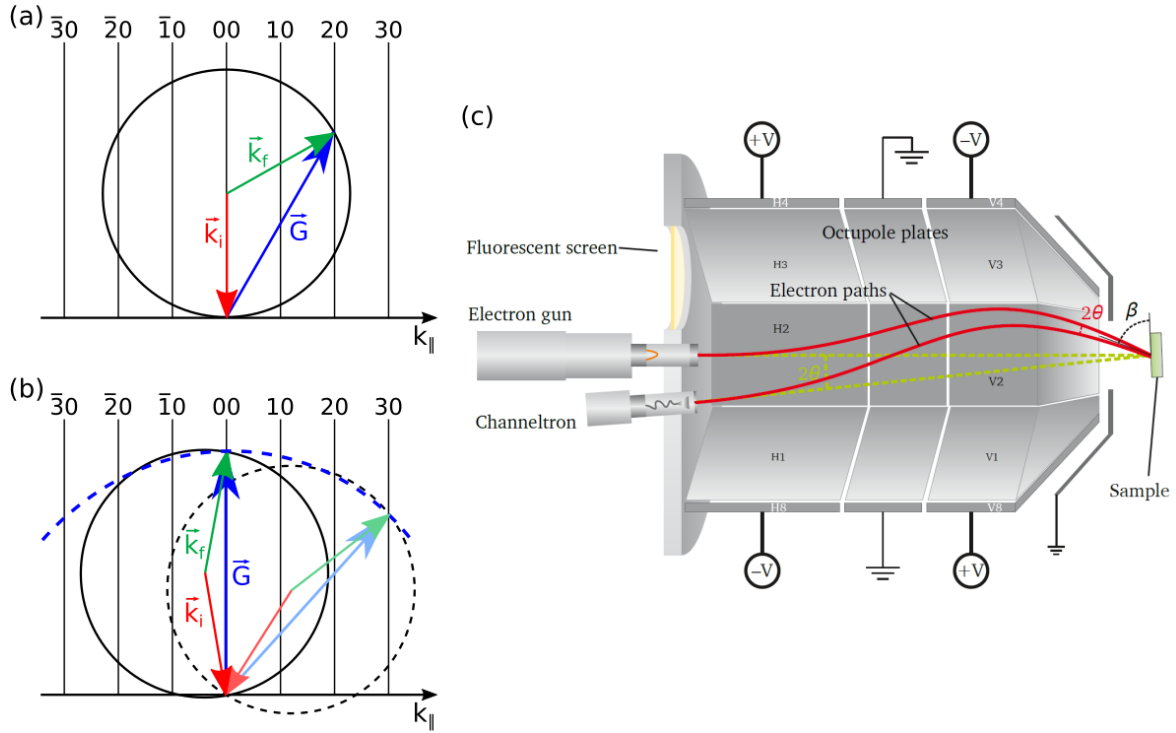


Figure 3.5: (a) Ewald construction and (b) its modified version depicting the scattering conditions applicable for optical LEED and SPALeED, respectively. (c) Schematic drawing of the SPALeED setup; taken from Ref. [130].

In this connection, Equation 3.1.21 was used for the determination of $\mu_p(T, t, N_A)$ with the substitution of N_D by $N_A(t)$. For visualization of the influence of the acceptor concentration present in the sub-surface layer as well as the space charge layer thickness on the conductivity σ_{pSCL} , exemplary curves varying either one are shown in Figs. 3.4 (b) and (c). Accordingly, the shape of σ_{SCL} is significantly changed by modification of N_A , while an increase of t_{SCL} merely leads to a shift to higher conductivity values.

3.2 Low energy electron diffraction

In the course of this theses, low energy electron diffraction (LEED) was mainly used for checking the sample quality after the preparation of nanowire ensembles. It allows the determination of periodic structures on surfaces.

As already implied by the technique's name, electrons with low energies, i.e., in the range of 20 – 300 eV, are accelerated from a filament and diffracted on the sample, giving rise to a diffraction pattern on a phosphorus screen [131]. It is very surface sensitive since the mean free path of these electrons in solids is only 0.6 to 1 nm [132]. The electrons' wavelength calculated by [133]

$$\lambda(\text{\AA}) = \frac{h}{\sqrt{2m_e E(\text{eV})}} \approx \sqrt{\frac{150.4 \text{ eV}}{E(\text{eV})}}, \quad (3.2.1)$$

are in the order of atomic distances. Thus, the technique is indeed suitable for investigations on surface symmetries and possible superstructures of surface reconstructions. The resulting diffraction spots obey to the Laue equation

$$\vec{K} = \vec{k}_f - \vec{k}_i = \vec{G}, \quad (3.2.2)$$

that describes the relationship between the wavevector of the incoming and outgoing electron, \vec{k}_i and \vec{k}_f , respectively. \vec{K} is the scattering vector, and \vec{G} the reciprocal lattice vector of a 2D lattice. Due to the surface periodicity, the part of \vec{K} , which is parallel to the surface, i.e., \vec{K}_{\parallel} , is only allowed to have discrete values. However, the perpendicular one, \vec{K}_{\perp} , is continuous, caused by the lack of periodicity in this direction. This results in the so-called lattice rods in reciprocal space. The diffraction spots seen in LEED can be determined by the Ewald construction, depicted in Fig. 3.5 (a). At the crossing points of the Ewald sphere and the lattice rods, a diffraction spot appears.

Two different types of this measurement technique were used in the scope of this thesis, namely the optical LEED and the spot profile analysis LEED (SPALEED). In the case of the former, the setup consists of a hot filament emitting electrons towards the sample. After diffraction, the electrons are filtered by grids that are passed only by elastically diffracted electrons, which are then accelerated on a phosphorus screen. In contrast to that, in SPALEED the angle between incoming and outgoing electron beam is kept constant, while the electrons follow a path determined by octopole plates (cf. Fig. 3.5 (c)). The scattering conditions are slightly changed, generating a modified Ewald sphere, which is rolled out by changing the octupole voltages, see Fig. 3.5 (b). The modified Ewald sphere is doubled in size; thus, the SPALEED has larger access to reciprocal space. A further advantage of the SPALEED technique compared to optical LEED is the possibility to analyze the profile of the (00) diffraction spot, that is hidden by the filament in the optical case.

3.3 Spin- and angle-resolved photoelectron spectroscopy

Today, many techniques in solid state physics are based on the photoelectric effect [134–136]. Common examples are X-Ray photoemission spectroscopy (XPS) for analyzing the chemical composition or angle-resolved photoemission spectroscopy (ARPES) for mapping electronic band structures. The latter was used in the scope of this thesis. Here, photons with an energy $h\nu$ hit a sample, while the kinetic energy E_{kin} of the resulting photoelectrons are analyzed. According to the relation

$$E_B = h\nu - E_{\text{kin}} - \phi \quad (3.3.1)$$

the binding energy E_B of the photoelectron is calculated. Here, ϕ is the work function of the sample. By rotation of the sample, a wide range in reciprocal space is accessible. Thus, the band dispersion of the filled states is mapped. Moreover, different light polarizations, such as linear (s or p) or circular (C^+ or C^-) can be used, e.g. in order to enhance the band intensities.

Further development of this technology led to the possibility of studying the spin structure of a material by using the so-called spin-resolved photoelectron spectroscopy. First experiments dealing with spin-polarized photoelectrons were performed after the theoretical prediction of U. Fano in 1969 [137]. The *Fano effect* describes the ejection of spin-polarized

electrons from a cesium atom by circularly polarized light, or, more generally, the spin-polarized photoemission on non-magnetic systems. He later named the reason for this effect *spin-orbit coupling* [138].

The following sections go into detail about the Rashba effect resulting in spin-polarized bands as well as the influence of light polarization on the acquired SARPES data, with particular focus on sample exhibiting a mirror axis.

3.3.1 Rashba effect

The Rashba effect is a momentum-dependent spin-splitting of the band structure caused by 2D systems [139, 140].

Since inversion symmetry in both space and time leads to spin degenerate electron and hole states, the Rashba effect is present only in case of asymmetry of the crystal potential. Such an inversion asymmetric potential exists, e.g., in the direction perpendicular to the crystal's surface. A schematic picture of the Rashba effect demonstrated on parabolic energy bands is displayed in Fig. 3.6. The formerly degenerated states are shifted by $\Delta E = \pm\alpha\hbar k$, leading to a constant energy surface consisting of concentrically shaped spin-polarized circles. The resulting Hamilton operator [141],

$$\hat{H}_{\text{Rashba}} = \alpha (\mathbf{E} \times \vec{k}) \cdot \hat{\sigma}, \quad (3.3.2)$$

contains the unit vector of the electric field \mathbf{E} , which corresponds to the gradient of the potential and thus is perpendicular to the surface, the Pauli matrices $\hat{\sigma} = (\sigma_x, \sigma_y, \sigma_z)$, as well as the Rashba parameter α , which quantifies the strength of the Rashba effect. The latter is proportional to the parameter of the atomic SOC λ , [142], and consequently follows $\alpha \propto \Delta_{\text{SO}}$ (cf. Equation 2.1.7).

In the scope of this thesis, two material systems displaying Rashba-split surface states are discussed, namely Sn/Si(111) and Pb/Si(557) (see chapters 6 and 8). The spin-orbit gaps Δ_{SO} of Sn and Pb are 0.8 eV and 2.0 eV, respectively [67, 68]. Hence the spin-splitting of the insulating surface state due to the Rashba effect is expected to be smaller in case of Sn/Si(111) as the value of $\Delta k_{\text{Pb/Si(557)}} = 0.2 \text{ \AA}^{-1}$ [113] for Pb/Si(557). This was confirmed by SARPES measurement yielding $\Delta k_{\text{Sn/Si(111)}} \approx 0.05 \text{ \AA}^{-1}$.

However, for systems with half-filled surface states, whose curvature severely effects the effective mass of the charge carriers close to E_{F} , higher-order terms have to be included as a correction to the linear Rashba model. For instance, the SIC-Pb/Si(111) phase shows an unconventionally small Rashba-splitting of $k_{\text{Pb/Si(111)}} \approx 0.04 \text{ \AA}^{-1}$, which is attributed to the anisotropic effective mass of the surface state having strongly reduced values with respect to the nearly-free electron gas [143, 144].

3.3.2 Influence of light polarization

Up to 1987, it was a common belief that only circularly polarized light could be used to eject spin-polarized electrons from single atoms or surfaces (e.g., [146, 147]). This was proven wrong by Tamura et al. [148–150], who did theoretical calculations based on symmetry arguments and experiments with circularly, linearly, and unpolarized light. With all three kinds of light, they were able to observe emission of spin-polarized electrons on metallic surfaces.

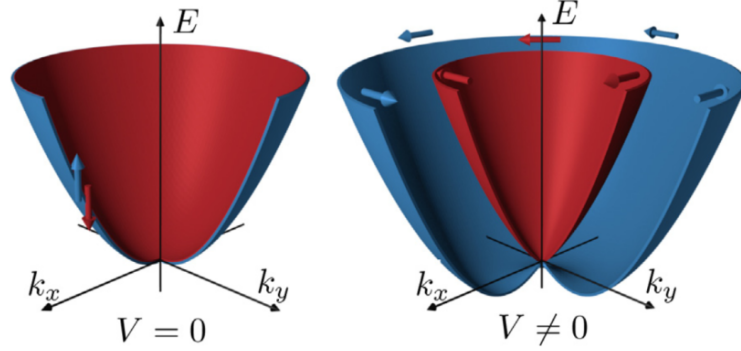


Figure 3.6: Parabolic energy bands: In the presence of inversion and time reversal symmetries they are spin-degenerate (left). If the inversion symmetry perpendicular to the plane is broken by an external electrostatic potential $V \neq 0$ a Rashba-splitting occurs. In this case the spins are momentum dependent due to SOC (right). Image is taken from Ref. [145].

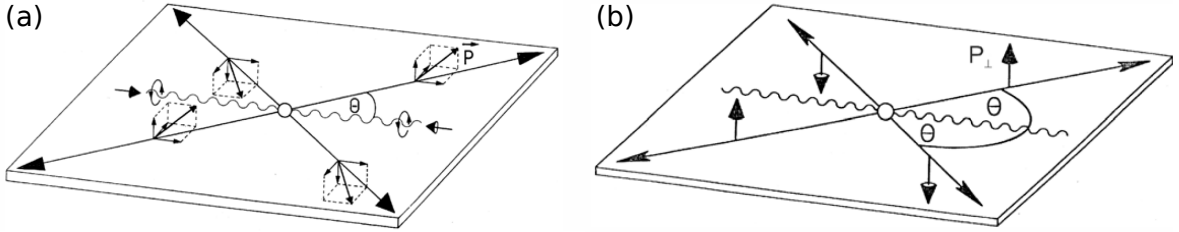


Figure 3.7: Photoionization reaction plane using (a) circularly polarized light with three components of the spin polarization vector, and (b) unpolarized light with a spin polarization of photoelectrons perpendicular to the plane. Images are taken from Ref. [151].

In order to investigate the influence of light polarization on the measured spin-polarization in spin-resolved ARPES measurements, Heinzmann et al. [151] introduced a “reaction plane”. For linearly polarized light, this plane is defined by the electric field vector \vec{E} and the photoelectron momentum [152]. Thus it depends on the polarization angle of the light. In the case of circularly polarized light, it is defined by the momenta of photons and photoelectrons. If the helicity of the radiation is reversed, the two spin-components in the reaction plane switch their sign, since these are proportional to the degree of circular polarization [153]. The third spin-component, which is perpendicular to the reaction plane, remains unchanged, as depicted in Fig. 3.7 (a). As unpolarized and linearly polarized light can be described by an incoherent or coherent superposition of left- and right-handed circularly polarized light, respectively, this third component should not be influenced by light polarization (see Fig. 3.7 (b)).

This was confirmed by measurements on Bi_2Te_3 with C^+ , C^- and p-polarized light [154]. Note that the reaction plane is the same for these polarization directions. The spin components S_x or S_y tangential to the Rashba-split band, which are perpendicular to the reaction plane depending on the measurement direction, are the same for all three polarization directions. The S_z component parallel to the reaction plane switched its sign dependent on the polarization, due to the dipole selection rules. Sánchez-Barriga et al. [155] saw in their

measurements on Bi₂Se₃ with photon energies between 50 eV and 70 eV as well that the S_x or S_y components perpendicular to the reaction plane displays the initial spin state of the system, regardless of whether C^+ , C^- or p -polarized light was used.

However, spin-resolved ARPES measurements are not always easy to interpret. In systems with a small Rashba-type spin-splitting, like the $(\sqrt{3} \times \sqrt{3})$ reconstruction of Sb/Ag(111), an intrinsic overlap between states with opposite spinors can be present. This causes an apparent large spin polarization component normal to the quantization axis of the Rashba effect seen in SARPES, independent on photon energy or its polarization [156]. It is possible to distinguish between the Rashba-type spin polarization and the components due to the overlap because the former typically crosses zero at the peak centers of the spin-integrated momentum distribution curve (MDC) [157]. The spin polarization of the overlap produces components with their maxima at the point of maximum overlap, which is at the center of the MDC peak [156].

3.3.3 Spin-resolved measurements along a mirror axis

For crystalline surfaces used in spin-resolved ARPES measurements, the question arises whether spin-components can be detected along a mirror axis and how the spin-polarization of photoelectrons change in case of different light polarizations. To make it even more complicated, the angle of incidence also plays a crucial role.

In systems with two mirror axis perpendicular to each other, i.e., in symmetry group C_{nv} ($n = 2, 4, 6$), and assuming normal incidence of light and normal emission of the photoelectrons, no spin-polarization is allowed regardless of the light polarization [148]. This can be explained by considering a single xz -symmetry plane, with z along the surface normal. The mirror operation in spin space,

$$M = -i\sigma_y, \quad (3.3.3)$$

prescribes for the spin-components in x and z direction $S_x = S_z = 0$, only allowing $S_y \neq 0$ [146]. Thus a second yz -mirror plane leads to $S_y = S_z = 0$, resulting in a vanishing spin-polarization for $k_{\parallel} = 0$ [148].

However, in case of an arbitrary incidence angle Φ in the xz -plane, the yz -mirror symmetry only remains for s -polarized light, since in this case \vec{E} is parallel to the surface. For both p and circular polarization, \vec{E} breaks the symmetry of the yz -plane due to the angle Φ . Thus, a finite S_y spin-component is possible [149].

If only one symmetry axis parallel to the measurement direction is present, e.g., along the xz -plane with symmetry group C_{3v} , the ejected photoelectrons are expected to show the following spin-components [146, 149]:

$$S_x = S_z = 0 \quad \text{and} \quad S_y \neq 0 \quad (3.3.4)$$

This result is based on the fact, that for circularly polarized light the mirror operation reverses the helicity, and thus spin components in the surface plane are generally allowed. As for linearly s - and p -polarized light only a finite P_y component is allowed, the same is true for circularly polarized light, which is a coherent superposition of s - and p - polarized parts.

So far, only circular, s -, and p -polarized light were considered. Additionally, Yaji et al. [158] showed a strong dependence of the measured spin-polarization on the angle of linear

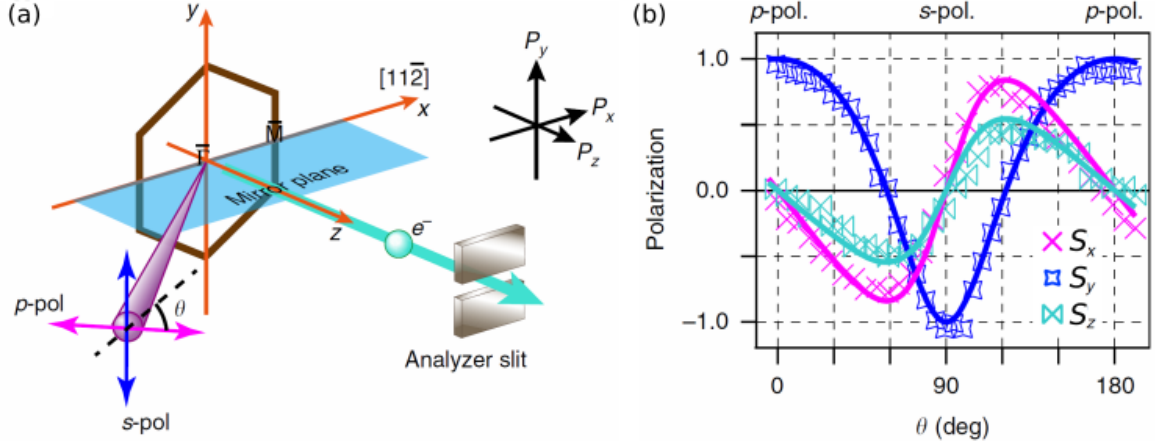


Figure 3.8: (a) Schematic drawing of the experimental geometry and a surface Brillouin zone with a mirror plane along $\Gamma\bar{M}$. The definition of the spin polarization direction is indicated. It can be rotated continuously by angle θ , which is the angle between \vec{E} of the linearly polarized light and the mirror plane. (b) Total intensity of simulated (solid lines) and experimental (dots) three-dimensional spin-polarizations of photoelectrons. Both figures taken from [158].

polarization. Their measurement setup is drawn schematically in Fig. 3.8(a). Along a mirror axis, only p - and s -polarized light shows the values expected according to Eq. 3.3.4. However, if the linearly polarized light has a polarization angle θ other than 0° or 90° , all three spin-components have finite values. Furthermore, a switch of sign in S_y between p - and s -polarization based on parity is seen in their measurements (see Fig. 3.8(b)). This switch is explained by dipole selection rules: s -polarized light excites states that are anti-symmetric to the mirror plane (ϕ_{odd}), p -polarized light excites the symmetric ones (ϕ_{even}). Spin-polarized bands may be made up of linear combinations of even and odd orbitals. Yaji et al. treated systems like Bi(111), Bi₂Se₃ and W(110), for which they concluded the spin-polarized branches consist of either $\phi_{even,\uparrow} + \phi_{odd,\downarrow}$ or $\phi_{even,\downarrow} + \phi_{odd,\uparrow}$, thus a spin-flip can be expected. In other systems, e.g., Au(111), this spin-flip between measurements with s - and p -polarized light is not observed [159]. This indicates their bands consist of the other two possible linear combinations, $\phi_{even,\uparrow} + \phi_{odd,\uparrow}$ and $\phi_{even,\downarrow} + \phi_{odd,\downarrow}$.

In the course of this thesis, SARPES measurements were performed on α -Sn/Si(111) along a direction which is a mirror plane for the structural ($\sqrt{3} \times \sqrt{3}$) surface reconstruction, using C^+ polarized light (cf. chapter 6.3). Therefore, the reaction plane coincides with the structural mirror plane; hence, only a finite S_y component is allowed. Since in addition both S_x and S_z components are detected by SARPES, the predicted spin-ordering causing an electronic ($2\sqrt{3} \times \sqrt{3}$) unit cell with three rotational domains was confirmed. For interpretation of the spin data, it is worth emphasizing again that the light polarization may alter the sign of spin components in the reaction plane but not their direction and amplitude.

Up to now, the discussion was restricted to the measured spin components. Apart from that, in case of circularly polarized light, the helicity of the beam influences the total intensity obtained in spin-integrated ARPES measurements owing to the so-called circular dichroism. Since the photons are initially spin-polarized due to optical orientation, they have a higher

scattering probability with electron carrying the same spin, resulting in a higher photocurrent measured at the detector. Consequently, intensity asymmetries observed between spectra using C^+ and C^- polarized light point towards spin-polarized surface states, although the quantitative analysis requires the knowledge of the specific electronic states involved [160–162].

Experimental setup

In the scope of this thesis, material systems are investigated that are not stable in air. Hence all measurements were carried out in an ultra-clean environment under ultra-high vacuum (UHV) conditions. This minimizes the adsorption of defects and increases the quality of in-situ prepared samples. The base pressure within the UHV chambers usually is approximately 10^{-10} mbar. The silicon samples used for the measurements were all first degassed at 500°C overnight and (unless otherwise stated) subsequently flashed to 1200°C prior to their initial preparation.

In total four different UHV chambers were used to perform STM, SPALEED, SARPES and transport experiments, which will be explained in the following sections.

4.1 Scanning tunneling microscope

In the course of this theses, two different kinds of scanning tunneling microscopes (STM) were used. For the investigations of Sn on both flat and vicinal Si substrates, as well as In nanowires, a variable temperature STM (VT-STM) was utilized. STS and high resolution STM data of Pb nanowires on Si(557) was acquired with a low temperature STM (LT-STM).

4.1.1 Variable temperature STM

The variable temperature STM is built in a *UHV 700* vacuum chamber, both are produced by RHK Technologies, Inc. [163]. A schematic setup of the STM is presented in Fig. 4.1 (a). It consists of a stage on which the samples are placed and a retractable scan head attached above it. On top of the sample holder is a helical ramp, which is divided into three segments. When the scan head is placed on the sample holder, each of its three piezo tube legs rests on one of these segments, due to the “Walker” type design of the STM. The tip is inserted in the center of the scan head, where it is movable via piezo elements in x , y , and z direction. Electrochemically etching is used for manufacturing the tips from tungsten wire. This technique is commonly used in order to produce atomically sharp tips. Further details on the procedure can be found elsewhere, e.g., [164, 165].

Samples can be heated resistively by passing a current through them, controlled by an infrared pyrometer, or cooled down to 25 K. Depending on the required temperature, either

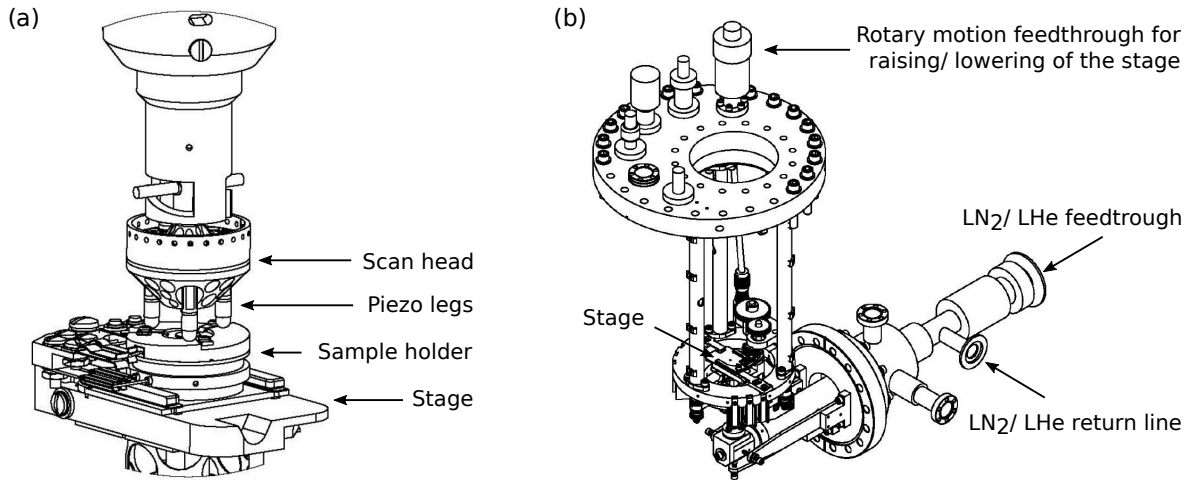


Figure 4.1: (a) Schematic setup of the VT-STM showing how the scan head is placed on the sample holder. (b) Setup of the STM stage and the cryostat located below it. Both pictures are adapted from [163].

liquid Helium (LHe) or liquid Nitrogen (LN₂) is suitable for cooling. By varying the flow rate, different temperatures can be set. The cryostat is located directly below the sample stage, as depicted in Fig. 4.1 (b). In this case, only the sample is cooled, while the tip and the rest of the system remain at ambient temperature. This allows the sample temperature to be changed quickly, but the quality of the sample may be influenced detrimentally due to rest gas atoms condensing on it.

The sharpness of STM tips can be improved in-situ by a tip heating system, that accelerates electrons from a hot filament towards the tip by applying high voltages. A garage is installed for storing up to six holders at the same time, carrying either tips or samples. Furthermore, a mass spectrometer is available for characterization of the residual gas composition.

A preparation chamber is attached to the STM-chamber for preparing samples without interrupting the UHV conditions. It is equipped with three metal evaporators (indium, lead, and tin) to prepare thin metallic films on silicon substrates. Here as well, the samples can be heated resistively for the degassing procedure of new samples, or during the preparation. To check the overall sample quality, an optical LEED is available. Additionally, this chamber is equipped with a XPS system and a sputter gun.

Samples and tips are exchanged by using a load lock system that is installed on the preparation chamber. By this means UHV conditions inside stay intact.

4.1.2 Low temperature STM

For low temperature measurements, a Scienta Omicron LT-STM was used [166]. In contrast to the previously described VT-STM, in this setup not only the sample is cooled but the entire STM system. This is done by the use of two concentric bath cryostats (see Fig. 4.2 (a)). The outer one serves as shielding and is usually filled with LN₂. The inner one is cooled either by LN₂ or LHe, resulting in a temperature of $T \approx 80$ K or $T \approx 6$ K, respectively.

Within these cryostats, the scanner and the sample stage are located. The scanner holding

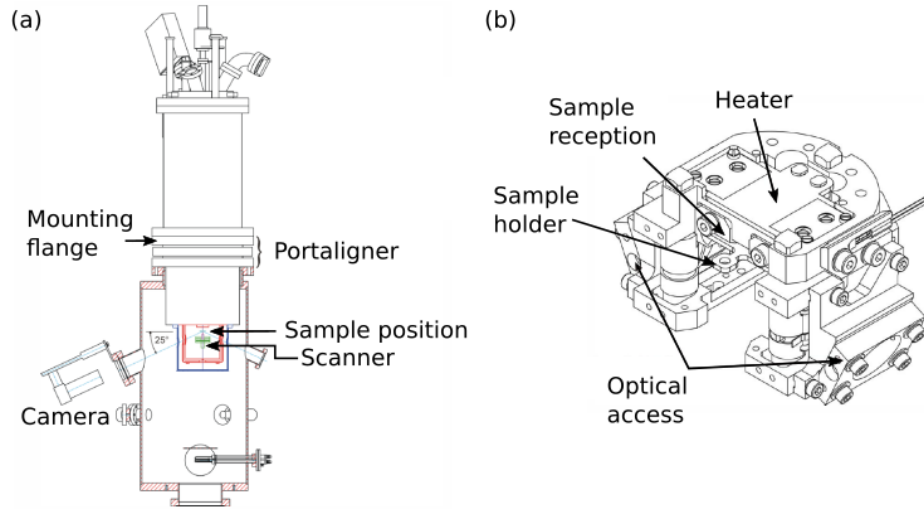


Figure 4.2: (a) Schematic front view of the LT-STM. Scanner and sample are surrounded by two concentric bath cryostats. (b) Setup of the sample stage. Both images are adapted from [166].

the tip is below the stage; thus, the sample is inserted upside down (see Fig. 4.2 (b)). For the measurements shown in chapter 8, both electrochemically etched tungsten tips and tips cut from Platinum-Iridium wire were used. Furthermore, the stage is equipped with a heating element for variation of the sample temperature. As the cryostats and thermal shielding surround the STM, optical access is only given by the use of a camera during scanning.

Inside the STM chamber, in total twelve sample holders or tip carriers can be stored in two carousels. A preparation chamber is installed on the STM chamber, which is equipped with an optical LEED and two evaporators (Pb and MnPc). During preparation, samples can be heated either resistively or by the use of a filament in the vicinity of the sample. The temperature is controlled with the same infrared pyrometer that was used on the VT-STM chamber. Samples and tips are exchanged via a load lock system attached to the preparation chamber.

In the course of the STS measurements presented in this thesis, dI/dV spectroscopy was done using an SR830 Lock-In amplifier [167]. This yields a better signal to noise ratio than a numerical calculation from the $I(V)$ curve.

4.2 COPHEE endstation at SIS beamline

Spin-resolved and spin-integrated ARPES measurements were done at the COmplete PHotoEmission Experiment (COPHEE) endstation at the Surface and Interface Spectroscopy (SIS) beamline of the Swiss Light Source, at the Paul Scherrer Institute. Circularly (C^+ and C^-) and linearly (s and p) polarized light with an energy range of 20 eV to 800 eV is provided by an undulator installed at SIS.

In Fig. 4.3, a schematic view of the endstation is shown [168]. Samples are installed via a load lock system on a manipulator with three translational and three angular degrees of

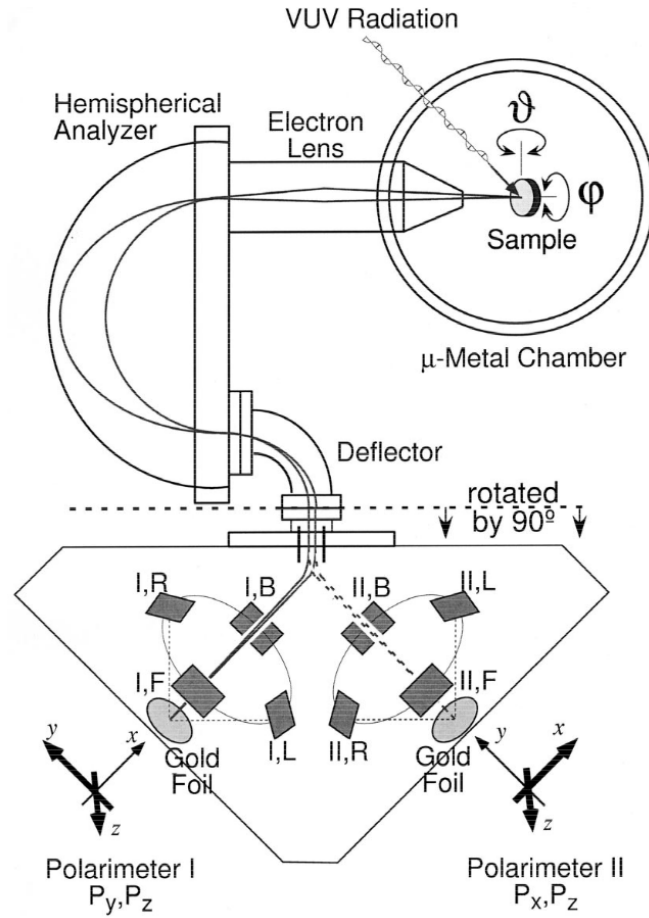


Figure 4.3: Schematic setup of the COPHEE endstation; taken from Ref. [168]. Electrons are photoemitted from a sample by UV radiation from SIS beamline. They can be angle-selected by rotation of the sample and energy-selected by the use of the electrostatic hemispherical analyzer. Two orthogonal Mott detectors measure the spin-polarization of the photoelectrons.

freedom. This allows exact positioning in real space and gives access to the reciprocal space dependent on the rotation angle. For spin-integrated ARPES a hemispherical analyzer is used with energy and angular resolution of 25 meV and 0.3° respectively. In order to measure the spin-components, COPHEE takes advantage of the spin selectivity of Mott scattering [169]. In order to acquire all three spin-components S_x , S_y and S_z , two Mott detectors are installed. In the spin-resolved mode, a resolution of 80 meV and 0.75° can be reached.

During measurements and sample preparation, the manipulator can be cooled down to 20 K with LHe, and the samples can be heated by resistive heating, monitored with the same infrared pyrometer as used at the VT-STM chamber. An optical LEED is built as well in the COPHEE endstation to check the sample quality. Further details on the setup can be found elsewhere, e.g., [168, 170, 171].

4.2.1 Calculation of the spin polarization

In this section, the calculation of the spin polarization components is briefly explained according to [168]. It is used for the interpretation of the SARPES data of the α -Sn phase on Si(111) discussed chapter 6.

In the so-called *Mott detector* installed in the COPHEE endstation, the photoemitted electrons are accelerated to a gold foil. In principle, the spin polarization P_x perpendicular to the scattering plane is calculated from the measured asymmetry A_x in the backscattered intensities N_L and N_R to the left or right of the incoming beam,

$$P_x = \frac{A_x}{S} = \frac{1}{S} \frac{N_L - N_R}{N_L + N_R}, \quad (4.2.1)$$

taking into account the Sherman function $S = 0.08$ [172], which is the asymmetry measured in the case of a 100 % polarized beam.

In accordance with the labels of the eight detectors shown in Fig. 4.3, the spin polarization components of the full polarization vector \vec{P} are given by

$$P_x = \frac{1}{S} \frac{N_{\text{II, B}} - N_{\text{II, F}}}{N_{\text{II, B}} + N_{\text{II, F}}}, \quad (4.2.2)$$

$$P_y = \frac{1}{S} \frac{N_{\text{I, F}} - N_{\text{I, B}}}{N_{\text{I, F}} + N_{\text{I, B}}}, \quad (4.2.3)$$

$$P_z = \frac{1}{2S} \left(\frac{N_{\text{I, L}} - N_{\text{I, R}}}{N_{\text{I, L}} + N_{\text{I, R}}} + \frac{N_{\text{II, L}} - N_{\text{II, R}}}{N_{\text{II, L}} + N_{\text{II, R}}} \right). \quad (4.2.4)$$

Considering the rotation of the sample manipulator with the angles ϑ and φ , the polarization vector P^{S} , which is the vector of expectation values of the three spin component operators S_x , S_y and S_z , in the sample coordinate system is

$$\begin{pmatrix} P_x^{\text{S}} \\ P_y^{\text{S}} \\ P_z^{\text{S}} \end{pmatrix} = \frac{1}{\sqrt{2}} \begin{pmatrix} \cos \vartheta \cos \varphi - \sin \varphi & -\cos \vartheta \cos \varphi - \sin \varphi & \sqrt{2} \sin \vartheta \cos \varphi \\ \cos \vartheta \sin \varphi + \cos \varphi & -\cos \vartheta \sin \varphi + \cos \varphi & \sqrt{2} \sin \vartheta \sin \varphi \\ -\sin \vartheta & \sin \vartheta & \sqrt{2} \cos \vartheta \end{pmatrix} \times \begin{pmatrix} P_x \\ P_y \\ P_z \end{pmatrix} \quad (4.2.5)$$

4.3 4pp STM/SEM

In order to perform local electronic transport measurements on In nanowires, a so-called four-point probe scanning tunneling microscope/scanning electron microscope (4pp STM/SEM) from Omicron Nanotechnology is utilized. It consists of four independently controllable STM scanners, as depicted in Fig. 4.4 (a). One high-resolution scanner is capable of acquiring atomically resolved STM images due to enhanced protection against vibration. The other three standard scanners are only used for the execution of transport measurements. All four scanners are equipped with electrochemically etched tungsten tips. The sample stage can be cooled down to 25 K using LHe. For fast stabilization of temperature, it is counter heated by a filament controlled utilizing a proportional-integral-derivative (PID) controller. As the tips are not directly cooled, they only adapt to the sample temperature while being in tunneling or ohmic contact with it.

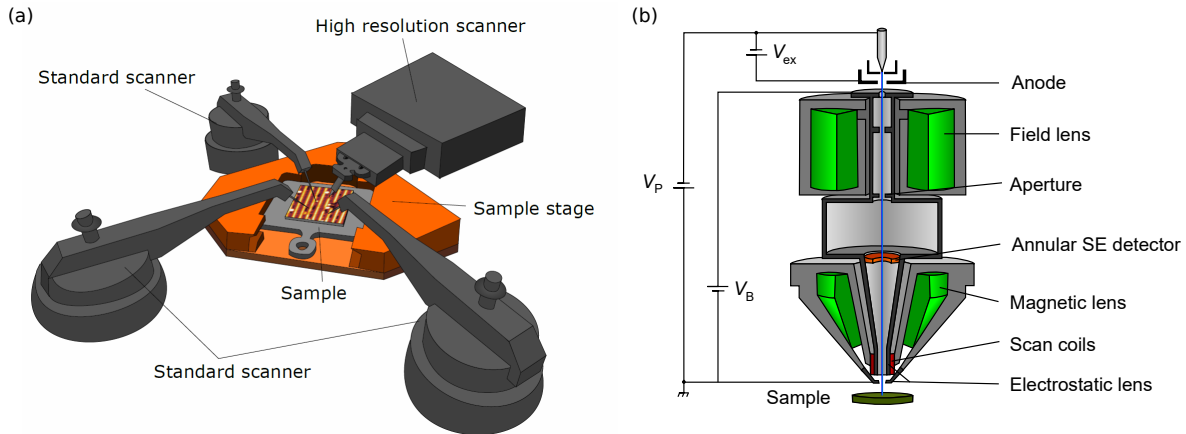


Figure 4.4: (a) Schematic of the 4pp-STM setup used for transport measurements; taken from Ref. [124]. (b) Cross-sectional view of the SEM column; taken from Ref. [173, 174].

Above the STM scanners, a GEMINI-type SEM is attached, which is commercially available from Carl Zeiss AG. Electrons extracted from a hot field emission cathode are accelerated and focused on the sample surface. SEM images with a resolution of approximately 4 nm can be obtained. A cross-sectional view of the SEM column labeled in more detail can be found in Fig. 4.4 (b). It is indispensable for the exact positioning of the four STM tips on a sample surface with nanoscale structures, e.g., nanowires. The standard contacting procedure as well as the way of cleaning the tips prior to the measurements by applying voltage pulses is extensively described elsewhere, e.g., [124], and will not be explained further here.

The 4pp-STM/SEM is installed in the analysis chamber of the UHV setup sketched in Fig. 4.5. A preparation chamber is attached to it, hosting an In evaporator and a SPALEED needed to monitor the quality of the samples. During preparation, heating via direct current or a backside filament is possible; both controlled with an infrared pyrometer (LumaSense IG 140). Additionally, a cooling stage is available for temperatures down to 140 K by use of LN_2 . Both the analysis and preparation part host a garage for storage, and a load lock system for changing samples or tips without compromising the UHV conditions.

The chamber is equipped with several further devices, such as a mass spectrometer or a hydrogen cracker. Furthermore, there are two ways to tune STM tips in-situ. A tip heating tool is located in the preparation part, while a field ion microscope (FIM) is attached to the analysis part. The latter provides access to the tip's chemical composition or the size of its apex [175], which additionally can be tuned to form single atom tips employing field evaporation [176].

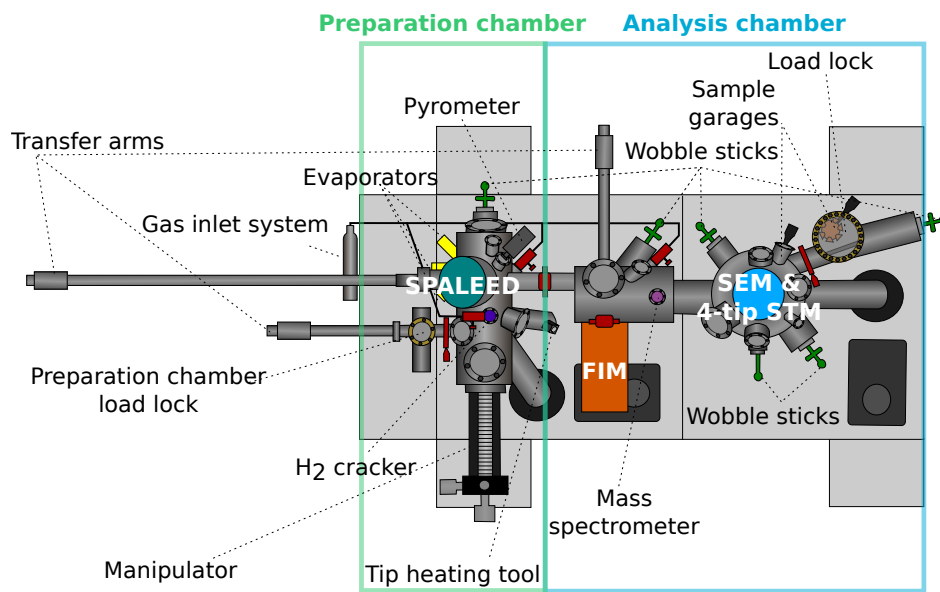


Figure 4.5: Schematic drawing of the 4pp STM/SEM chamber. It consists of two parts, namely the preparation chamber and the analysis chamber, marked with green or blue rectangles, respectively. Adopted from [124].

Part II

Self-Assembled Low-Dimensional Systems on Silicon Substrates

In/Si(111)-(4 × 1) reconstruction

The (4 × 1)-In/Si(111) reconstruction is one of the most intensively studied model systems in the context of quasi-1D atomic nanowires. As described in detail in chapter 2.2, it reversely undergoes a Peierls-type metal-insulator transition at a temperature of about $T_c \approx 120$ K. Furthermore, the system shows a thermal hysteresis with a width of $W_H \approx 8 - 10$ K in conductivity measurements [88] and LEED studies [84, 96] during subsequent cooling and heating cycles. The hysteresis width decreases if substrate steps are present on the surface, e.g., on samples with a miscut of 2° from [111] towards the $[\bar{1}\bar{1}2]$ direction [88]. This is due to a shift of the onset of the phase transition temperature upon heating, T_2 , to lower values, caused by a lack of interchain coupling in the vicinity of a step edge. In this chapter, further transport investigations were done regarding the confinement effects induced by surface steps on the phase transition temperature using silicon substrates with a miscut of 1° and 4° towards the $[\bar{1}\bar{1}2]$ direction.

For all measurements described in the following, the (4 × 1) In reconstruction is prepared on a clean Si(111)-(7 × 7) substrate. During evaporation of 0.6 – 1.2 ML In, the sample is held at a temperature of 400 °C. According to the phase diagram of In/Si(111) [177, 178] choosing either higher annealing temperatures or another coverage results in different phases, e.g. (1 × 1) or $(\sqrt{31} \times \sqrt{31})R9^\circ$. These phases were used for calibration of the evaporator.

5.1 Influence of spatial confinement on the Peierls transition

In order to gain further insights concerning the influence of spatial confinement induced by substrate steps on the phase transition temperature, In nanowires grown on two differently inclined Si substrates, i.e., with 1° and 4° miscut along the $[\bar{1}\bar{1}2]$ direction, were studied in detail. First, they were characterized by means of SPALEED and anisotropy measurements (chapter 5.1.1), and after that temperature-dependent transport experiments were carried out (chapter 5.1.2).

For transport data acquired on Si substrates, the space charge layer introduced in chapter 3.1.3 can have a significant influence on the measured sheet conductivity. Since it is well-known that its thickness depends on the temperature used during cleaning of the bare Si substrate, two distinct temperatures were chosen for flash annealing prior to the evaporation of In. Hence, in total four types of samples are considered in the following: two of each miscut

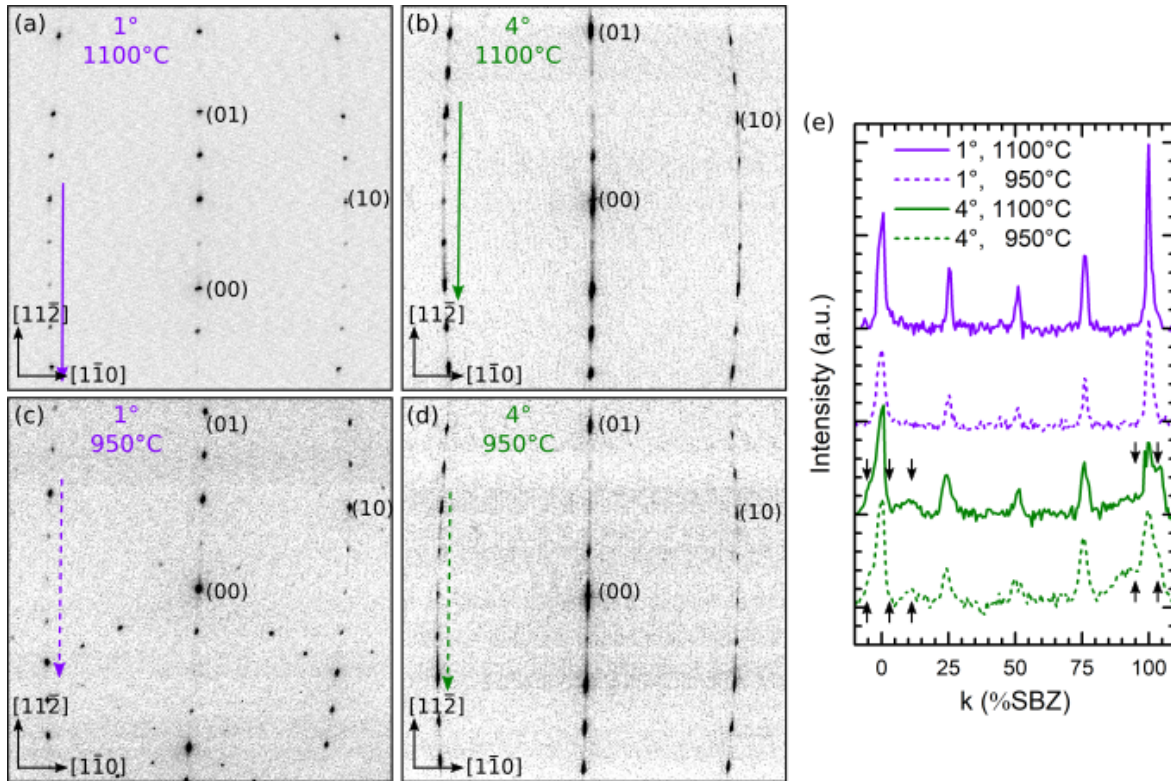


Figure 5.1: SPALEED pattern of the (4×1) -In/Si(111) reconstruction at RT all taken at $E = 96$ eV. Substrates are (a), (c) with 1° miscut towards the $[\bar{1}\bar{1}2]$ direction, and (b), (d) with 4° miscut towards the $[\bar{1}\bar{1}2]$ direction. The maximum temperature during flash annealing prior to the nanowire growth was (a), (b) 1100°C and (c), (d) 950°C . Diffraction spots of (1×1) -Si are indicated. (e) Linescans along the directions shown by the arrows in (a)-(d). Black arrows highlight peaks with a spacing of 7.5% SBZ originating from the steps of the 4° miscut samples.

angle, either heated up to a maximum temperature of 950°C or a higher one of 1100°C .

5.1.1 Characterization of the samples

The four types of In/Si(111) samples were first characterized by means of SPALEED. The corresponding patterns are shown in Figs. 5.1(a)-(d). On all of these substrates grows primarily a single-domain (4×1) -In reconstruction. For the samples with 1° miscut, the average terrace width of 18 nm is suitable for twelve rows of the (4×1) reconstruction. However, due to the flash annealing cycles along with mechanical stress by the clamping of the sample to its holder, the substrate steps may shift resulting in terraces exceeding the width of 30 nm, where all three domains are able to grow [97] (see Fig. 5.1 (c)).

For the 4° case, three (4×1) rows fit on the terraces, which are on average 4.5 nm wide. The higher density of steps and the resulting lack of interaction between adjacent nanowires causes the diffraction spots to be elongated in the direction perpendicular to the wires, compared to the 1° samples. It is visible in the linescans taken along the first order diffraction spots shown in Fig. 5.1 (e). Moreover, in the vicinity of the (1×1) Si diffraction spots, small peaks

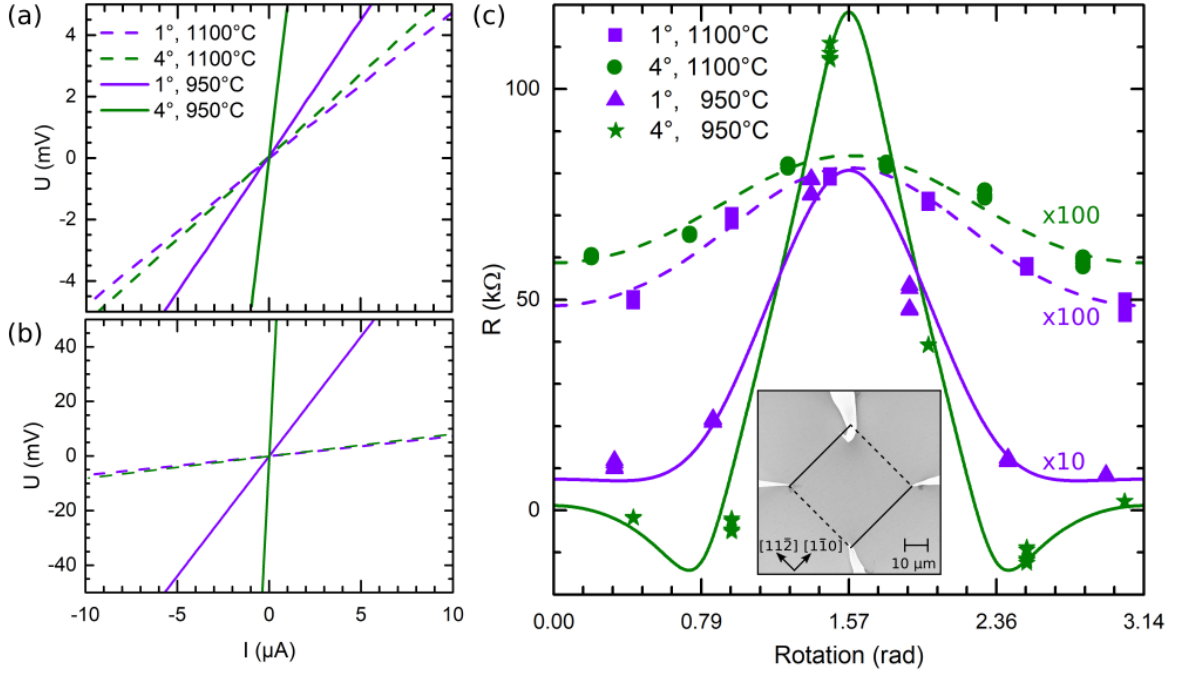


Figure 5.2: Exemplary $I(V)$ curves measured at RT in the direction (a) parallel and (b) perpendicular to the In nanowires. (c) Resistance measured at RT using the rotational square method and curves fitted according to Eq. 3.1.12 on samples with 1° (violet) and 4° (green) miscut. The Si substrates were flash annealed at temperatures up to 950°C (solid lines) or 1100°C (dashed lines). The latter are magnified by a factor 100, the solid purple curve by 10. Zero refers to the $[1\bar{1}0]$ direction parallel to the In wires. Inset: SEM image of the four STM arranged in a square geometry used for transport measurements.

with a spacing of 7.5% SBZ are present on the 4° miscut samples. They correspond to the average terrace width of 4.5 nm .

Since the SPALEED images were taken at an electron energy of 96 eV , which is an in-phase condition, i.e., the scattering phase is an integer value ($S = 5$), the spot profile is governed by the instrumental broadening and any further information concerning the samples' quality caused by the different annealing temperatures cannot be deduced [133].

Further information about the samples is obtained via transport measurements, which were measured using a 4pp square geometry, as introduced in chapter 3.1.3. The positioning of the STM tips was monitored by SEM, which is exemplarily depicted in the inset of Fig. 5.2(c). Resistance values were deduced from linear $I(V)$ curves. Some of these curves acquired in the direction parallel and perpendicular to the In nanowires on the four types of samples are displayed in Figs. 5.2(a) and (b), respectively. They clearly show an increase in resistance for the samples flashed to 950°C compared to the 1100°C ones, which implies a better ordered and less defective surface reconstruction in the latter case.

As a next step, the samples were characterized by means of rotational square measurements, and the anisotropy ratios ρ_y/ρ_x were calculated using Equation 3.1.12 (see Fig. 5.2(c)). The samples flashed to 1100°C with a miscut of 1° and 4° have a low anisotropy ratio of 1.4 and 1.3, respectively. For the samples heated to 950°C , the anisotropy of the 1° sample is already

much larger, i.e., $\rho_y/\rho_x = 5.4$. However, an increase of more than one order of magnitude to an anisotropy value of 47 is found for the 4° sample heated to 950°C , even exhibiting negative resistance for certain rotation angles. This demonstrates the enhanced SCL growth at elevated temperatures since nominally both substrate types have the same resistivity of $\rho = 0.4 - 2.6 \Omega\text{cm}$. Apparently, considering the samples heated to 1100°C , the SCL is thick enough to enable almost 2D-like conduction, even in the presence of a high density of steps. In contrast to that, for the samples heated to 950°C , the 1D conductance is much more pronounced, indicating a thin SCL, and additionally, an influence of the number of surface steps on the anisotropy ratio is clearly visible. These findings will be verified in the following by considering the individual components contributing to the sample conductivities.

5.1.2 Temperature-dependent transport investigations

Temperature-dependent resistance measurements were performed on the four types of samples. The 4pp square arrangement was aligned in such a way, that either the resistance parallel, R_{\parallel} , or perpendicular to the nanowires, R_{\perp} , is obtained. For each of the samples, two sets of data are shown in Fig. 5.3, which were acquired either during the cooling of the sample or its subsequent heating. This procedure is similar to the cooling and heating cycle carried out in previous measurements [84, 88, 96]. The resulting resistance curves all show the same behavior: Coming from high temperatures, the resistances first vary only slightly, but then show a sharp increase for temperatures below ~ 150 K. Notably, both samples heated to 1100°C (Figs. 5.3(a) and (c)) show similar values of R_{\parallel} and R_{\perp} , regardless of the number of steps existing on the surfaces. However, the total increase of resistance is only about a factor of 4, while the scattering of the data points is quite large. Additionally, R_{\perp} and R_{\parallel} differ very little even at low temperatures, and no difference is visible between the heating and cooling curve, confirming a rather 2D-like conductivity behavior.

In contrast to that, for the samples heated to 950°C , the resistance increases by several orders of magnitude. Concerning the sample with 1° miscut, the anisotropy gets larger for lower temperatures. While R_{\perp} shows similar values for the cooling and heating curve, the resistance measured in the direction along the nanowires differs. Upon cooling below ~ 150 K, the rise of R_{\parallel} is significantly lower than for the corresponding heating curve. Only the very last data point measured during cooling deviates from this, which exhibits a much higher resistance compared to the other values. This can be attributed to a probe, that is not sufficiently brought into contact with the sample; thus, this data point is disregarded in the further analysis and only plotted for the sake of completeness.

Regarding the 4° sample flashed to 950°C , transport measurements were rather challenging to execute. Upon cooling to temperatures below 200 K, R_{\perp} already rose up to the $\text{M}\Omega$ range, caused by the low interaction between wires on adjacent terraces. Thus, as the probes continued to lose contact quite frequently, further data was acquired using only two probes instead of four. Since for the 2pp setup not only the sample resistance is measured, but additionally, the resistances of the contacts and the probes are included, there is a sudden jump in resistance visible at ~ 200 K in Fig. 5.3(d). Furthermore, the sharp increase in resistance below ~ 150 K is less pronounced than in the 1° miscut case.

In the following sections, the conductivity of the In induced surfaces state is evaluated based on these temperature dependent resistance measurements. First, the samples heated

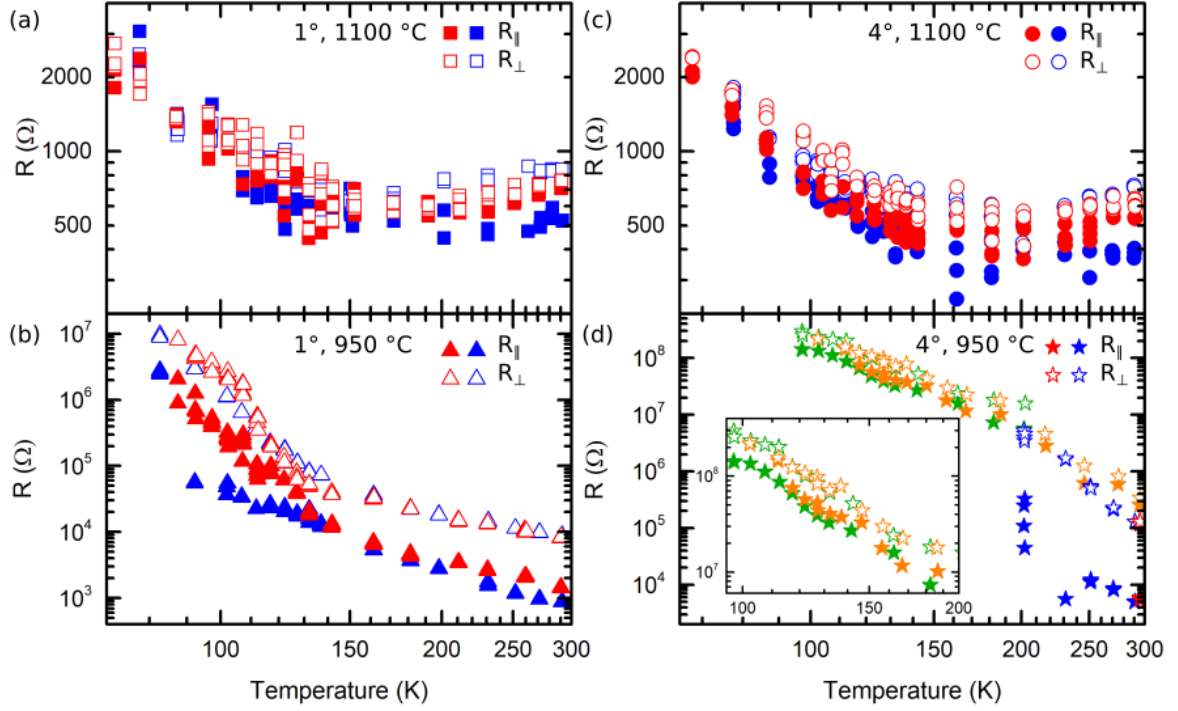


Figure 5.3: Temperature dependent resistance measurements performed in a 4pp square arrangement measured parallel ($R_{||}$) and perpendicular (R_{\perp}) to the nanowires during cooling (blue) and heating (red). The samples had a miscut of (a), (b) 1° and (c), (d) 4° towards $[\bar{1}\bar{1}2]$. Prior to indium evaporation, the Si substrates were flash annealed up to either (a), (c) 1100°C or (b), (d) 950°C . Owing to the high resistance values in (d), 4pp measurements were only possible for the data marked in blue and red, whereas all other data was acquired as 2pp measurements (green and orange). Inset in (d) shows an enlargement of the data below 200 K.

to 1100°C are discussed, and afterward the samples, which were flash annealed up to 950°C during the cleaning procedure.

Surface state conductivity of the samples flash annealed at 1100°C

In order to evaluate the surface state conductivity σ_S induced by the In reconstruction, first of all the conductivities parallel and perpendicular to the In nanowires, $\sigma_{||}$ and σ_{\perp} , are calculated using Equation 3.1.10 and $\sigma = 1/\rho$. For the samples with the substrates annealed at 1100°C , the results are displayed in Fig. 5.4. In panel (a) and (b), the conductivities of the sample with 1° miscut are plotted for the cooling and heating curve, respectively. The same is shown in panel (d) and (e) for the 4° sample. Since the (4×1) -In reconstruction has quasi-1D metallic surface state bands [98], σ_{\perp} is attributed completely to the sum of conductivity contributions originating from bulk and SCL,

$$\sigma_{\perp} = \sigma_B + \sigma_{\text{SCL}} = \sigma_B + \sigma_{\text{pSCL}} + \sigma_{\text{iSCL}}. \quad (5.1.1)$$

Further details on these individual conductivity contributions and their dependence on the parameters used for fitting can be found in chapter 3.1.3.

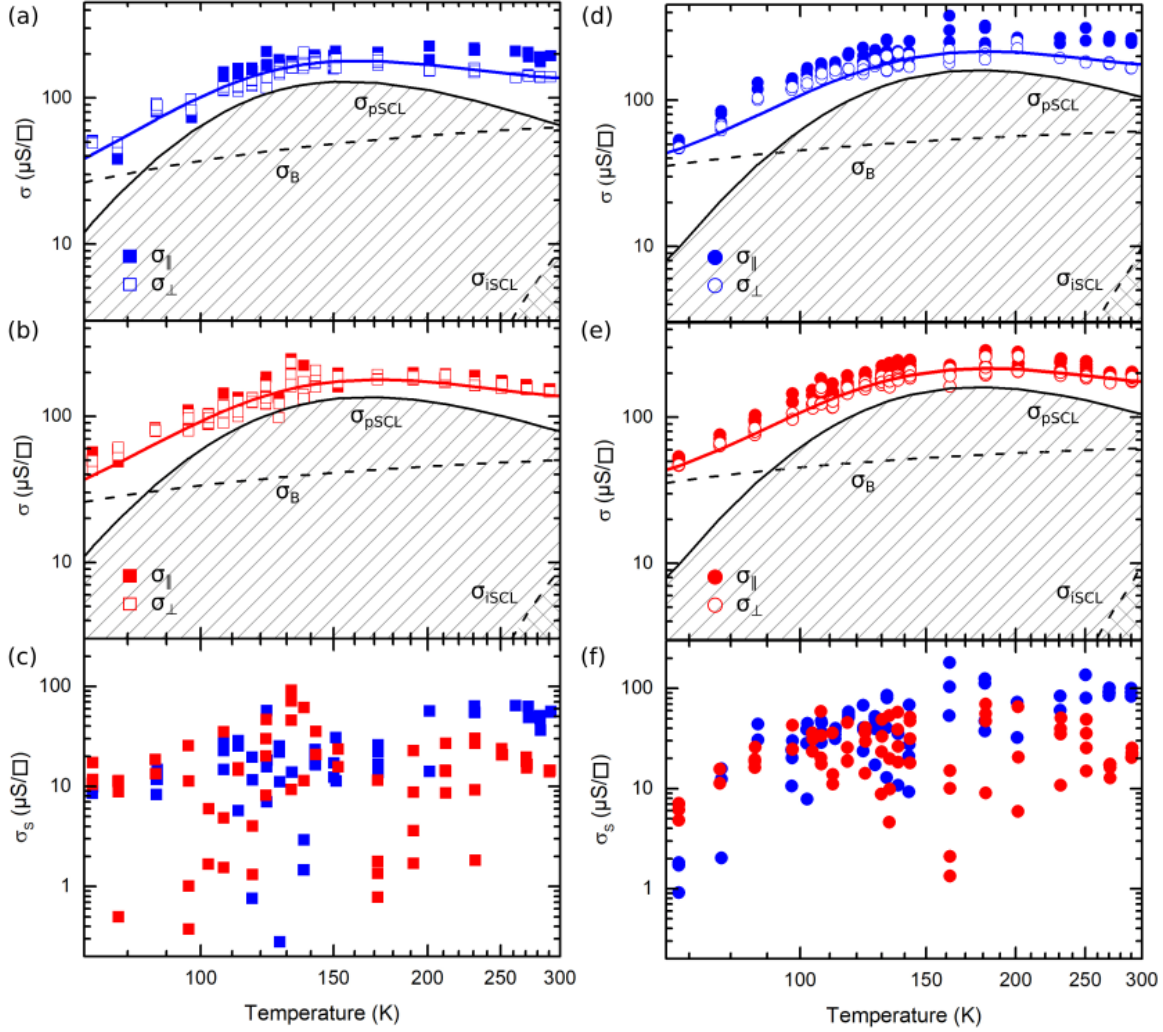


Figure 5.4: Temperature dependent conductivities of samples with (a)-(c) 1° and (d)-(f) 4° miscut angle, which have been flash annealed up to 1100°C . (a) and (d) was acquired during cooling, whereas (b) and (e) are the heating curves. The contributions of the bulk and the SCL, σ_B , σ_{pSCL} , and σ_{iSCL} are indicated. Their sum is depicted as blue or red lines, corresponding to the direction of temperature change. (c) and (f) show the conductivity of the surface state, σ_s , during cooling and heating.

The fitting procedure was done as follows: First, the intrinsic SCL conductivity, σ_{iSCL} , was determined, since it simply depends on the donor concentration of the bulk, which is $N_{\text{D}} \approx 3.2 \cdot 10^{15} \text{ cm}^{-3}$ according to the substrate resistivity of $\rho = 0.4 - 2.6 \text{ } \Omega\text{cm}$. After that, the contributions originating from the bulk and the parasitic sub-surface p-type SCL were iteratively calculated using Mathematica [179], in order to receive the best possible fit to the measured data of σ_{\perp} .

For both samples, i.e., with the 1° and the 4° miscut substrate, the same fitting parameters were obtained. Employing Eq. 3.1.14, the activation energy of σ_{B} yields $\Delta_{\text{B}} \approx (6 \pm 2) \text{ meV}$, which is in accordance with recent results from similar measurements on Au/Si(553) [124]. The parasitic p-type SCL is calculated to have a thickness of approximately $t_{\text{SCL}} \approx 200 \text{ nm}$ with a acceptor concentration in the range of $N_{\text{A}} \approx 1 \cdot 10^{17} \text{ cm}^{-3}$, according to Eq. 3.1.24. These values exactly reproduce the results reported for the p-type sub-surface dopant inversion layer of n-type Si(111) flash annealed at 1150°C [77] and are in the same order of magnitude as earlier results for In/Si(111) [26]. The corresponding temperature dependent curves for σ_{B} , σ_{pSCL} , and σ_{iSCL} , as well as the sum of all three conductivity components for each of the samples are plotted in Fig. 5.4. It is clearly visible that the calculated total conductivity is in good agreement with the measured data of σ_{\perp} .

Finally, the conductivity of the surface state σ_{S} is calculated via

$$\sigma_{\text{S}} = \sigma_{\parallel} - \sigma_{\perp}. \quad (5.1.2)$$

The resulting σ_{S} curves are plotted in Figs. 5.4 (e) and (f), respectively. However, for both 1° and 4° samples, neither cooling nor heating data exhibit a clear trend that hints towards the phase transition temperature of the In nanowires. Instead, the data points scatter around a mean value of approximately $\sigma_{\text{S}} \approx 10 \text{ } \mu\text{S}/\square$, which is rather due to noise than to the actual surface state conductivity. Therefore, the metal-insulator transition temperature of the In nanowires is not identifiable, and this data cannot confirm any influence of the increased step density in the case of the 4° miscut substrate.

Surface state conductivity of the samples flash annealed at 950°C

The same kind of analysis as described in the previous section has been performed on the two samples, that were flash annealed only up to 950°C . The results are plotted in Fig. 5.5. Starting with the 1° miscut sample, the activation energy increases by about an order of magnitude, i.e., $\Delta_{\text{B}} \approx (50 \pm 5) \text{ meV}$, while both the SCL thickness and the acceptor concentration within the parasitic SCL decrease significantly compared to the samples heated to 1100°C , being $t_{\text{SCL}} \approx 40 \text{ nm}$ and $N_{\text{A}} \approx 2 \cdot 10^{16} \text{ cm}^{-3}$, respectively. Moreover, due to the low total conductivity measured perpendicular to the nanowires, the intrinsic SCL makes up a larger share compared to the 1100°C samples (see Figs. 5.5 (a) and (b)). This is consistent with literature stating the thickness of the p-type SCL increases for higher flash annealing temperatures, e.g., reaching the μm range for 1300°C [26, 77], while for low annealing temperatures the intrinsic SCL is the predominant conductivity contribution [26].

In this case, the conductivity of the quasi-1D surface state σ_{S} can indeed be determined, as obvious from Fig. 5.5 (c). As expected for the In nanowires, the drop of σ_{S} at low temperatures is induced by the metal-insulator transition. The critical temperatures are estimated to be $T_1 \approx 128^{\circ}\text{C}$ for the cooling curve and $T_2 \approx 138^{\circ}\text{C}$ during heating. The

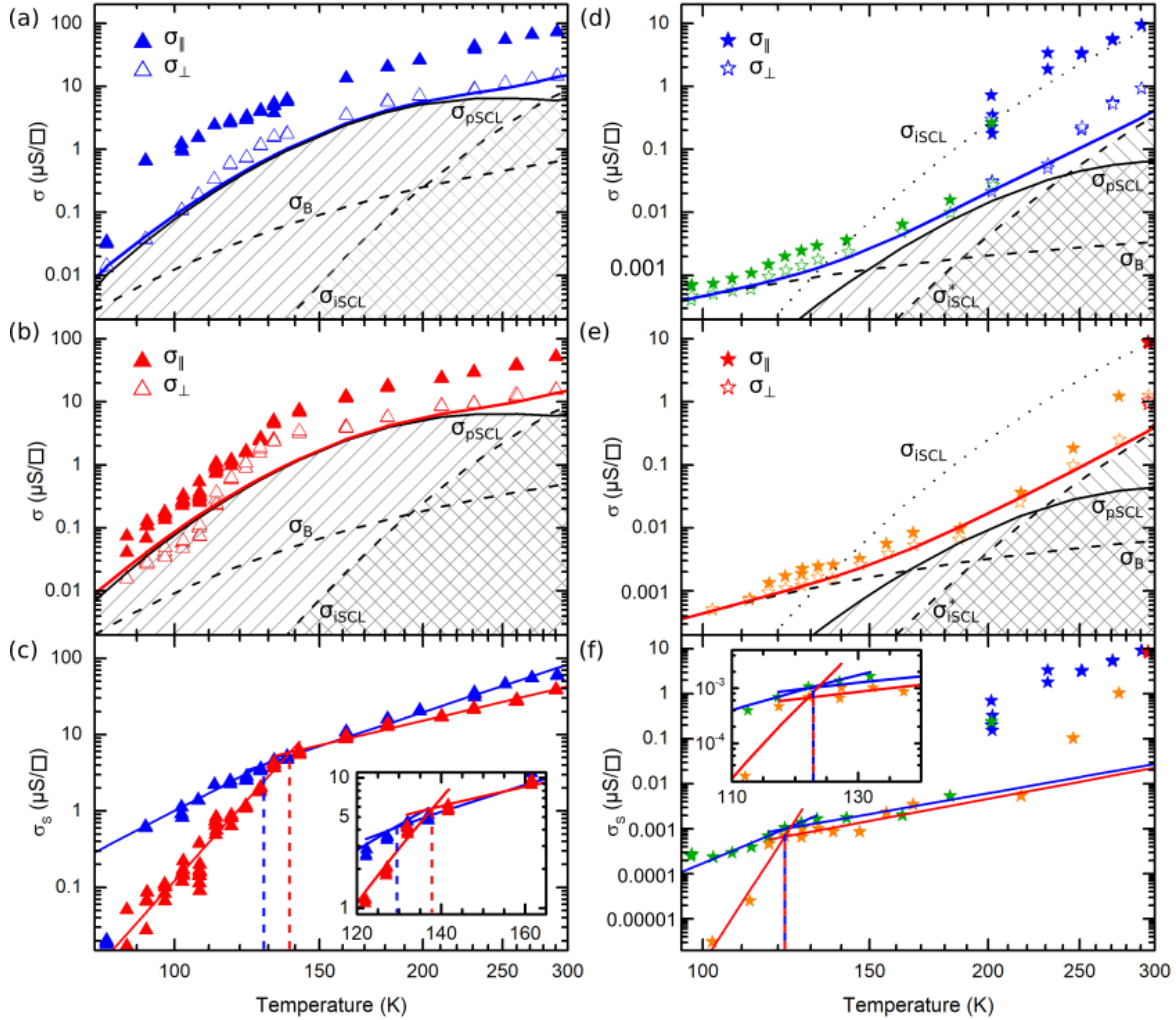


Figure 5.5: Temperature dependent conductivities of samples with (a)-(c) 1° and (d)-(f) 4° miscut angle, which have been flash annealed up to 950 °C. (a) and (d) was acquired during cooling, whereas (b) and (e) are the heating curves. The contributions of the bulk and the SCL, σ_B , σ_{pSCL} , σ_{iSCL} , as well as in (d) and (e) a modified σ_{iSCL}^* , are indicated. Their sum is depicted as blue or red lines, corresponding to the direction of temperature change. (c) and (f) show the conductivity of the surface state, σ_s , during cooling and heating. The insets show an enlargement of the area around T_c . Solid and dotted lines are guides to the eye highlighting the change in conductivity, dashed lines indicate the deduced T_1 (blue) and T_2 (red). In (d)-(f) green and orange colored data points were acquired in a 2pp setup, while the other were measured in 4pp geometry.

resulting hysteresis width $W_H \approx 10$ K is of comparable size to previous studies [84, 88, 96], while the actual transition temperatures are shifted to higher values by about 9 K [88]. As this is true for both the cooling and heating curve, a systematic variation due to too fast temperature changing rates can be excluded. Consequently, it has to be attributed to a constant temperature difference between the sample and temperature sensor. Subtracting it leads to final values of $T_1 \approx 119^\circ\text{C}$ and $T_2 \approx 129^\circ\text{C}$.

For the 4° sample heated to 950°C , the fitting procedure had to be adjusted. As previously mentioned, this data was acquired using both a 4pp and 2pp setup. For the latter, the probe and contact resistances contribute to the measured resistances. Hence, in order to include the contact resistance, the 2pp conductivities shown in Figs. 5.5 (d) and (e) were corrected by adding a temperature dependent conductivity contribution. It corresponds to the thermionic emission induced by the current flow from the probe to the sample

$$\sigma_T \propto T^2 \exp\left(-\frac{\phi_B}{k_B T}\right) \quad (5.1.3)$$

with the Schottky barrier height of the probe material tungsten on Si being $\phi_B \approx 0.7$ eV [180]. However, as obvious from the dotted line indicating σ_{iSCL} , already this contribution considerably overestimates the measured data. Therefore, additionally, a modified σ_{iSCL}^* with a reduced sheet conductivity was applied.

The parameters used for fitting of σ_\perp turned out to be $\Delta_B \approx (30 \pm 3)$ meV, $N_A \approx 1 \cdot 10^{16} \text{ cm}^{-3}$, and $t_{\text{SCL}} \approx 2$ nm, while the modified intrinsic SCL remains the predominant contribution. Compared to the 1° case, the bulk activation energy and the dopant concentration of the SCL is in a similar range, however its thickness is reduced by an order of magnitude. This is consistent with the difference of about one order of magnitude between these two samples, taking into account that a decrease of t_{SCL} leads to lower conduction values (cf. chapter 3.1.3, Fig. 3.4).

The remaining question, whether the step density influences the phase transition temperature, is answered by Fig. 5.5 (f). Similar to the 1° sample, a drop of surface state conductance σ_S is observable at low temperatures, but the onset of the phase transition is shifted in temperature. The critical temperatures are estimated to be $T_1 = T_2 \approx 122$ K both during cooling and heating. As mentioned above, a systematic temperature offset of 9 K due to the experimental setup has to be subtracted, resulting in $T_1 = T_2 \approx 113$ K. Consequently, the apparent phase transition temperatures are lowered by approximately $\Delta T_1 \approx 6$ K and $\Delta T_2 \approx 16$ K compared to the 1° sample.

Hence, from measurements performed on In nanowires on top of substrates that were flash annealed only to 950°C , the surface state conductivity originating from the quasi-1D In reconstruction can be deduced. Besides, for the case of high step densities, the vanishing of the hysteresis for heating and cooling cycled was confirmed. However, this is not solely caused by a shift of T_2 , as proposed earlier [88]. Instead, a shift of about 6 K to lower temperatures was observed for T_1 as well.

5.2 Summary and conclusion

In summary, this chapter reported on the influence of substrate steps on the phase transition temperature of In nanowires grown on Si(111) substrates. Steps present on even nominally

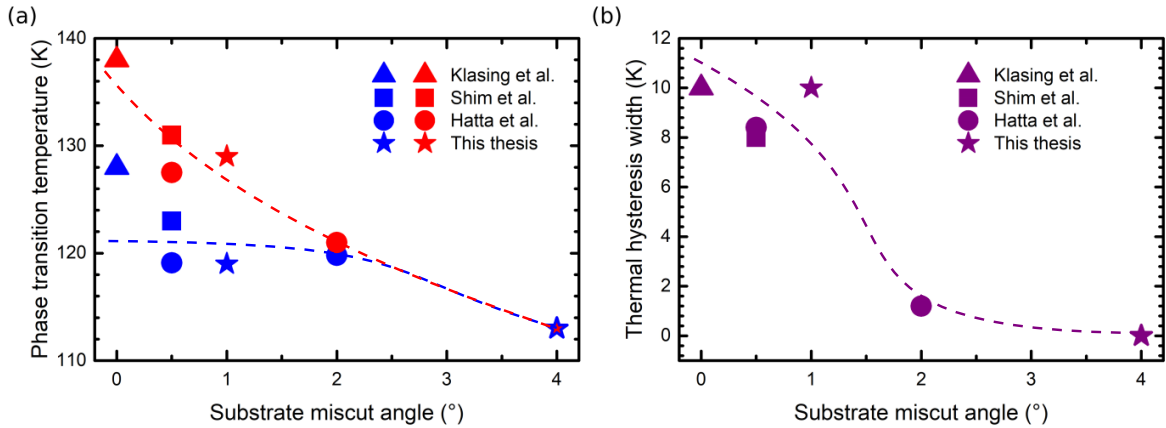


Figure 5.6: Comparison of experimentally obtained (a) phase transition temperatures of In/Si(111) during cooling T_1 (blue) and during heating T_2 (red) and (b) the thermal hysteresis width $W_H = T_2 - T_1$. Data was taken from Klasing et al. [84], Shim et al. [96] and Hatta et al. [88]. Dashed lines are a guide to the eyes.

flat surfaces were formerly expected to impede the interchain coupling between neighboring (4×1) chains, leading to a destabilization of the low temperature (8×2) phase. Since this shifts the apparent phase transition temperature T_2 upon heating to lower temperatures, while the critical temperature during cooling, T_1 , remains constant, a reduction of the hysteresis width of the sheet conductivity was observed for subsequent heating and cooling cycles.

A detailed analysis done by probing the surface state conductivity via transport measurements demonstrated a more complex behavior. In addition to the expected vanishing of the thermal hysteresis on samples due to surface steps, a shift of both T_1 and T_2 to lower temperatures was observed. This is highlighted in Fig. 5.6, where the apparent phase transition temperatures measured in the scope of this thesis as well as the deduced thermal hysteresis widths are compared with literature data obtained on samples with different substrate miscut angles.

This leads to the conclusion that the surface steps do not only destabilize the low-temperature phase upon heating but additionally can affect the formation of the (8×2) during cooling. Since the transition in the latter direction preferentially starts inside a (4×1) domain [88], the steps influence the phase transition temperature only for a sufficiently high density of steps. For small terrace widths suitable for merely three (4×1) nanowires, the nucleation of the (8×2) is forced to start close to a step edge resulting in a decrease of T_1 due to the lack of interchain coupling.

α -Sn phase on Si(111)

The following chapter goes into detail about the structural and electronic properties of α -Sn/Si(111) with a coverage of $\theta = 1/3$ ML. Much attention is paid to its Mott-insulating low-temperature phase that exists below $T \approx 70$ K. Compared to Pb, the electronic correlation effects for α -Sn are much stronger due to the smaller orbital size. On the other hand, due to the smaller Z of Sn, the role of spin-orbit coupling just recently came into the focus of research. Consequently, the low-temperature phase of α -Sn was investigated in order to elucidate the effect of SOC in a correlated electronic system and measured the spin-components of the surface states in the Mott regime directly by means of spin- and angle-resolved photoemission (SARPES).

For the measurements, long-range ordered Si(111) surfaces (phosphorous-doped, $0.01 \Omega\text{cm}$) as templates for Sn adsorption were prepared by degassing the samples at 500°C for several hours and repeated flash annealing to 1150°C until a sharp (7×7) reconstruction was seen by LEED. Afterward, $1/3$ of a monolayer of Sn was evaporated on the surface while the sample was held at 600°C . The quality of the α -Sn surface reconstruction with $(\sqrt{3} \times \sqrt{3})$ symmetry was checked afterwards by LEED. The diffraction pattern remains unchanged upon cooling down to 40 K with LHe. The rate of evaporation was calibrated independently by STM experiments. VT-STM measurements were performed in collaboration with Uygur Özdemir during his bachelor thesis [181]. The spin-integrated and spin-resolved ARPES data of the low-temperature phase were previously published in " α -Sn phase on Si(111): Spin texture of a two-dimensional Mott state" [182] and will not be cited separately.

6.1 Phase diagram of Sn submonolayer structures on Si(111)

Adsorption of submonolayers of Sn on Si(111) substrates gives rise to several phases that have been investigated for more than 50 years. They were first studied by Estrup and Morrison [184] in 1964, who observed four different stable phases at room temperature using LEED. Detailed reflection high energy electron diffraction (RHEED) measurements later confirmed their findings and added information about the temperature dependence of those phases [183].

The resulting phase diagram depending on substrate temperature and Sn coverage is displayed in Fig. 6.1. Starting at a coverage of $\theta = 1/6$ ML, the (7×7) reconstruction of the Si(111) substrate vanishes and a mosaic $\text{Si}_x\text{Sn}_{1-x}/\text{Si}(111)-(\sqrt{3} \times \sqrt{3})R30^\circ$ structure develops

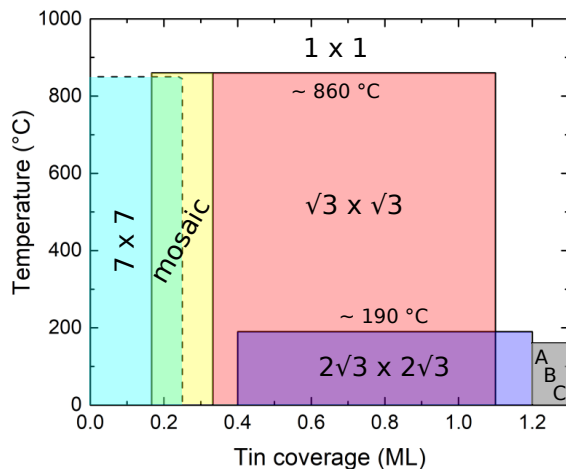


Figure 6.1: Phase diagram of tin submonolayer structures on Si(111) depending on substrate temperature and coverage, adapted from [183]. *A*, *B*, and *C* denote high coverage phases with $(\sqrt{133} \times 4\sqrt{3})$, $(3\sqrt{7} \times 3\sqrt{7})R(30 \pm 10.9)^\circ$ and $(2\sqrt{91} \times 2\sqrt{91})R(30 \pm 3)^\circ$ reconstructions.

with $0.5 \geq x \geq 0$, that is named γ -Sn phase. It consists of a mixture of Sn and Si atoms in T_4 positions at the surface [185]. At an exact coverage of $\theta = 1/3$ ML all Si atoms in the topmost layer at the surface are substituted by Sn atoms. This phase is called α -Sn phase, which forms a $(\sqrt{3} \times \sqrt{3})$ structure as well [185, 186]. Increasing the coverage even more, a $(2\sqrt{3} \times 2\sqrt{3})R30^\circ$ phase starts to develop on top of the α -Sn structure. Both phases coexist in separate domains up to a coverage of more than one monolayer, at which only the $(2\sqrt{3} \times 2\sqrt{3})$ phase is present [62, 187–189]. In contrast to the low coverage phases that consist of a single atomic layer, the $(2\sqrt{3} \times 2\sqrt{3})$ phase comprises two layers of Sn atoms. However, its atomic structure is currently still under debate. Latest results [190] favor a model by Toernevik et al. [187] containing 14 Sn atoms per unit cell arranged in a double layer, with its top layer comprising of four atoms. Furthermore, three high coverage phases are reported that are labeled *A*, *B* and *C* in the phase diagram. They form structures with large unit cells, namely $(\sqrt{133} \times 4\sqrt{3})$, $(3\sqrt{7} \times 3\sqrt{7})R(30 \pm 10.9)^\circ$ and $(2\sqrt{91} \times 2\sqrt{91})R(30 \pm 3)^\circ$ [183].

If the substrate temperature is changed to higher values than room temperature, both $(2\sqrt{3} \times 2\sqrt{3})$ and $(\sqrt{3} \times \sqrt{3})$ phases undergo a transition to a (1×1) structure, at temperatures of $T_{2\sqrt{3}} \approx 190^\circ\text{C}$ and $T_{\sqrt{3}} \approx 860^\circ\text{C}$, respectively [183].

6.2 Structural properties of α -Sn

As mentioned before, the α -Sn phase exists at a coverage of $\theta = 1/3$ ML Sn on the flat Si(111) surface. It forms a $(\sqrt{3} \times \sqrt{3})R30^\circ$ reconstruction with a lattice constant of $a_{\text{Sn}} = \sqrt{3}a_{\text{Si}} = 6.65 \text{ \AA}$. In Fig. 6.2(a), a top view with marked unit cells is sketched. The Sn atoms are located at T_4 positions at the threefold hollow site above the second layer silicon atoms [191].

After preparation, all samples were checked with LEED. As seen in Fig. 6.2(b), (1×1) diffraction spots originating from the silicon substrate are clearly observable as well as $(\sqrt{3} \times \sqrt{3})$ spots caused by the Sn superstructure. By this means, the consistently good sample

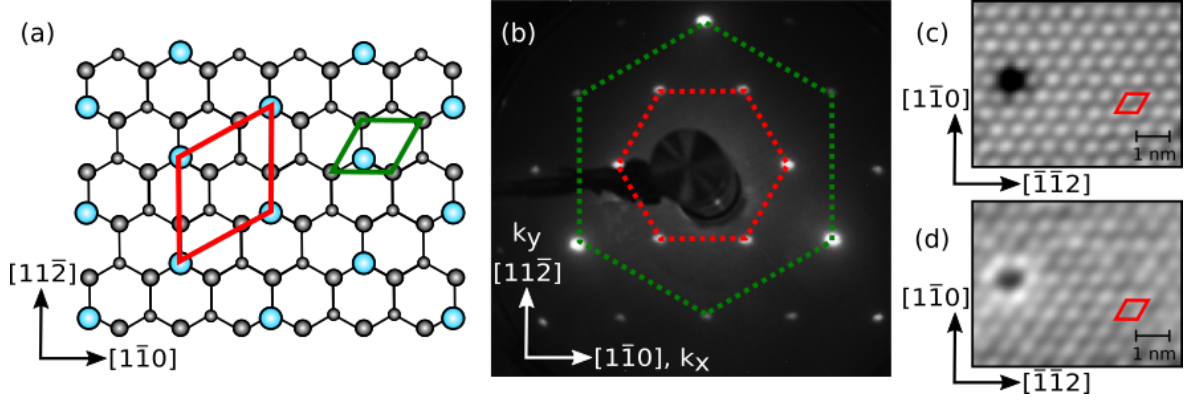


Figure 6.2: (a) Schematic top view of the α -Sn reconstruction on Si(111). Blue circles represent Sn atoms on T_4 adsorption sites; Si atoms are gray, their size indicates if they belong to the first or second layer of the substrate. Unit cells of $(\sqrt{3} \times \sqrt{3})$ -Sn (red) and (1×1) -Si (green) are marked with lines. (b) LEED images taken at an electron energy of 77.4 eV at room temperature. Dashed lines connect the first order diffraction spots of $(\sqrt{3} \times \sqrt{3})$ (red) and (1×1) (green) diffraction spots. (c) and (d) Empty and filled state STM image of the α -Sn phase exhibiting a defect caused by a substitutional silicon atom; the $(\sqrt{3} \times \sqrt{3})$ unit cell is highlighted in red ($U = 1\text{ V}$ and -1 V , respectively, $I = 100\text{ pA}$).

quality is ensured.

Looking at the α -Sn phase with a STM, the $(\sqrt{3} \times \sqrt{3})$ structure can be resolved (cf. Figs. 6.2 (c) and (d)). Bright protrusions indicate the positions of Sn atoms, and the underlying Si substrate is obviously not resolvable. The Sn atoms all have the same apparent height except for those lying close to a certain type of defect. In order to acquire a long-range ordering of the surface, the amount of defects has to be reduced as low as possible. During the measurements presented here, the average defect density determined by the evaluation of several STM pictures did not exceed 3%. Similar values have been reported before by other groups [192, 193]. By choosing a higher temperature for the annealing step (e.g., 825 °C), the defect density can reach a value up to 50% due to desorption, creating the mosaic γ -Sn phase [185].

Since the first STM investigations on this surface in 1994 [185], in total five different kinds of defects have been identified [193–199]. Two of them are due to substitutional atoms (Si or dopant atoms from the substrate), two originate from Sn atoms incorporated in the first or second substrate layer, and the last one can be attributed to a vacancy [197]. The defect shown in Figs. 6.2 (c) and (d) is characterized by a hole surrounded by a hexagonal ring of either darker protrusions in an empty state picture or brighter ones for the filled states. This is typical for a substitutional silicon atom located at a T_4 site, which is the most frequently observed defect on this surface. If two or more of those are located next to each other, a local (3×3) pattern is formed [195, 197], which must not be confused with a low temperature (3×3) phase as it is only local and observable at room temperature [192, 199]. This kind of defect has also been reported for other systems, e.g. Pb/Ge(111) [200] or Sn/Ge(111) [201–203].

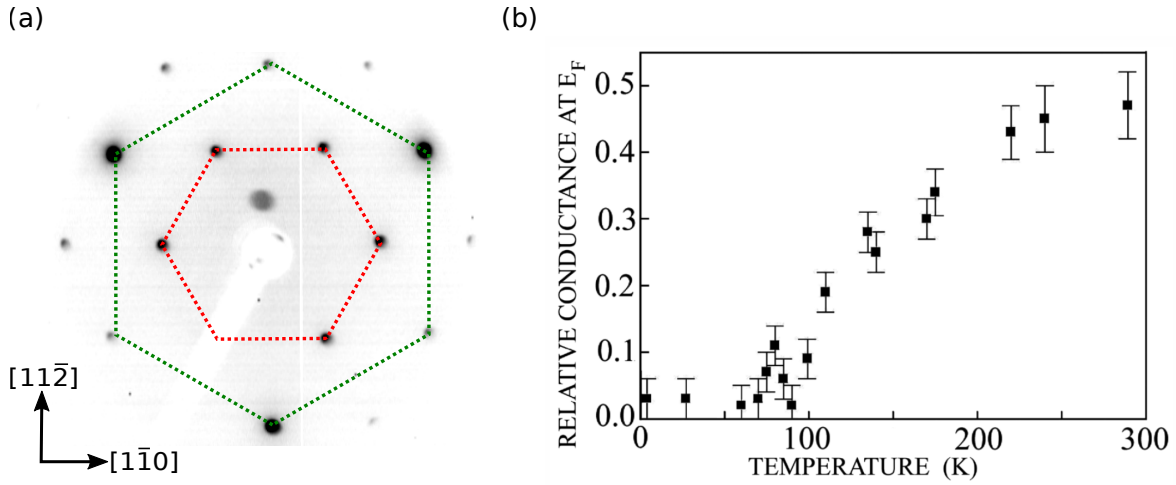


Figure 6.3: (a) LEED image of α -Sn taken at an electron energy of 76 eV at a temperature of 40 K. Dashed lines connect the first order diffraction spots of (1×1) (green) and $(\sqrt{3} \times \sqrt{3})$ (red). The feature next to the electron gun stems from a defect on the screen. (b) Temperature dependence of the LDOS at the Fermi level. The values have been normalized at the maximum value of the conductance 0.3 eV above and below E_F ; taken from Ref. [66].

6.3 Low temperature phase of α -Sn

At temperatures below room temperature many group IV element $(\sqrt{3} \times \sqrt{3})$ reconstructions on semiconductors with a coverage of $1/3$ ML, i.e., similar to α -Sn, exhibit a low temperature phase. Systems like Sn/Ge(111) [201], Pb/Si(111) [204] or Pb/Ge(111) [29] undergo a reversible phase transition from $(\sqrt{3} \times \sqrt{3})$ to (3×3) during cooling. Hence such a transition was expected for the α -Sn phase as well [194]. However, as obvious from the LEED picture taken at 40 K displayed in Fig. 6.3 (a), the $(\sqrt{3} \times \sqrt{3})$ pattern is still remaining without any hint of additional diffraction spots originating from a possible low temperature phase. In 2002, it was confirmed by STM that the $(\sqrt{3} \times \sqrt{3})$ reconstruction is present at temperatures as low as 6 K [192], thus this system indeed does not undergo a structural transition to a (3×3) phase.

Later it turned out that despite these findings, an isostructural phase transition exists. Below 70 K, the α -Sn phase changes from a metal to an insulator [66]. The band gap size is experimentally observed to be around 200 meV in ARPES [21] whereas calculations yield 328 meV [205]. STS and conductivity measurements indicate that this metal-insulator transition MIT is driven by strong electron correlations as known for a Mott-Hubbard insulator [206]. In Figure 6.3 (b), the corresponding decrease in conductance at low temperatures is displayed. Theoretical results show that the insulating ground state of α -Sn might be a ferrimagnetic Slater-type insulator via itinerant magnetic order [205, 207] or, on account of spin-orbit coupling, a 120° -Néel structure with non-collinear ordering [208]. However, based on high resolution photoemission experiments and DFT [21], a description of the spin-integrated spectral function is only possible if row-wise collinear antiferromagnetic order with a $(2\sqrt{3} \times \sqrt{3})$ symmetry at low temperatures is assumed for the Mott state. ARPES measurements of the surface state responsible for the MIT are shown in Fig. 6.4 (a). The

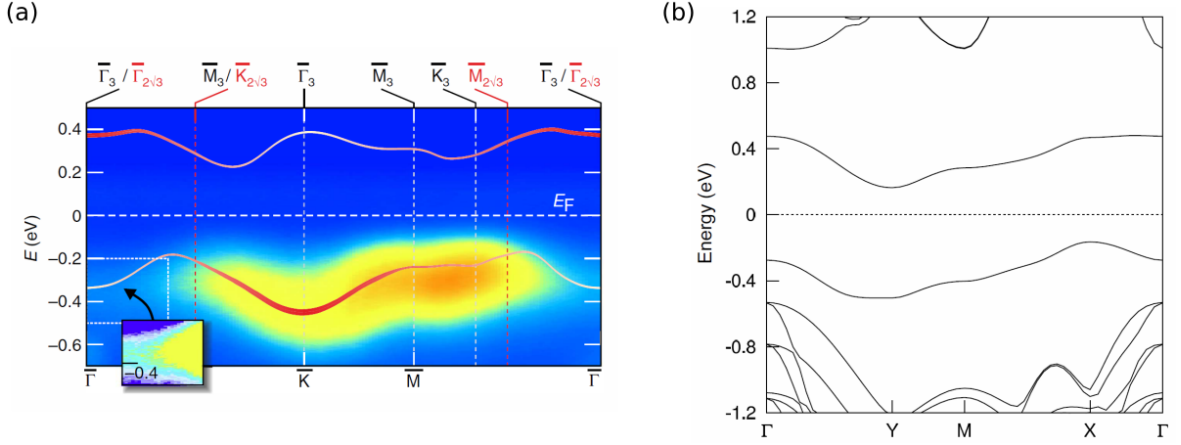


Figure 6.4: (a) Comparison of the (LDA + DCA) quasi-particle dispersion (red curve) with the ARPES intensity (false colour plot, $T \approx 60$ K) in the original ($\sqrt{3} \times \sqrt{3}$) SBZ (lower labels) and the (3×3) and $(2\sqrt{3} \times 2\sqrt{3})$ SBZs (upper labels). Inset: replica of the ARPES shadow band within dashed box, displayed with enhanced contrast, which highlights the non-degeneracy between $\bar{\Gamma}$ and \bar{K} ; taken from Ref. [21]. (b) Surface band structure of the antiferromagnetic $(2\sqrt{3} \times \sqrt{3})$ reconstruction obtained using the HSE functional; taken from Ref. [205]. High symmetry points are denoted in Fig. 6.5(c). The energy zero represents the Fermi level.

superimposed quasi-particle dispersion was calculated by combining a dynamical cluster approximation (DCA) with DFT, namely the local density approximation (LDA), yielding a Hubbard $U = 0.60$ eV and the electronic hopping parameter $t = 52.7$ meV. Thus, the system is strongly correlated, and hopping is suppressed by the strong on-site coulomb repulsion (cf. chapter 2.1.1). Additionally, it clearly rules out a (3×3) spin texture on the surface because of the absent band back-folding from $\bar{\Gamma}$ to \bar{K} [21].

The proposed $(2\sqrt{3} \times \sqrt{3})$ unit cell occurs if Sn atoms of the structural $(\sqrt{3} \times \sqrt{3})$ reconstruction are associated with a spin. In this case, the spin is ordered in a row-wise collinear antiferromagnetic way if every other row of Sn atoms carries the same spin. Thus the resulting spin unit cell is twice as large as the structural $(\sqrt{3} \times \sqrt{3})$ unit cell. A top view of it is sketched in Fig. 6.5(a) with the unit cell marked in an oblique and rectangular fashion. This unit cell generally exists in three domains rotated by 120° with respect to each other, see Figs. 6.5(b) and (c). In reciprocal space, this gives rise to rectangular SBZs, as shown in Fig. 6.5(d). Unlike Li et al. [21] suggested, the mere existence of these three rotational domains does not lead to an effective $(2\sqrt{3} \times 2\sqrt{3})$ SBZ but to a more complex pattern as discussed in the following sections.

Indeed, the same symmetry was obtained by hybrid DFT calculations, but suggesting a Slater-type insulator via band magnetism [205]. The screened hybrid exchange-correlation functional of Heyd-Scuseria-Ernzerhof (HSE) was used for correction of the self-interaction error inherent to conventional DFT and eventually stabilizing this spin pattern. The resulting band structure of the $(2\sqrt{3} \times \sqrt{3})$ rectangular SBZ as shown in Fig. 6.4(b) features a spin-degenerate insulating surface state that is well within the ARPES measurements. The broad appearance of the surface state in ARPES is due to the coexistence of the three rotational

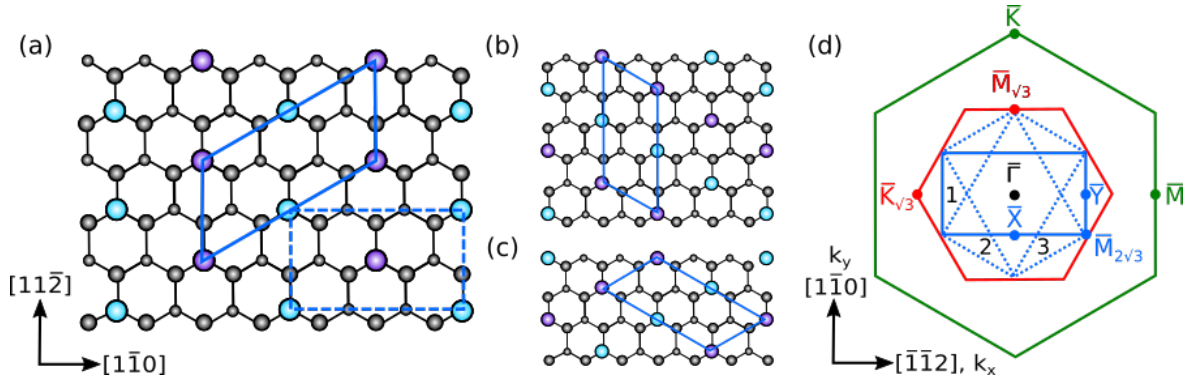


Figure 6.5: (a) Schematic top view of the row-wise collinear antiferromagnetic spin ordering of α -Sn. Blue and purple circles represent Sn atoms on T_4 adsorption sites with different spin polarizations; Si atoms are gray. Oblique (blue) and rectangular (blue dashed) $(2\sqrt{3} \times \sqrt{3})$ -Sn unit cells of the horizontal domain are marked with lines. (b) and (c) 120° rotational domains of $(2\sqrt{3} \times \sqrt{3})$ -Sn, labeled as domain 2 or 3, respectively. (d) SBZs of the (1×1) (green), $(\sqrt{3} \times \sqrt{3})$ (red) and three rotational $(2\sqrt{3} \times \sqrt{3})$ domains (blue). High symmetry points are indicated. The domain labeled as '1' is referred to as the horizontal domain, while domains '2' and '3' are termed rotated domain structures.

domains on the surface of the sample, which have slightly different dispersions if measured along high symmetry points of the $(\sqrt{3} \times \sqrt{3})$ reconstruction [21, 205].

6.3.1 Spin-integrated constant energy and band maps

For further investigations of the insulating ground state, a CEM of the α -Sn phase, illustrated in Fig. 6.6, was taken at 0.38 eV below the Fermi energy E_F . This energy was chosen since it yields an acceptable signal-to-noise ratio. Like all following ARPES measurements, it was done at $T \approx 40$ K, well below the phase transition temperature. A surface state with high intensity is observed around the \bar{M} points of the $(\sqrt{3} \times \sqrt{3})$ and two domains of $(2\sqrt{3} \times \sqrt{3})$ unit cells. The local minimum of this dispersing state is located at $\bar{K}_{\sqrt{3}}$. The SBZ boundaries and symmetry points of both reconstructions are superimposed for clarification.

Band maps along two high symmetry directions are shown in Figs. 6.7(a) and (b). They clearly reveal the insulating nature of the ground state at low temperature. For better orientation, the valence band maximum of Si is marked. In order to characterize the surface states in more detail, an enlargement of the region marked by rectangles in Figs. 6.7(a) and (b) is shown in Fig. 6.8. Clearly, the surface state along the k_x direction reveals a w shape with minima around 0.6 eV binding energies located at the $\bar{K}_{\sqrt{3}}$ points (cf. Fig. 6.8(c)). A pronounced broadening of all surface states is obvious and was also seen in other high-resolution ARPES experiments [21]. As shown in the following, this apparent smearing is rather an effect of the multidomain structure of the $(2\sqrt{3} \times \sqrt{3})$ reconstruction and the Rashba-type spin splitting of the surface states than a lack of resolution.

Figure 6.8 shows a comparison between the measured MDCs and the band structure based on previous calculations [21, 205]. Starting with the k_x direction, there is some intensity in the vicinity of the $\bar{\Gamma}$ point, which can be seen more clearly in the curvature fit of the band map shown in panel (e). This faint feature was observed before, and its position at around

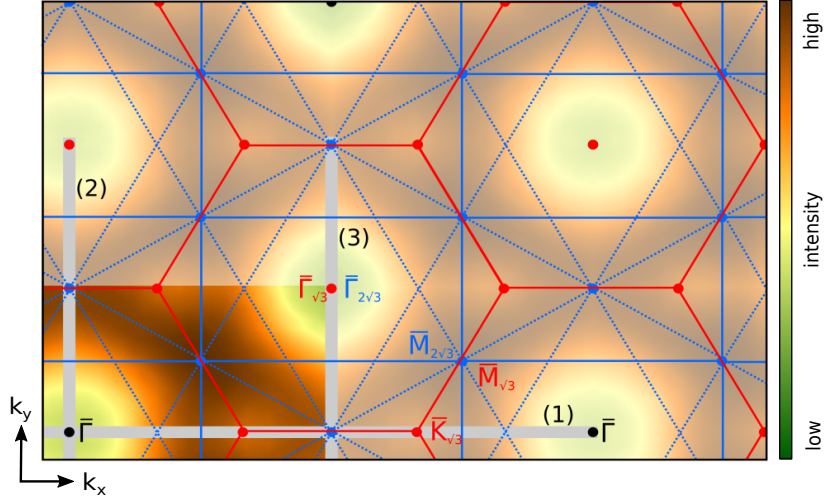


Figure 6.6: Extended CEM taken at $E_B = 0.38$ eV and $T \approx 40$ K. Only the phase space shown in the lower left was measured. The superimposed red and blue lines show the SBZ of the $(\sqrt{3} \times \sqrt{3})$ and of the three rotational domains of $(2\sqrt{3} \times \sqrt{3})$, respectively. Dots symbolize high symmetry points of both structures; gray lines highlight the directions of the (S)ARPES measurements.

0.4 eV binding energy is indicative for the broken $(\sqrt{3} \times \sqrt{3})$ symmetry [21]. Moreover, the MDC shown in Fig. 6.8 (a) reveals a multipeak structure which is visible also in the curvature plot of the data (Fig. 6.8 (e)).

Quantitative agreement for the positions of the multipeak MDC structure with calculations is obtained if contributions of the surface state from different domains are taken into account. The solid and dashed blue curves display calculated spin-degenerate surface bands for the horizontal (domain 1) and the rotated domains, respectively. The band structures for the $(2\sqrt{3} \times \sqrt{3})$ reconstruction were taken from Lee et al. [205]. Thereby, the dashed curve in Fig. 6.8 is the projection of the band structure from two rotated domains and thus should comprise twice as much intensity compared to the band belonging to domain 1, drawn with a solid line. Indeed, this trend is seen in the MDC, at least for the first sequence of peaks. The gradual damping of the signal along the k_x direction comes either from a slight azimuthal misalignment of the scan direction, changes in the dipole selection rules with changing incidence angle of light, and/or the physisorption of UHV rest gas. As shown in the next section, the Rashba-type spin splitting along the k_x direction is approximately five times smaller than the band splitting seen in the MDC, thus already the analysis of the spin-integrated data provides clear evidence for the collinear antiferromagnetic ordering with $(2\sqrt{3} \times \sqrt{3})$ symmetry.

Along the k_y direction the band structure, displayed in Figs. 6.8 (d) and (f), consists of two bands as well. In contrast to the k_x direction, the bands disperse less [205]. While the band originating from domain 1 disperses at binding energies between 0.2 – 0.3 eV, the other band is located between 0.3 – 0.45 eV. Thus, the MDC taken at $E_B = 0.38$ eV does not comprise any bands from domain 1 but four peaks from domains 2 and 3. Contrary to the k_x direction, the splitting along the k_y direction is mainly due to spin-orbit interaction as shown in the

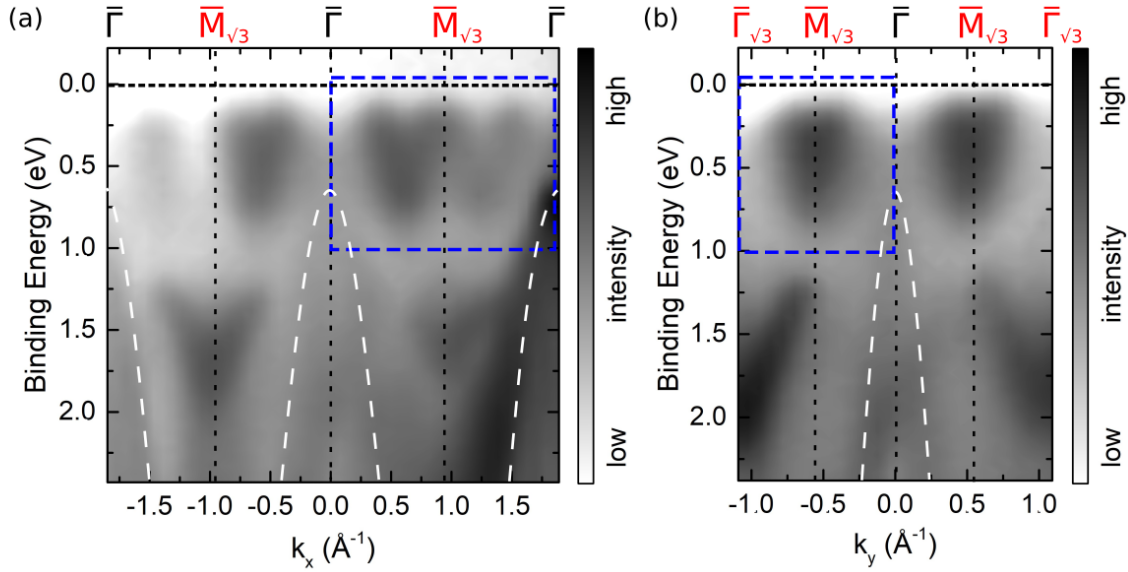


Figure 6.7: (a) Band map along the k_x direction (1) as denoted in Fig. 6.6. (b) Band map along the k_y -direction (2). Dashed white curves show the positions of the Si valence band. Details of the band maps within the blue boxes are shown in Fig. 6.8.

following. Again, the interpretation of the spin-integrated ARPES data already indicates the $(2\sqrt{3} \times \sqrt{3})$ symmetry.

6.3.2 Spin-resolved band structure

For investigations on these surface bands, MDCs were taken again at $E_B = 0.38$ eV along k_y (part of the direction is marked by (3) in Fig. 6.6), but with right (C^+) and left (C^-) circularly polarized light at a photon energy of $h\nu = 44$ eV. Figure 6.9 (a) shows the corresponding band map along the k_y direction. Notably, the Si valence bands are seen here as replica structures around the $\bar{\Gamma}_{\sqrt{3}}$ points, which indicates the long-range ordering of the α -Sn reconstruction.

Both MDCs have roughly the same shape, but they show deviations in intensity on the side of the peaks originating from the surface bands. This means that those states show circular dichroism (cf. chapter 3.3.3), which indicates that spin-orbit interaction plays an important role and the states have to be described by different quantum numbers. A more detailed analysis was done by plotting the difference and fitting the sum of C^+ and C^- spectra in panels (c) and (d), respectively. The helicity dependent photoemission intensity is ascribed to two spin-orbit split states symmetrically shifted around the time-reversal invariant $\bar{M}_{\sqrt{3}}$ points. Within the errors of the measurement, the splitting is identical to the splitting discussed in the context of Fig. 6.8 (b). As shown below the circular dichroism is most likely a result of Rashba-type spin splitting of the surface states.

In order to quantify the spin texture of the surface states and to rule out that matrix element effects entirely govern the dichroitic signal, SARPES measurements were performed, again at a binding energy of $E_B = 0.38$ eV. Figure 6.10 (a) shows the spin-resolved MDC along the k_x direction. A comparison with the spin-integrated signal shown in Fig. 6.8 (a)

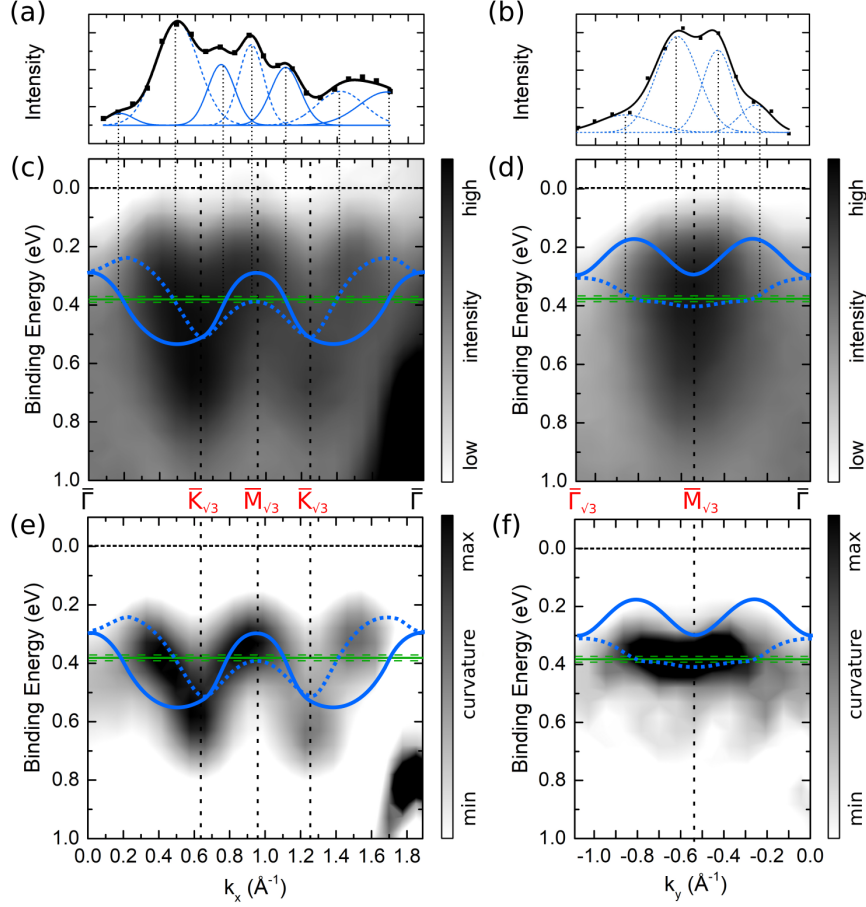


Figure 6.8: (a), (b) MDCs along the k_x and k_y directions taken at 0.38 eV, respectively. (c), (d) Band maps along the k_x and k_y directions. (e), (f) Curvature maps of (c) and (d) to highlight details of the band structure. Green lines show the position of the MDCs. Solid and dashed blue curves indicate (spin-degenerated) calculated surface bands from domain 1 and domains 2, 3 of the $(2\sqrt{3} \times \sqrt{3})$ structure, respectively. The band structure was taken from Ref. [205].

yields qualitatively the same shape. The measurement was started this time from the high momentum side, i.e., the gradual drop in intensity is most likely induced by physisorption of residual gas. The three measured spin components calculated according to chapter 4.2.1, shown in Fig. 6.10 (b), clearly reveal a pronounced in-plane spin polarization of the surface states (nonvanishing S_x, S_y).

A simultaneous description of all four data sets ($S_{x,y,z}$ and total intensity) is achieved only if a peak substructure shown in Fig. 6.10 (a) is considered: First of all, each intensity feature comprises a doublet structure which accounts for the Rashba-splitting. The presence of a doublet with opposite spins is partly visible also in the raw data, e.g., from the rapid change of amplitude of the S_y component around 1.5 \AA^{-1} . Secondly, the most intense MDC peaks discussed in the context of Fig. 6.8 (a) (dashed lines, rotated domains) are considered by the three intense double peak structures (marked by green and orange lines). Furthermore,

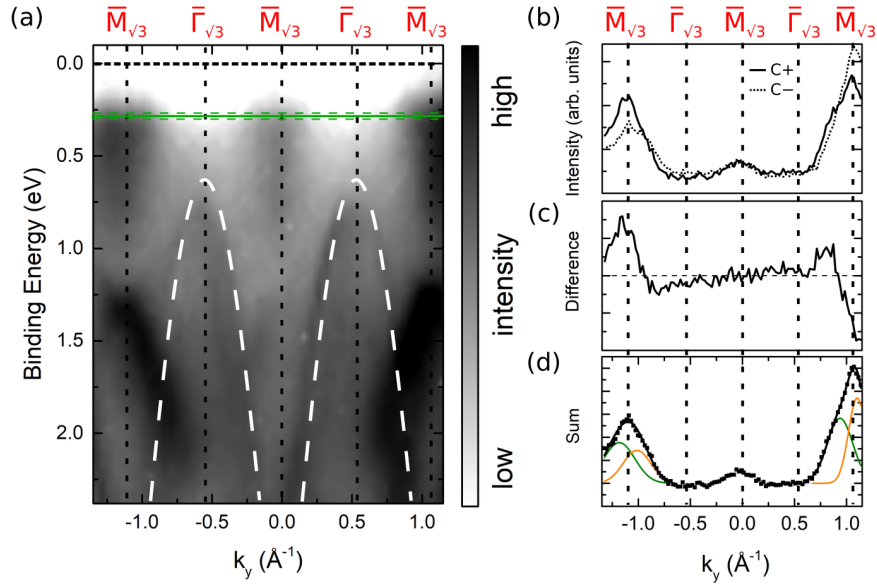


Figure 6.9: (a) Band map along the direction denoted by (3) in Fig. 6.6. The dashed curves show the $(\sqrt{3} \times \sqrt{3})$ -replica states of the Si valence bands. (b) MDCs taken along the k_y direction, as indicated by the green line in (a), with C^+ and C^- polarization. (c) and (d) show the difference and sum of the two MDC spectra, respectively.

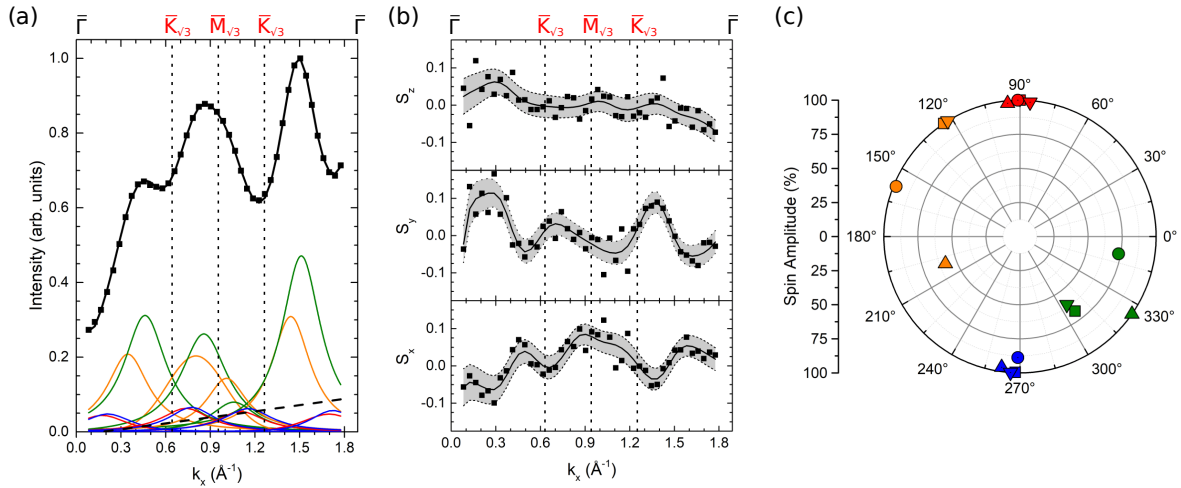


Figure 6.10: (a) Spin-resolved MDC along the k_x direction taken at 0.38 eV below E_F . The upper axis shows the high symmetry points (cf. Fig. 6.5(c)). (b) Corresponding spin-polarization vectors S_x , S_y , and S_z . The shaded areas represent the uncertainty by simultaneously fitting all four data sets. (c) S_x - and S_y -spin components of the peaks shown in (a). The 0° and 90° denote the positive x and y directions, respectively.

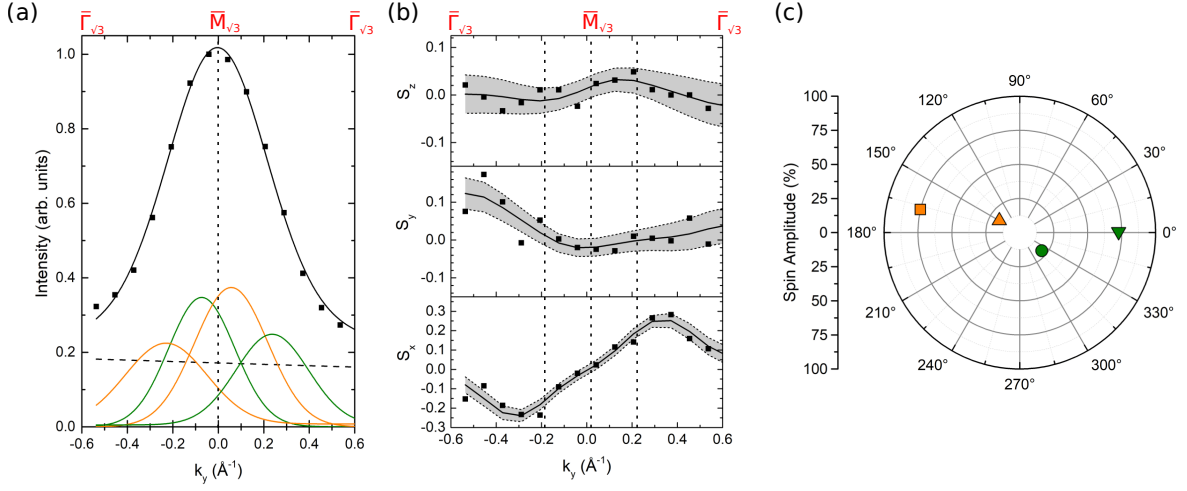


Figure 6.11: (a) Spin-resolved MDC along the k_y direction taken at 0.38 eV below E_F . The upper axis shows the high symmetry points of the three domains. (b) Corresponding spin-polarization vectors S_x , S_y , and S_z . The shaded areas represent the uncertainty by simultaneously fitting all four data sets. (c) S_x - and S_y -spin components of the peaks shown in (a). The 0° and 90° denote the positive x and y directions, respectively.

the less intense peaks seen in Fig. 6.8 (a) (solid lines, domain 1) were detectable and taken into account by a corresponding sequence of double peaks (red and blue curves). It should be emphasized that a better agreement is obtained if instead of six peaks, eight peaks are considered for the rotated domains in Fig. 6.10 (a). Any modeling with fewer peaks was not able to describe the variations in the magnitude of the three spin polarizations satisfyingly. As already pointed out, at the constant energy of 0.38 eV the surface bands originating from these domains are barely touched (cf. dashed lines in Fig. 6.8 (c)). For the measurements with the Mott detectors, the energy resolution is lower, and the larger integration area is most likely the reason for this observation. Based on this initial guess, a satisfying modeling of the experimental spin-resolved data succeeded.

A polar plot of the resulting in-plane spin components S_x and S_y is shown in Fig. 6.10 (c): Indeed, each of the doublet structures reveals de-facto an opposite spin orientation, as expected for conventional Rashba-split states. The splitting is around $\Delta k_x \approx 0.05 \text{ \AA}^{-1}$, which means that a correlated quantum state with weak spin-orbit coupling can describe the α -Sn phase [18]. Furthermore, the less intense peaks belong to domain 1, in agreement with the assignments done in Figs. 6.8 (a) and (c). Consequently, due to the mirror plane of this domain, only S_y spin components are observed for the k_x direction (cf. chapter 3.3.3). Contrary, the spin vectors originating from the rotated domains show both S_x and S_y components. The spin texture from these states originates from both domains. Therefore, any imbalance between these two domains will cause a finite S_x component [143]. Nevertheless, the analysis is fully consistent with the conclusions from the previous section and supports the formation of $(2\sqrt{3} \times \sqrt{3})$ domains. The finding of in-plane spin components suggests an in-plane anti-ferromagnetic ordering between the Sn sites. Similar magnetization patterns were previously reported for Mn/W(110) [209].

Besides the k_x direction, the spin components of the surface state along the k_y direction

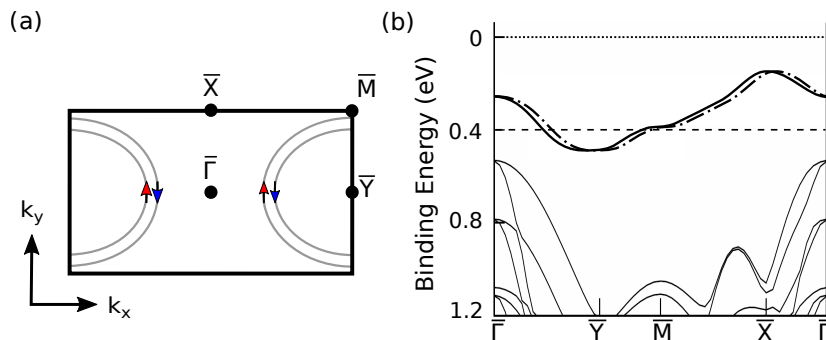


Figure 6.12: (a) Electronic structure and spin texture in the SBZ of the $(2\sqrt{3} \times \sqrt{3})$ structure at a binding energy of approximately 0.4 eV with a Rashba-splitting of $\Delta k \approx 0.05 \text{ \AA}^{-1}$. (b) Band structure reproduced after Lee et al. [205]. The Mott state was complemented by a Rashba-type spin splitting.

was also measured (cf. Fig. 6.11). According to the discussion in the context of Fig. 6.8 (d) the surface state at around 0.38 eV binding energy is formed by states of the rotated domains. A four-peak structure is mandatory for the momentum range in order to describe the MDC intensity and three spin-component data sets satisfyingly. Clearly, the adjacent peaks show an alternating spin structure. However, the apparent larger Rashba-splitting of $\Delta k_y \approx 0.2 \text{ \AA}^{-1}$ is a result of the intersection of the Mott states from adjacent zones and not an indication of an anisotropic spin texture, as shown below. If both domains were equally distributed, only the S_x component should show up. The finite value of S_y component reflects the asymmetry between these two domains, in accordance with the conclusions drawn above.

6.3.3 Model for the spin-texture of the α -Sn phase

For the spin-ordered $(2\sqrt{3} \times \sqrt{3})$ structure, Lee et al. [205] calculated a band structure for one domain containing one only slightly dispersing surface band with a binding energy between approximately 0.1 and 0.5 eV. In accordance with the results in this work concerning the spin-orbit interaction, a Rashba-type spin splitting of $\Delta k \approx 0.05 \text{ \AA}^{-1}$ is superimposed in Fig. 6.12 (b) while maintaining spin degeneracy at time-reversal invariant momenta. Consequently, the rectangular SBZ comprises two almost circularly shaped bands around the \bar{Y} point with opposite spin directions, as seen in Fig. 6.12 (a). Along the mirror plane xz in the k_x direction, crossing through $\bar{\Gamma}$ and \bar{Y} , the spin components S_x and S_z are zero and only S_y has a finite value in agreement with the reported finding.

In Fig. 6.13 all three rotational domains are depicted in an extended zone scheme. The surface bands of different domains overlap each other resulting in a complex electronic structure model. Looking along the k_x direction, i.e., $\bar{\Gamma}\bar{Y}$ of the horizontal domain, one finds an alternating spin structure originating either only from domain 1 or an overlap of the surface bands of the two other domains 2 and 3 (numbering refers to Fig. 6.5 (c)). Along the k_y direction, $\bar{\Gamma}\bar{X}$ of domain 1, only bands of domains 2 and 3 appear. The domains are spatially separated, and no interaction between the bands of different domains can be expected. However, in measurements, the spin-polarization at these points with overlapping bands will depend on the distribution and size of the three domains.

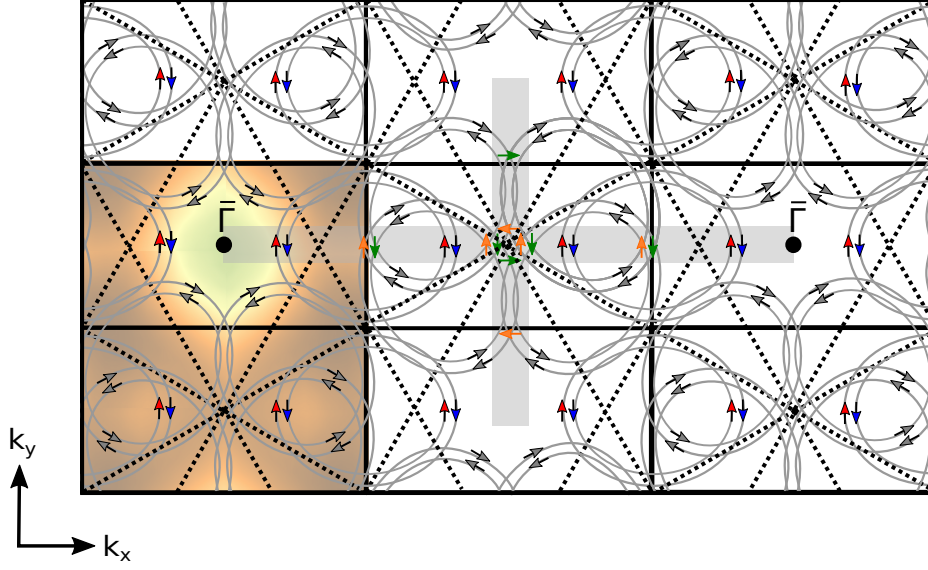


Figure 6.13: SBZ consisting of three rotational ($2\sqrt{3} \times \sqrt{3}$) domains. Red and blue spin vectors belong to the horizontal domain as seen in Fig. 6.12(a). Spin components of the other two domains are shown in gray, the resulting spins of those domains along the k_x and k_y direction in orange and green. The broad gray lines indicate the positions of measurements along the k_x and k_y direction shown in Fig. 6.8 and coincide with the lines denoted by (1) and (3) in Fig. 6.6.

6.4 Summary and conclusion

In summary, the spin-orbit interaction of the correlated α -Sn structure on Si(111) with a Sn coverage of $\theta = 1/3$ ML was investigated directly with spin- and angle-resolved photoemission. This phase structurally shows a $(\sqrt{3} \times \sqrt{3})$ reconstruction even below the metal-insulator phase transition temperature of $T_c \approx 70$ K. Spin-resolved band structures at low temperatures were identified which originate from a $(2\sqrt{3} \times \sqrt{3})$ symmetry, in agreement with previous theoretical studies [21, 205]. This symmetry is mandatory for the formation of a row-wise collinear antiferromagnetically ordered spin arrangement of the Sn atoms adsorbed on T_4 positions with a $(\sqrt{3} \times \sqrt{3})$ order. As it turns out, the Rashba-splitting is comparably small, and the spin-orbit interaction is weak in this structure. According to the spin orientation in the ARPES experiments, an in-plane ordering of the spins in the antiferromagnetic phase is proposed.

There is currently a debate whether the insulating state is driven by electronic correlation effects or by spin-ordering [21, 205]. In the latter case, where the ground state is characterized as a Slater-type insulator via band magnetism, the antiferromagnetic ordering should come along with nesting in between helical states. However, a doubling of the unit cell, as seen for Pb/Si(557) [41], was not observed. Moreover, no indications of hybridization between the Sn states and the Si valence bands ($3p_z$ states) were observed, which enables the superexchange. Therefore, the α -Sn/Si(111) phase should instead be described as a weakly spin-orbit coupled Mott system [18].

Formation of Sn-induced nanowires on vicinal silicon surfaces

A potential candidate for nanowires revealing electronic correlation effects is the Sn/Si(557) system. As discussed in chapter 6, its 2D analog, i.e., the α -Sn phase on Si(111), gives rise to a weakly spin-orbit coupled Mott phase, even though the SOC strength and the resulting Rashba-splitting is significantly smaller compared to the isoelectronic Pb. Electronically, the Mott phase exhibits a $(2\sqrt{3} \times \sqrt{3})$ unit cell due to the antiferromagnetic ordering between adjacent Sn rows of the $(\sqrt{3} \times \sqrt{3})$ -structure [21, 182].

The targeted manipulation of such kind of Mott-systems offers a wide range of possibilities. For instance, doping leads to various phases like high-temperature superconductivity [70], charge-transfer insulators [71], or robust metallic states [74], that are described in more detail in chapter 2.1.3. For α -Sn on Si(111), a metallic quasi-particle state was found within the Mott gap if the system is modified by means of the acceptor concentration of the Si substrate [46]. In this context, the growth of Mott-phases of finite widths on stepped substrates is interesting and was not considered before. Step edges may provide binding sites with electronic properties different from the flat surface, leading to partially ionized atoms. In the case of Ag/Si(557), this results in doping of electrons to the nanowires [79]. Besides, a refacetting similar to Pb/Si(557) implies a terrace width of approximately the same size as one unit cell of the low-temperature $(2\sqrt{3} \times \sqrt{3})$ structure and might suppress the formation of it.

In the scope of this chapter, the growth of Sn on Si(557) is analyzed in order to elucidate the possibility to form defined nanowires. By choosing different coverages, three distinct phases were identified by means of STM and LEED. Deposition of more than 0.5 ML of Sn leads to the formation of the high coverage $(2\sqrt{3} \times 2\sqrt{3})$ phase on (111) terraces that destabilizes the triple steps, resulting in a local (223) orientation. If the $(2\sqrt{3} \times 2\sqrt{3})$ stripes grow larger, step bunching occurs, eventually resulting in a surface covered by large (111) terraces. Only for lower Sn coverages, ordered stripes of Sn wires with a structural $(\sqrt{3} \times \sqrt{3})$ reconstruction separated by triple steps were found. As observed by ARPES, this confinement destroys the insulating nature of the spin-split ground state, pointing towards a finite-size induced quenching of the Mott state.

Samples were prepared using well oriented surfaces of phosphorous-doped Si(557) with a resistivity of less than $< 5 \text{ m}\Omega\text{cm}$, which were degassed at 500°C for several hours and

repeatedly flash annealed to 1150 °C until a sharp (7×7) reconstruction and step-train patterns were seen in optical LEED. In order to prepare the three types of nanowires, different amounts of Sn, i.e. 0.4 monolayer ($\text{ML} = 7.8 \times 10^{14} \text{ cm}^{-2}$, defined with respect to Si(111)), 0.6 ML and 0.9 ML, were deposited at a rate of around 0.02 ML/min on the surface. During evaporation, the substrate is kept at a temperature of $(570 \pm 20)^\circ\text{C}$.

The samples were investigated by means of LEED, STM and ARPES. LEED and STM measurements were performed at room temperature. ARPES measurements were done at the COPHEE endstation at the SIS beamline of the Swiss Light Source (cf. chapter 4.2), using C^+ and linearly p polarized light with a photon energy of 44 eV. The photoemission experiments were carried out with an energy and angle resolution of 25 meV and 0.5° at low temperatures (40 K), well below the phase transition temperature of ~ 70 K for the α -Sn phase on Si(111) (cf. chapter 6).

The results presented here were previously published in “Formation of Sn-induced nanowires on Si(557)” [210], and will not be cited separately.

7.1 Growth of Sn on Si(557)

The possibility of growing Sn nanowires on Si(557) was investigated by evaporation of sub-monolayer Sn coverages, which results in the formation of three distinct phases. Fig. 7.1 shown large scale STM images and LEED patterns with different Sn coverages of 0.4 ML (panel (a),(d)), 0.6 ML ((b),(e)) and 0.9 ML ((c),(f)). For the lowest Sn coverage of 0.4 ML, the former step structure of the Si(557) surface is preserved as deduced from the spot splitting of $\Delta k = 0.1 \text{ \AA}^{-1}$ around the (1×1) diffraction spots in LEED along the $[11\bar{2}]$ -direction. In addition, a weak $\times 2$ streak is visible as well as pronounced $(\sqrt{3} \times \sqrt{3})$ diffraction spots. The homogeneously stepped surface can be confirmed by STM, showing a nanowire-like structure. A slight azimuthal miscut restricts the length of the wires to approximately 200 nm.

Covering the Si(557) surface with a larger Sn coverage, i.e. 0.6 ML, the structure of the surface changes entirely (cf. Figs. 7.1 (b) and (e)). Sharp diffraction spots seen in LEED between the (1×1) spots in the $[1\bar{1}0]$ -direction reveal spot splitting of a homogeneously stepped (223) surface orientation, similar to the adsorption of Pb/Si(557) [41]. Again $(\sqrt{3} \times \sqrt{3})$ diffraction spots are visible, but in addition also diffraction spots originating from a $(2\sqrt{3} \times 2\sqrt{3})$ reconstruction are present. In consequence of the formation of (223) facets, the initial (557)-oriented surface builds up larger (111)-areas in order to maintain the average inclination. This local refacetting shows up in STM by the formation of bundle-like structures. Their width is around 20 nm and, compared to the low coverage phase, the length decreases down to 100 nm.

Increasing the coverage even further to 0.9 ML, the diffraction spots coming from (223) orientation vanish in LEED (Fig. 7.1 (f)). The $(2\sqrt{3} \times 2\sqrt{3})$ reconstruction becomes more intense and a streaky feature appears at the $\times 2$ positions. However, the appearance is quite similar to the intermediate coverage phase. The nanowire bundles still exhibit approximately the same size, but now the structure of these bundles can be resolved more clearly even in a large scale STM picture shown in Fig. 7.1 (c). They seem to consist of few nanowires which appear to be much wider than in the case of less Sn coverage. In the following, the atomic structure of the nanowires at the different Sn coverages will be explained in more detail.

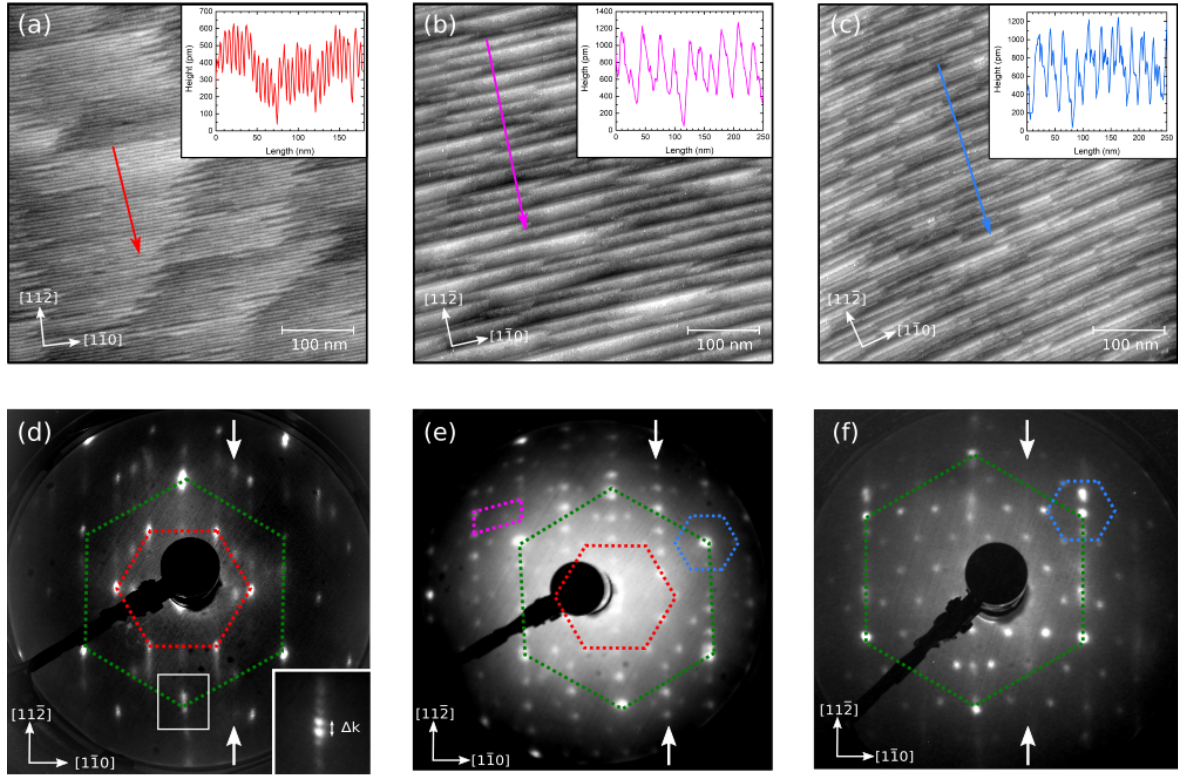


Figure 7.1: (a–c) STM images of Sn coverage dependent phases on Si(557): (a) 0.4 ML (tunneling condition $V = -1$ V, $I = 1$ nA), (b) 0.6 ML ($V = 1$ V, $I = 0.1$ nA) and (c) 0.9 ML ($V = -2$ V, $I = 0.1$ nA). Arrows indicate the directions of the linescans shown in the insets. (d–f) LEED images taken at electron energies around 80 eV corresponding to the STM pictures shown above. Dashed lines indicate the (1×1) (green), $(\sqrt{3} \times \sqrt{3})$ (red), $\times 2$ (purple) and $(2\sqrt{3} \times 2\sqrt{3})$ (blue) unit cells in reciprocal space, white arrows show the $\times 2$ positions. Inset in (d): Enlarged area around the (1×1) spot highlighting the spot splitting Δk across the step direction of the Si(557).

7.1.1 Intermediate and high coverage nanowires

The α -Sn phase on Si(111), which is described in detail in chapter 6, comprises ideally $1/3$ ML. For higher coverages a mixture of $(\sqrt{3} \times \sqrt{3})$ and $(2\sqrt{3} \times 2\sqrt{3})$ domains is expected, according to the phase diagram for Sn/Si(111) [183] (cf. Fig. 6.1). The latter phase has a nominal Sn coverage of around 1.2 ML [185]. Although the atomic structure is still under debate, latest results favor the model by Toernevik et al. containing 14 Sn atoms per unit cell arranged in a double layer, with its top layer comprising of four atoms [187, 190].

The (111)-terrace size of the clean and homogeneously stepped Si(557) surface is 1.9 nm, thus large enough to form a $(2\sqrt{3} \times 2\sqrt{3})$ unit cell. Obviously, a different scenario is energetically favored, as seen in Fig. 7.2 for 0.6 ML Sn. The double layered $(2\sqrt{3} \times 2\sqrt{3})$ structure destabilizes the step structure of the Si(557) surface and increases the width of the (111) terraces. The (111) terraces are between 5 and 20 nm wide and, indeed, a phase mixture of $(\sqrt{3} \times \sqrt{3})$ and $(2\sqrt{3} \times 2\sqrt{3})$ reconstructions is observed on them (Fig. 7.2 (b)). As a consequence, steeper areas are formed resembling locally a (223) facet structure. They consist

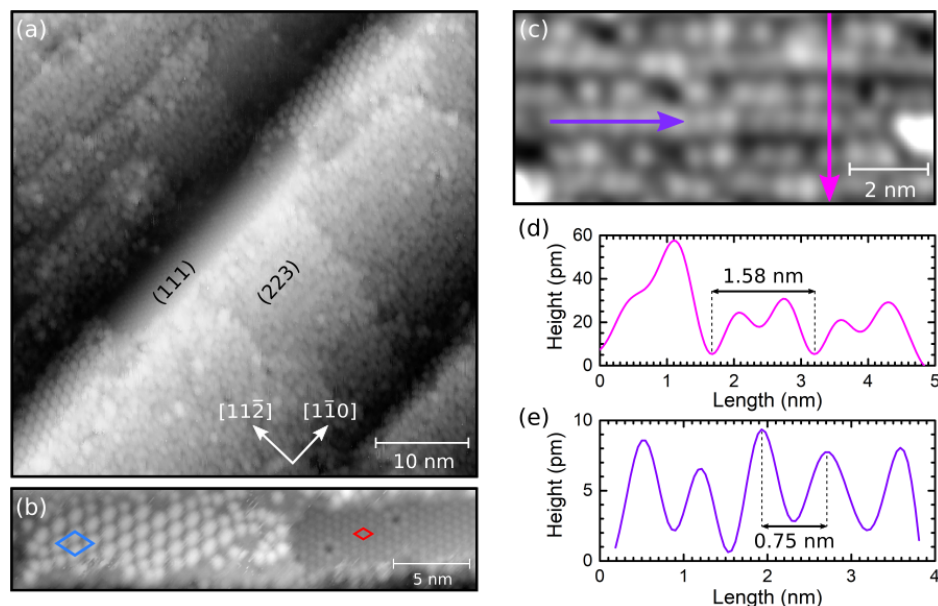


Figure 7.2: (a) STM image ($V = -1$ V, $I = 0.1$ nA) of the 0.6 ML Sn phase on Si(557). (b) Enlarged image of the coexisting $(\sqrt{3} \times \sqrt{3})$ and $(2\sqrt{3} \times 2\sqrt{3})$ structure on the (111) terraces taken at (-1 V, 80 pA), unit cells are indicated in red and blue, respectively. (c) Enlarged image of the (223) oriented part (-1 V, 50 pA). The arrows indicate the directions where the line scans, shown in (d) and (e), were taken.

of small steps with a distance of 1.58 nm, as seen in Figs. 7.2(c) and (d). On each step, two rows of Sn atoms can be resolved. Along the chains the Sn atoms have a spacing of $2a_{\text{Si}} = 0.75$ nm (see Fig. 7.2(e)), corresponding to the sharp $\times 2$ phase seen in LEED (cf. Fig. 7.1(e), purple unit cell). This reconstruction is concomitant with a step-step correlation within the (223)-facet structure giving rise to the sharp diffraction spots and has been seen for other systems as well [211, 212]. As obvious from Fig. 7.2(c), these atomic chains are not as free of defects as other nanowire systems on vicinal substrates (cf. chapter 8). In order to improve the long-ranged order along the steps, additional 0.1 ML of Sn were added with the substrate temperature kept at 550 °C. However, the additional Sn tends to accumulate only on the (111) terraces, not on the (223) facets, resulting in even larger $(2\sqrt{3} \times 2\sqrt{3})$ domains on the (111) terraces, and eventually covering the entire terrace when the Sn coverage is increased even more.

Above a Sn coverage of $\approx 2/3$ ML, the high coverage nanowire phase represents the majority. The wider (111) terraces are completely covered by a $(2\sqrt{3} \times 2\sqrt{3})$ reconstruction and further excess Sn would have to accumulate on the local (223) orientated parts. Although these small terraces provide a width suitable for the formation of a $(2\sqrt{3} \times 2\sqrt{3})$ unit cell, larger domains are favored and further Sn deposition leads to step bunching, resulting in a surface dominated by large (111) terraces (Fig. 7.3(a)). They are entirely covered by a $(2\sqrt{3} \times 2\sqrt{3})$ reconstruction. The terrace widths appear to be quite irregular, but they are usually a multiple of 1.33 nm, which is the lattice constant of the Sn reconstruction.

Summarizing this part, the formation of extended α -Sn phases, which may undergo a metal to insulator transition at low temperatures, and $(2\sqrt{3} \times 2\sqrt{3})$ reconstructions on (111) areas

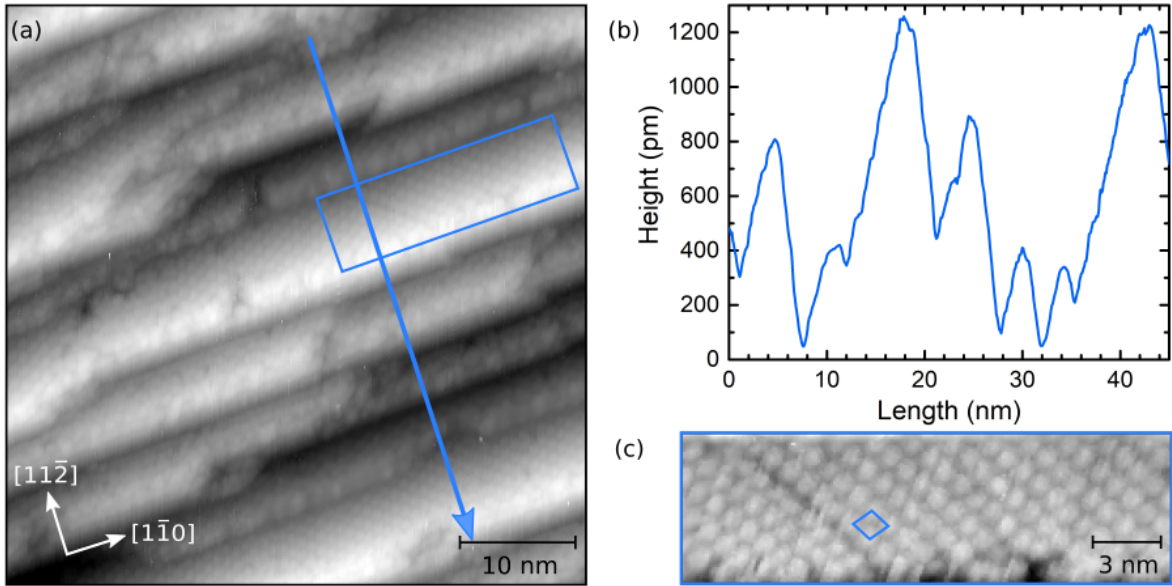


Figure 7.3: (a) STM image of the 0.9 ML Sn phase on Si(557). Blue arrow indicates the direction of the linescan shown in (b). (c) Enlarged image of the $(2\sqrt{3} \times 2\sqrt{3})$ structure on the terraces. The unit cell is indicated in blue. Images were taken at ($V = 2$ V, $I = 60$ pA)

drive the refacetting of the initial Si(557) orientation. This is in contrast to Pb/Si(557), where the nesting condition found for Pb/Si(557) favors the formation of a (223) facet structure with a well defined atomic Pb-induced reconstruction [41, 112] (see chapter 2.3 and 8 for more details).

Intermediate coverage nanowires grown on a Si(223) substrate

A further approach for decreasing the defect sites of the intermediate coverage nanowires was made by changing the inclination angle of the Si substrate. Although Si(557) is widely used as a template for nanowires growth (e.g., [213–216]), it might not always be the ideal choice. As mentioned above, for the intermediate coverage nanowires, the formerly (557) oriented substrate surface is locally modified to (223) facets that are separated by wider (111) terraces. In order to avoid the latter and improve the long-range ordering of the nanowires, the feasibility of growing Sn nanowires on a Si(223) substrate was studied.

The Si(223) substrate itself is inclined by 11.4° towards $[\bar{1}\bar{1}2]$ compared to the flat (111) surface [217], which is approximately 2° more than in case of Si(557) [218]. By means of LEED, a faint indication of a steptrain along the $[\bar{1}\bar{1}2]$ direction is visible (see Figs. 7.4 (a)). Its spot splitting $\Delta k \approx 11$ %SBZ corresponds to an average terrace width of $9a_{\text{Si}} \approx 3$ nm separated by double steps, with $a_{\text{Si}} = 0.352$ nm being the Si lattice constant in $[\bar{1}\bar{1}2]$ direction. This is confirmed by STM measurements and a linescan taken perpendicular to the steps (cf. Fig. 7.4 (b) and (c)), which show a homogeneously faceted surface. However, the step edges appear to be quite rough and irregularly shaped, which might explain the high background intensity observed in LEED.

Around 0.6 ML Sn were evaporated on this surface, following the same procedure as for

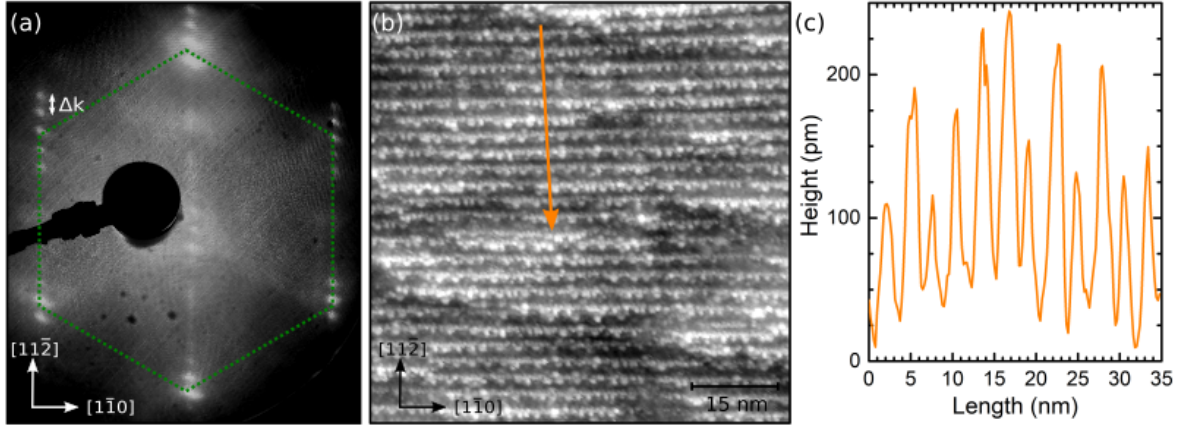


Figure 7.4: (a) LEED taken at an electron energy of 60 eV and (b) STM images ($V = -1.1$ V, $I = 50$ pA) of the bare Si(223) substrate. Dashed lines highlight the (1×1) (green) and $(\sqrt{3} \times \sqrt{3})$ (red) unit cells in reciprocal space. The arrow in (b) indicates the position of the linescan shown in (c).

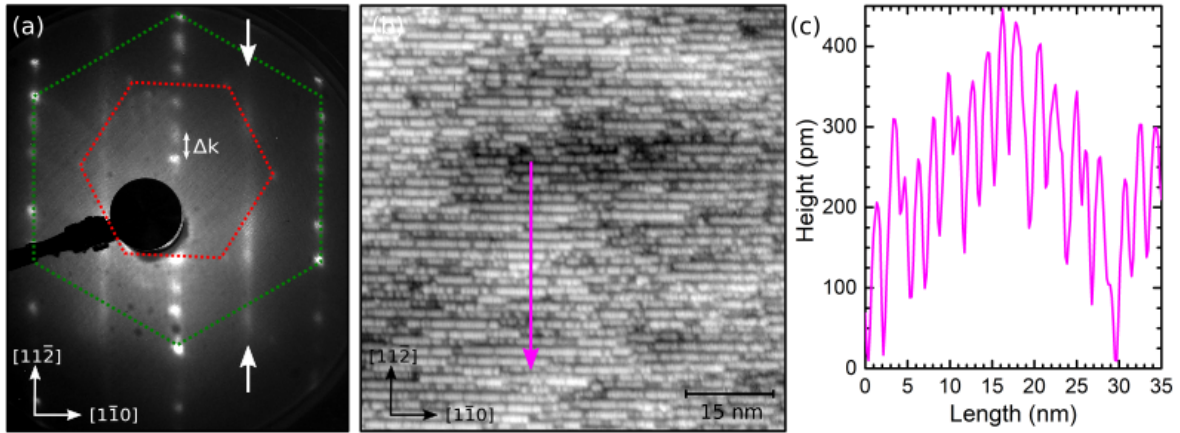


Figure 7.5: (a) LEED taken at an electron energy of 60 eV and (b) STM images ($V = 1$ V, $I = 60$ pA) of the 0.6 ML Sn phase on Si(223). Dashed lines highlight the (1×1) (green) and $(\sqrt{3} \times \sqrt{3})$ (red) unit cells in reciprocal space, white arrows the $\times 2$ positions. The arrow in (b) indicates the position of the linescan shown in (c).

the intermediate coverage wires grown on Si(557). Evoked by the Sn evaporation, the surface reconstruction changes from a double-stepped to a single-stepped topography. This is seen in Fig. 7.5 via LEED and STM images, as well as a linescan taken along the direction perpendicular to the Sn nanowires. The splitting between adjacent diffraction spots along the steptrain turns out to be the same as for Sn/Si(557), namely $\Delta k = 21.3\%$ SBZ, which corresponds to a terrace width of $4\frac{2}{3} a_{\text{Si}} = 1.55$ nm. Hence, the Sn-induced single-stepped (223) orientation is stable even without the close vicinity of wider (111) terraces. However, in Fig. 7.5 (a) faint $(\sqrt{3} \times \sqrt{3})$ diffraction spots are observable, which originate from the Sn reconstruction on (111) terraces. This leads to the conclusion, that some wider (111) terraces are yet present on the surface, although their amount is much less than for Sn/Si(557). Furthermore, the quality nanowires itself is not improved by the use of this substrate. They still show a similar defect density, that remains unchanged upon further Sn adsorption. Besides, the interchain coupling is reduced in this case, according to the LEED image. Compared to Sn/Si(557) (see Fig. 7.1 (e)), the diffraction pattern has changed at the $\times 2$ position. Instead of distinct spots indicating a long-range intrachain correlation, it appears for Sn/Si(223) as a streaky feature. Contrary to similar phases reported for Pb/Si(557) [219], it is not possible to convert one phase into the other by high-temperature annealing.

7.1.2 Low coverage nanowires: a pseudo-gapped Mott state?

For the low Sn-coverage regime the initial surface structure of Si(557) is preserved. The spacing between two adjacent terraces is 5.73 nm (cf. Fig. 7.6 (b)) which corresponds to the spot splitting observed by LEED. STM measurements shown in Fig. 7.6 reveal that the surface structure consists of approximately 3 nm wide (111) terraces covered with a $(\sqrt{3} \times \sqrt{3})$ -Sn structure separated by triple steps, similar to Ag/Si(557) [215]. The $(\sqrt{3} \times \sqrt{3})$ -Sn reconstruction on the mini-(111) terraces is well-known for the α -Sn phase on Si(111) with a coverage of $1/3$ ML [184, 185]. The $\times 2$ -periodicity originates from Si-dimers along the step edges. The edge roughness is mainly a result of the zig-zag edges of the Sn-reconstruction along the $[1\bar{1}0]$ -direction.

Compared to higher coverage phases, only the 0.4 ML Sn-phase on Si(557) results in the formation of a homogeneously stepped structure with defined 3 nm wide stripes hosting a α -Sn reconstruction. As mentioned, the α -Sn/Si(111) system is a prototype system for a metal-insulator transition at $T_c \approx 70$ K (cf. chapter 6) [66]. Therefore, this phase is suitable to probe finite-size effects for a surface Mott system. As shown in Figs. 7.7 (a) and (b) energy distribution curves (EDC) were taken at two different points in k -space at 40 K. Along the $[1\bar{1}0]$ -direction, the spectral weight at E_F is strongly suppressed for both the flat and the vicinal surface. On the other hand, whereas along the $[11\bar{2}]$ -direction the surface state on the flat surface shows a clear Mott gap, a considerable intensity is found at E_F for the same state on the vicinal surface. The band maps, which correspond to the EDCs, are shown in Figs. 6.10 (c) and (d), as well as curvature plots ((e) and (f)). The latter shows the dispersion of the surface state in more detail. The calculated band structure of α -Sn/Si(111) [205] is superimposed in order to highlight the alteration of the surface state in case of the vicinal substrate, especially in the $[11\bar{2}]$ -direction. Furthermore, the intensity of the Sn/Si(557) surface state appears to be weaker than for Sn/Si(111). Since a lack of sample quality is excluded by means of LEED, which was done prior to the ARPES measurements,

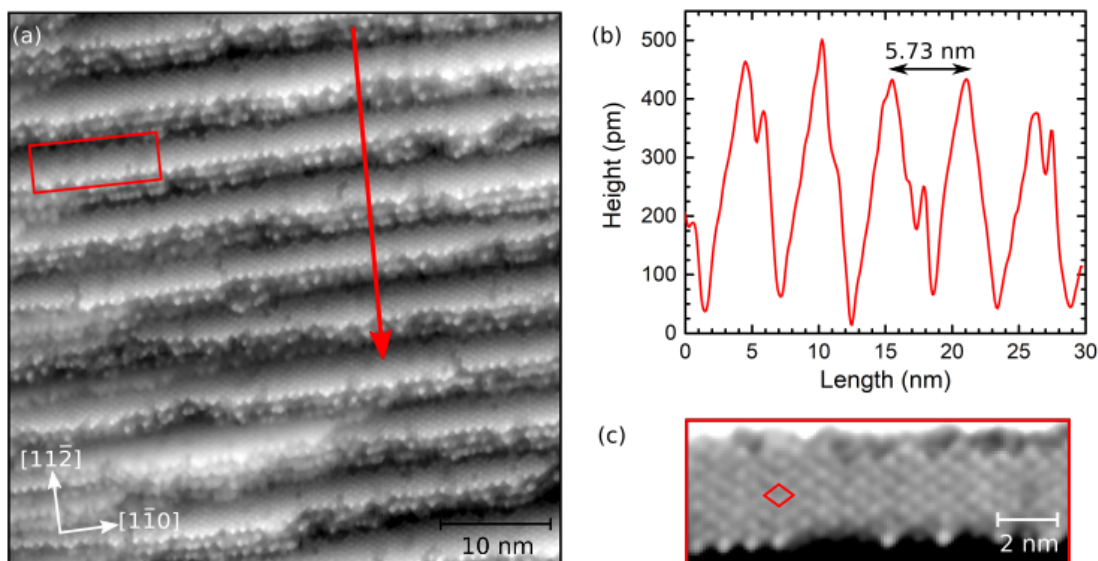


Figure 7.6: (a) STM image of the 0.4 ML Sn phase on Si(557). Red arrow indicates the direction of the linescan shown in (b). (c) Enlarged image of the $(\sqrt{3} \times \sqrt{3})$ structure on the terraces. The unit cell is indicated in red. Images were taken at ($V = 1$ V, $I = 1$ nA)

the decrease in intensity is attributed to the confined size of the α -Sn reconstruction, and the presence of stepped areas in between. Apparently, the Sn/Si(557) system in this coverage regime resembles a pseudo-gapped Mott state.

7.2 Summary and conclusion

In summary, the growth of Sn on Si(557) substrates was studied in detail. In total, three different stable phases were identified. For coverages needed to form the α -Sn phase on Si(111), the initial surface facet structure is maintained. Increasing of the Sn coverage leads to $(2\sqrt{3} \times 2\sqrt{3})$ domains, that tend to develop on large (111) terraces. That first results in locally (223) oriented parts separated by wider (111) terraces, and eventually, the whole surface is covered with (111) terraces due to step bunching.

For coverages of 0.4 ML Sn, a homogeneously stepped array of α -Sn nanowires is found. ARPES measurements on this phase below T_c for the Mott transition on Sn/Si(111) clearly showed a metallic surface state in the direction across the nanowires. As introduced in chapter 2.1.3, Ming et al. [46] succeeded in doping the α -Sn/Si(111) phase via changing the substrate's doping level. Upon hole doping, STS measurements show the development of a quasi-particle state inside the Mott-insulating gap of the system. In the case considered here, doping might be induced via step edges. As already known for Ag/Si(557), excess atoms adsorbed on step edges leads to electron-doping of the system. Along the step edges of these Sn nanowires, silicon dimers are present as well as Sn atoms. This may lead to an additional state close to E_F , which is seen in ARPES in superposition with the insulating state originating from the α -Sn phase.

Alternatively, the finite width of the α -Sn nanowires should be considered, which is com-

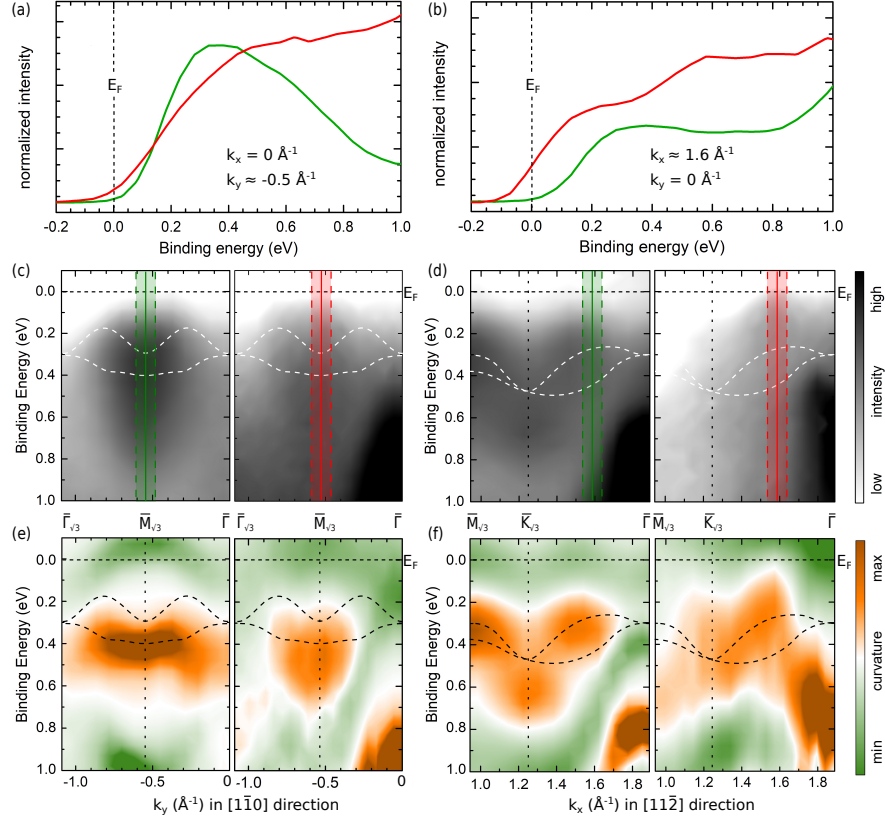


Figure 7.7: (a), (b) EDCs for surface states along the $[\bar{1}\bar{1}0]$ -direction (at $k_y \approx -0.5 \text{ \AA}^{-1}$, $k_x = 0 \text{ \AA}^{-1}$) and $[\bar{1}\bar{1}\bar{2}]$ -direction (at $k_x \approx 1.6 \text{ \AA}^{-1}$, $k_y = 0 \text{ \AA}^{-1}$), respectively. Red lines correspond to low coverage Sn/Si(557) nanowires, green lines are from α -Sn/Si(111) and are shown for comparison. c) Band maps of the Mott-state along the $[\bar{1}\bar{1}0]$ -direction for α -Sn phase on Si(111) (left, 90 eV photon energy, 40 K) and Si(557) (right, 44 eV photon energy, 40 K). d) Band maps like in panel c) but along the $[\bar{1}\bar{1}\bar{2}]$ -direction. (e), (f) Curvature maps of (c) and (d) to highlight details of the band structure. The Sn/Si(111) data were reproduced from data shown in Ref. [182]. The dashed lines refer to band structure calculations for Sn/Si(111) [182, 205].

parable to the coherence length of the Mott state which can be approximately calculated via $\xi = 2\hbar v_F / \pi \Delta$, where Δ is the energy gap and v_F the Fermi velocity of the electrons [220]. From the ARPES data $\xi \approx 2 - 3 \text{ nm}$ can be estimated; thus the finite width along the $[\bar{1}\bar{1}\bar{2}]$ -direction quenches the Mott state in this direction resulting in a pseudo-gapped Mott state in α -Sn nanowires.

Pb nanowires on a vicinal silicon substrate

Pb structures with coverages of 1.3 ML grown on vicinal silicon substrates have attracted much interest during the last decades as they host peculiar spin properties. For instance, Pb/Si(553) was reported to arrange in a well-ordered nanowire array, which electronically has a purely 1D character with metallic surface states showing a giant Rashba-type spin-orbit splitting [221–223]. The Pb/Si(557) system presented here exhibits a peculiar inherent instability. Growing Pb structures close to the desorption temperature of Pb, i.e., 330 °C, leads to a local refacetting of the surface. Depending on the exact Pb coverage in the range of 1.2 and 1.6 ML, various differently oriented facets are observable, e.g. (112), (335), or (223) [216]. The deviation from the overall (557) orientation is compensated by wider (111) terraces, or non-periodic step bunches.

In the case of the particular Pb coverage of 1.3 ML, the surface undergoes a refacetting to a local (223) orientation. The resulting (223) mini-terraces have a width of $4\frac{2}{3} a_{\text{Si}} = 1.55$ nm, with $a_{\text{Si}} = 0.332$ nm being the Si lattice constant in $[\bar{1}\bar{1}2]$ direction. It corresponds to a spot splitting of $\Delta k_y = 21.3$ %SBZ seen in the SPALEED pattern displayed in Fig. 8.1 (a) [216]. On top of the terraces, the Pb atoms are supposed to arrange in a densely packed $(\sqrt{3} \times \sqrt{3})R30^\circ$ reconstruction with four Pb atoms per unit cell [43]. Despite the existence of several STM images published in literature, e.g. [41, 43], actual high resolution images revealing the exact atomic positions are still missing up to date.

Interestingly, the system reversely switches between 1D and 2D properties by the change of temperature. Below a critical value of $T_c \approx 78$ K, a 1D metallic state with high conductance is present along the nanowires, while it is insulating in the direction perpendicular to them. The conductance anisotropy is drastically reduced for higher temperatures, as depicted in Fig. 8.1 (b) [42–44]. This one-directional metal-insulator transition is explained by the formation of a SODW introduced in chapter 2.3, due to a delicate interplay between SOC and electronic correlations strength of the system [103, 107]. The quite exotic insulating state is robust even upon adding small amounts of excess Pb coverage onto the surface, as proved by the preservation of the spin order of the system [41]. Indeed, the excess coverage tends to decorate the step edges, instead of random adsorption on top of the terraces. Several different periodicities up to a length of six times the terrace width were reported from SPALEED investigations [45]. In the course of this, a decoration of every second step edge is achieved for $\delta\theta = 0.1$ ML, and consequently, all edges are covered for $\delta\theta = 0.2$ ML. However, the

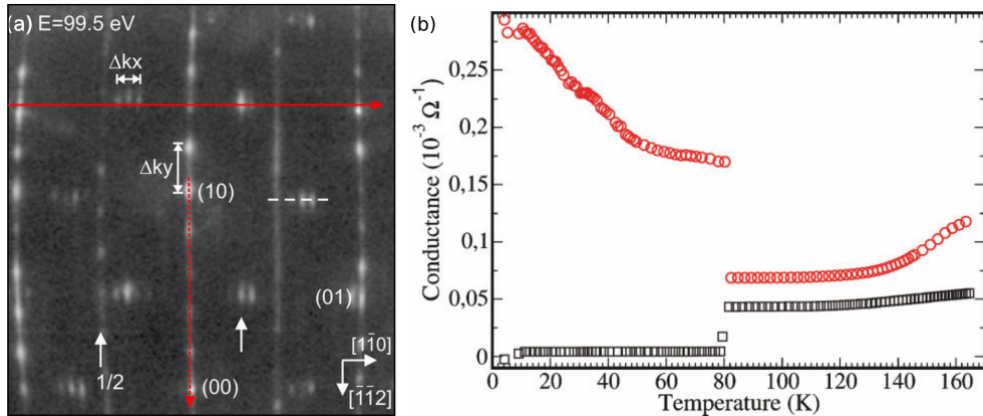


Figure 8.1: (a) SPALEED pattern taken from Ref. [216]. The red arrows indicate the directions of the linescan shown in Fig. 8.6. (b) Conductance as a function of temperature from Ref. [42, 44] of ~ 1.3 ML Pb on Si(557). For the data points marked by red circles (black squares), conductance was measured along the $[110]$ ($[\bar{1}\bar{1}2]$) direction, that is parallel (perpendicular) to the nanowires.

particular adsorption site along the edges has not been determined so far.

Within the scope of this chapter, new insights in both structural and electronic properties are introduced. The measurements presented in the following were carried out by using the LT-STM as described in chapter 4.1.2. Three different temperatures were chosen for operation, i.e., RT, 80 K, and 6 K, in order to acquire data above and below T_c . For the latter two temperatures, LN₂ or LHe served as coolant.

Samples were prepared using degassed and flash-annealed phosphorous-doped Si(557) substrates ($\rho < 5$ m Ω cm) as a template, clearly showing both (7×7) reconstruction and a step-train pattern in optical LEED. For nanowire growth, Pb was evaporated employing a two-step recipe. First, 2 ML Pb was applied with the substrate held at 330 °C, afterward, the substrate temperature was lowered to 300 °C for deposition of additional 1.5 ML Pb. During the first step, the Pb atoms do not stick to the surface due to the elevated temperature, but rather bombard it in order to destroy the Si- (7×7) reconstruction. This leads to a destabilization of the triple steps and induces obviously a refacetting to a single-stepped surface, which is stabilized by Pb adsorption throughout the second stage of the recipe. The resulting total coverage is approximately 1.3 ML. The nanowires may be tuned by adding additional Pb up to an excess coverage of $\delta\theta = 0.2$ ML. In this case, a wide range of substrate temperatures is applicable, i.e., the arising structure remains the same for sample temperatures between 80 K and RT, due to the high mobility of Pb atoms even at low temperatures.

8.1 Structural properties

As already pointed out in the introduction of this chapter, it is well-known that the preparation of the Pb/Si(557) system with a Pb coverage of about 1.3 ML leads to a refacetting of the surface. The arising reconstruction consists mainly of single-stepped (223) oriented parts separated by a minority phase of wider (111) terraces, which compensate the deviation to the overall (557) orientation. This is observable by means of STM, as displayed in Fig.

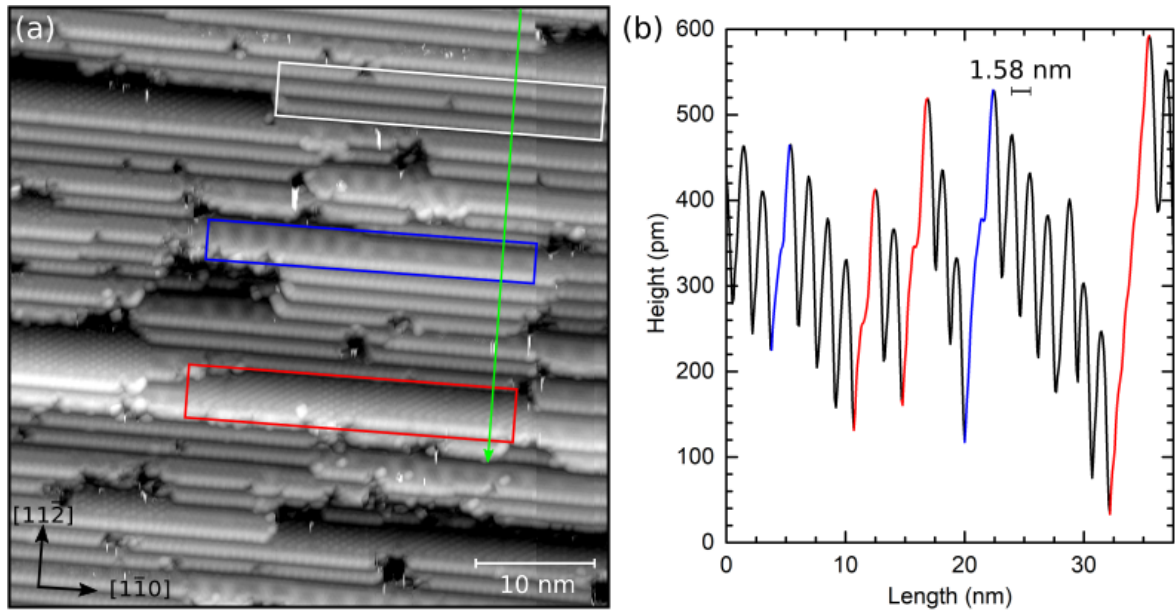


Figure 8.2: (a) Overview STM image of the Pb/Si(557) surface, showing (223) oriented nanowires separated by wider (111) terraces (tunneling conditions: $U = -1$ V, $I = 0.5$ nA, $T = 80$ K). Exemplarily, an area with nanowires is marked by the white rectangle, as well as two different Pb reconstructions namely SIC and a modulated Pb- $\sqrt{3}$ phase in red or blue, respectively. (b) Linescans along the direction indicated by the green arrow in (a). (223) oriented parts are drawn in black; the color of the (111) terraces correspond to their Pb reconstruction (cf. panel (a)).

8.2(a). The linescan taken in the direction perpendicular to the step edges (see Fig. 8.2(b)) clearly shows the two local orientations as well as the distance of 1.58 nm between adjacent nanowires. In order to model the atomic structure of the nanowires present on the (223) facets in the following (chapter 8.1.2), it is focused first on the (111) terraces. Although it is the minority on this surface, their structural model is easier to deduce from the STM images owing to their larger individual size, and the structure of the nanowires can be derived based on it afterward.

8.1.1 Pb phases on (111) terraces

Apparently, at this coverage two different structures coexist on the larger (111) terraces, which can be distinguished even in large-scale images (cf. Fig. 8.2(a) or Ref. [219, 224]). On the one hand, a rather flat reconstruction, and on the other hand a phase that exhibits a modulation which causes pronounced stripes. Considering the phase diagram of Pb/Si(111) [225], the so-called striped incommensurate phase (SIC) is found for Pb coverages of $\theta = 4/3$ ML. It comprises Pb tetramers arranged in a $(\sqrt{3} \times \sqrt{3})$ reconstruction. The tetramer's central atom can be either located above a hollow site of the topmost Si honeycomb (H_3), or on top of a Si atom of the second Si layer (T_4), while the surrounding three atoms occupy off-centered positions above a Si atom of the first Si layer (T_1) [226, 227]. These two adsorption geometries are energetically almost identical and thus similarly often occupied [227, 228]. This gives rise

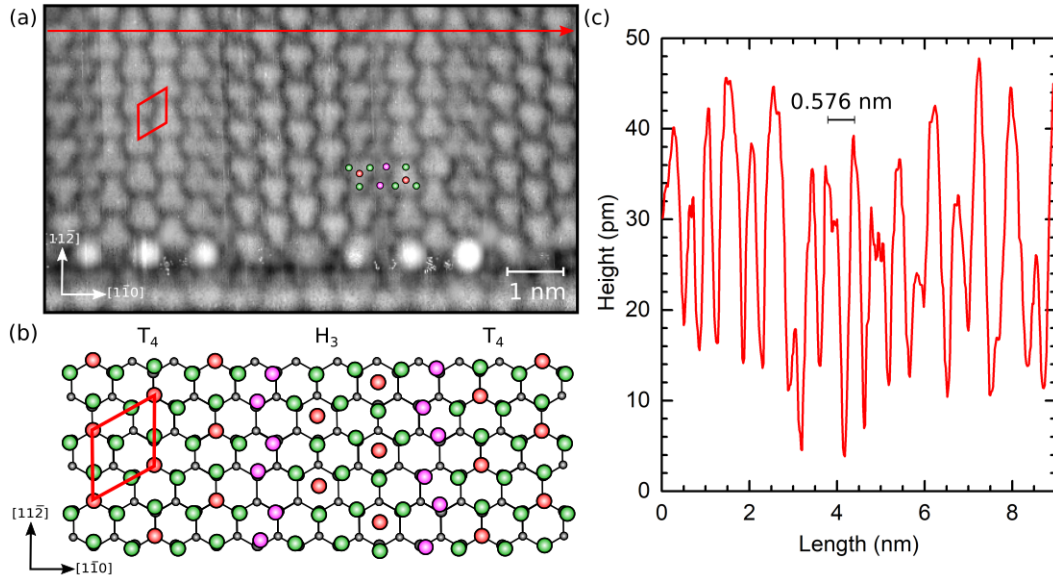


Figure 8.3: (a) STM image of a wider (111) terrace featuring the SIC phase ($U = -0.5$ V, $I = 0.5$ nA, $T = 80$ K). The $(\sqrt{3} \times \sqrt{3})$ unit cell is highlighted in red. A step edge is located at the bottom edge of the picture. The dashed arrow indicates a distance of $3a_{\text{Si}} = 1.152$ nm parallel to the step edge. (b) Top-view structural model of the SIC phase. It consists of tetramers composed of one central atom (red) and three surrounding atoms (green), arranged in a $(\sqrt{3} \times \sqrt{3})$ reconstruction. The central atom of these tetramers is located either at the T_4 or H_3 adsorption site, while the surrounding atoms occupy off-centered T_1 positions. These domains may vary in size and are separated by quasi- $(\sqrt{7} \times \sqrt{3})$ domain walls (indicated in pink) [226, 227, 229].

to the formation of domains, which are separated by quasi- $(\sqrt{7} \times \sqrt{3})$ domain walls [225, 229]. As the domain walls have a slightly lower Pb density than the Pb- $(\sqrt{3} \times \sqrt{3})$ tetramers, the actual Pb coverage of the SIC phase is about 1.3 ML [228].

Indeed, the SIC phase is present on most of the larger (111) terraces of Pb/Si(557). Fig. 8.3(a) shows a STM image of such an area. Due to the finite size of the terraces, one of the three possible rotational domains is favored, i.e., in order to maximize the domain size, the domain walls run perpendicular to the step edge. The corresponding structural model is depicted in Fig. 8.3(b). Like for the Pb/Si(111) SIC phase, the $(\sqrt{3} \times \sqrt{3})$ reconstruction consists of Pb tetramers, and the T_4 and H_3 domains are separated by quasi- $(\sqrt{7} \times \sqrt{3})$ domain walls. In STM, these tetramers appear as triangular patterns, since the central atom appears lower than the surrounding three Pb atoms due to its adsorption site [143]. Hence, the linescan in Fig. 8.3(c) displays a periodicity of $\sqrt{3}a_{\text{Si}} \cos(30^\circ) = 0.576$ nm instead of around $a_{\text{Si}} = 0.384$ nm, as expected from the structural model.

The second phase observed on the (111) terraces is depicted in Fig. 8.4(a). The STM picture shows a terrace that varies in width. To the right side, it is larger and several $(\sqrt{3} \times \sqrt{3})$ unit cells of the SIC phase can be identified. They were used for calibration of the underlying silicon lattice in order to construct a structural model of the second phase. The second phase itself exhibits an atomically resolved structure that appears to be modulated in height. A linescan in Fig. 8.4(b) determines the length of the modulation to about 2.4 nm.

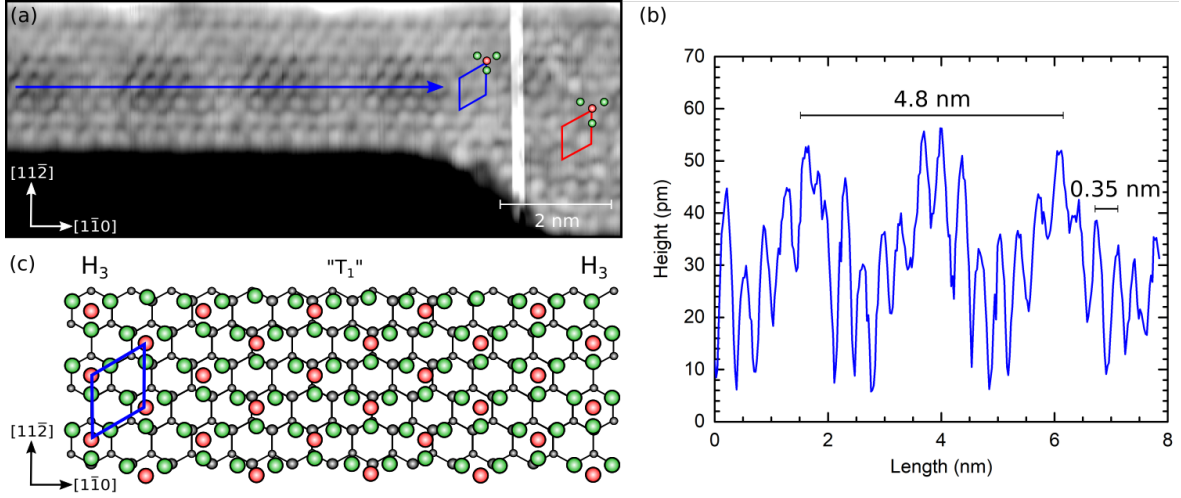


Figure 8.4: (a) STM image of a wider (111) terrace featuring the modulated $\text{Pb-}\sqrt{3}$ phase ($U = -1$ V, $I = 0.5$ nA, $T = 6$ K). Towards the right side the terrace width increases giving rise to a H_3 SIC domain. The unit cells of both phases are highlighted in red and blue, respectively. The blue arrow illustrates the domain size of the dense $\text{Pb-}\sqrt{3}$ structure. The vertical white line is a tip artifact. (b) Linescan along the terrace, highlighting the modulation present on it. (c) Top-view structural model of the modulated $\text{Pb-}\sqrt{3}$ phase. It is made of tetramers roughly arranged in a $(\sqrt{3} \times \sqrt{3})$ reconstruction, which is compressed in $[1\bar{1}0]$ direction. The domain size is $12.5a_{\text{Si}} = 4.80$ nm.

Actually, the actual size of the Pb superstructure unit cell is doubled in size. For modeling of the atomic structure, a close resemblance to the SIC phase was assumed, i.e., it consists of tetramers which appear as triangular patterns. This seems to be reasonable as it results in a Pb coverage only slightly higher than the SIC phase, but differs from a previously suggested quasi- (1×1) reconstruction for structures with a similar appearance in STM emerging at domain boundary intersections of SIC-Pb/Si(111) [230]. However, for the latter, a trimer structure and thus a lower coverage of only 1 ML Pb for the SIC phase was supposed.

In contrast to the SIC phase, for the modulated Pb phase, the spacing between adjacent tetramers is less, resulting in a more densely packed structure. Hence the adsorption sites of the tetramers differ which gives rise to the observable superstructure with a unit cell length of $12.5a_{\text{Si}} = 4.80$ nm (cf. Fig. 8.4(c)). The doubling of the supercell length compared to the modulation seen in the linescan is due to energetically similar adsorption sites. For central atoms adsorbed either at H_3 or at bridge positions between T_1 and T_4 , the structure appears to be higher in STM, whereas all other tetramers are darker in contrast.

On the Pb/Si(557) surface, both phases present on the (111) terraces are not distributed equally. The majority is covered by the SIC phase, whereas the modulated Pb phase only develops on terraces with a width of approximately 3 nm. Furthermore, the distances between maxima of the modulation vary around 2 and 2.4 nm [224]. This leads to the conclusion that the modulated phase is not limited to a specific value of Pb coverage but rather exists in a certain range of $\theta \approx 1.44 - 1.46$ ML due to variable spacings between the Pb tetramers. As the SIC phase comprises 1.3 ML, any higher Pb coverage present on the surface may be compensated by the development of modulated phase domains.

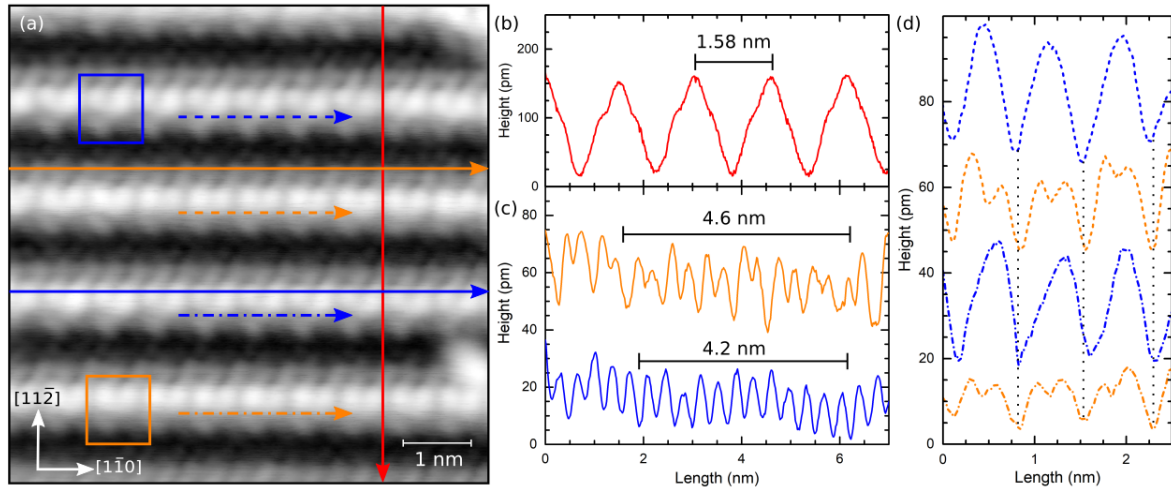


Figure 8.5: (a) High resolution STM image of the (223) faceted part showing four Pb nanowires ($U = 0.5$ V, $I = 0.3$ nA, $T = 6$ K). The arrangement of Pb atoms differs at the step edges, resulting in two different arrangements of bright protrusions (marked by orange and blue rectangles). These two configurations are alternately present on every second step edge. (b) Linescan perpendicular to the nanowires (red arrow in (a)) showing the distance of 1.58 nm between adjacent step edges. (c) Linescans along two nanowires with different step edge configuration (solid orange and blue arrows in (a)) showing a modulation of 4.6 nm and 4.2 nm. (d) Linescans highlight the two different step edge configurations (dashed/ dashed-dotted orange and blue arrows marked in (a)). Dotted black lines point out the strong correlation between adjacent chains.

8.1.2 Nanowires on (223) facets

The Pb nanowire-like structure that will be discussed in this section arises on the (223) faceted parts that are enclosed by the wider (111) terraces. In order to highlight the structural change triggered by small amounts of Pb excess coverage, measurements were done on samples with additional $\delta\theta \approx 0.1$ ML Pb adsorbed at RT after the execution of the standard two-step recipe for Pb nanowire growth, as already described in the introduction of this chapter.

An atomically resolved STM image of four of the nanowires is shown in Fig. 8.5 (a). The spacing of 1.58 nm between adjacent step edges is consistent with the local (223) orientation (see Fig. 8.5 (b)), while the mini-terrace itself has a width of $4\frac{2}{3}a_{\text{Si}} = 1.55$ nm [43, 216]. Strikingly, the arrangement of Pb atoms differs at the step edges, appearing as two different arrangements of bright protrusions in STM. Linescans taken directly along the step edges (see Fig. 8.5 (d)) show either a double peak structure or single peaks. The periodicity of both is approximately 0.70 nm, which is smaller than $2a_{\text{Si}} = 0.768$ nm expected for dimerized Si bonds. Furthermore, adjacent step edge configurations are in-phase, pointing towards a strong interchain coupling. These two configurations are alternately occurring on every second step edge, just as it was concluded previously from the appearance of extra diffraction spots in SPALeED measurements taken along the $[\bar{1}\bar{1}2]$ direction, i.e., perpendicular to the nanowires [216]. It will be shown in the following that the Pb excess coverage accumulates at the mini-terraces with double-peaked step edges, while the terraces with single protrusions are covered by the initially deposited 1.3 ML Pb.

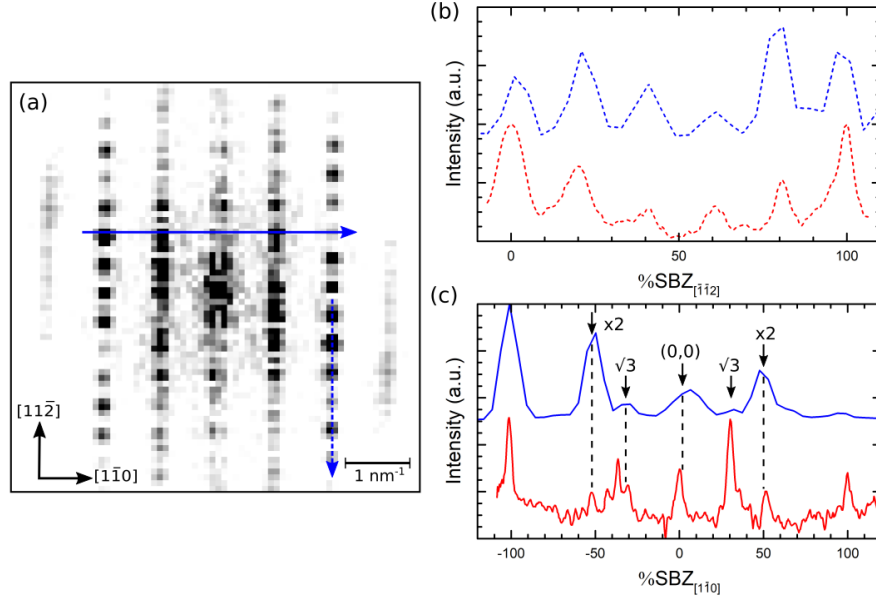


Figure 8.6: (a) FFT of the STM image in Fig. 8.5 (a). Linescans along (b) the $[\bar{1}\bar{1}2]$ and (c) the $[\bar{1}\bar{1}0]$ direction are indicated with blue arrows. For comparison, linescans taken along the same directions in Fig. 8.1 (a) are shown in red. In (c), arrows indicate the positions of the $\sqrt{3}$, $\times 2$ and $(0,0)$ diffraction spots.

In Fig. 8.5 (c), linescans taken in $[\bar{1}\bar{1}0]$ direction parallel to the nanowires are displayed. They highlight a vertical modulation of the atomic structure present on terraces both with and without Pb excess coverage. Considering different mini-(111) terraces, the modulation length varies slightly being 4.6 nm or 4.2 nm for nanowires with or without additional Pb, respectively. Noticeable, both lengths are roughly multiples of the silicon lattice constant, namely $12a_{\text{Si}}$ or $11a_{\text{Si}}$. In previous publications on Pb/Si(557), STM images always revealed a constant modulation length of $10a_{\text{Si}}$ [43, 216]. However, from SPALEED data measuring the spot splitting of the $\sqrt{3}$ diffraction spot, it was already deduced that tiny amounts of Pb excess coverage do not only decorate the step edges but simultaneously alter the wavelength along the terraces [216]. For instance, for coverages between 1.30 and 1.314 ML, the modulation length varies from $7a_{\text{Si}}$ to $12a_{\text{Si}}$, which corresponds to the (1,3) and (1,6) phase in terms of the devil's staircase phases [216]. Hence, the wavelengths of $12a_{\text{Si}}$ and $11a_{\text{Si}}$ already point towards a modification of the structure due to the adsorbed 0.1 ML of excess Pb.

In order to model the actual atomic structure of the nanowires, first a fast Fourier transformation (FFT) of the STM image shown in Fig. 8.5 (a) was done (see Fig. 8.6 (a)). Along the $[\bar{1}\bar{1}2]$ direction (cf. Fig. 8.6 (b)), the spot splitting represents the step distance of 1.58 nm, which is in accordance with the SPALEED image of Pb/Si(557) (see Fig. 8.1 (a)), but any extra diffraction spots due to the excess coverage cannot be resolved due to the small size of the transformed STM image. Furthermore, a linescan along the $[\bar{1}\bar{1}0]$ direction (see Fig. 8.6 (c)) reveals a faint intensity of the $\sqrt{3}$ diffraction spots. It indicates an atomic structure similar to the modulated Pb- $\sqrt{3}$ phase observed on the wider (111) terraces. In that case, the triangular patterns originating from the Pb tetramers, which form the $(\sqrt{3} \times \sqrt{3})$, are not as pronounced in STM as for the SIC phase.

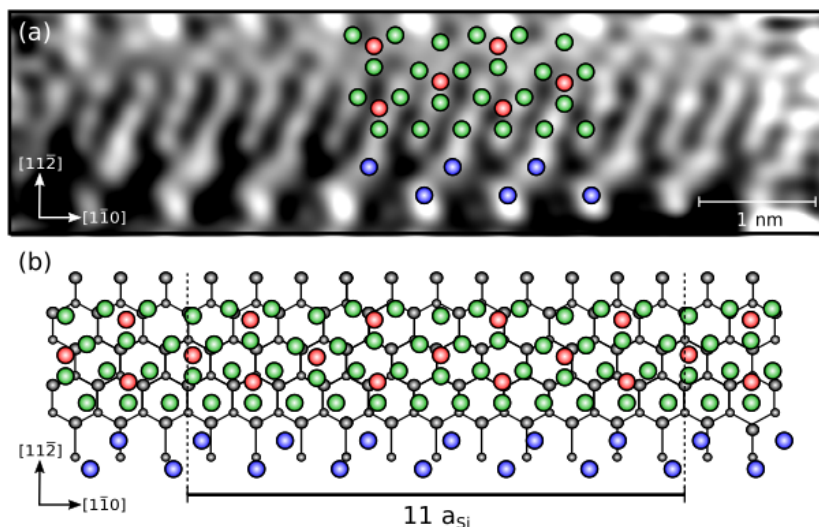


Figure 8.7: (a) Enlargement of the nanowire without Pb excess coverage marked with the blue arrow in Fig. 8.5 (a) ($U = 0.5$ V, $I = 0.3$ nA, $T = 6$ K). Contrast enhancement was done by aligning the height of the lines in the STM picture. (b) Top-view structural model of the (223) facet. On the mini-terrace is a dense Pb- $\sqrt{3}$ phase, consisting of tetramers marked by red and green circles, with a modulation of $11a_{\text{Si}} = 4.22$ nm. Blue circles denote Pb atoms arranged in two rows along the step edge with a periodicity of 0.70 nm each. Parts of this model are superimposed on (a) to highlight their good agreement.

Moreover, parts of the STM image shown in Fig. 8.5 (a) were contrast enhanced by aligning the height of the lines. The resulting image for a mini-terrace without Pb excess coverage is displayed in Fig. 8.7 (a). For creating the structural model, a similar approach was chosen as for the modulated Pb phase on larger (111) terraces (cf. chapter 8.1.1), as implied by the FFT. First of all, the underlying silicon lattice was calibrated using a zoomed out picture at the same position as Fig. 8.5 (a), but also showing a larger (111) terrace featuring the SIC phase. The Pb atoms on top were arranged as tetramers that form a compressed ($\sqrt{3} \times \sqrt{3}$) reconstruction to fit the observed pattern. Although the central atom of the tetramers still remains hidden, it is a suitable approach as the $\sqrt{3}$ diffraction spot is split due to varying modulation lengths [216]. Like on the (111) terraces, the modulation of $11a_{\text{Si}} = 4.22$ nm is caused by different adsorption sites occupied by the tetramers. In this case, the compression of the Pb structure does not only occur along the terrace but in $[1\bar{1}0]$ direction as well. Hence, the bridge site positions in between T_1 and T_4 are not exactly met but rather shifted to T_1 . Since the appearance in STM of tetramers having this position differs from H_3 occupied sites, the linescan resembles the actual modulation present on the mini-terrace.

Concerning the step edges, it has been previously assumed [216], that for terraces without Pb excess coverage dimerized silicon bonds remain present at step edges. Indeed, a periodicity of roughly $2a_{\text{Si}}$ is observed at the step edges, but it is modulated in the same fashion as the $\sqrt{3}$ reconstruction on top of the mini-terraces. Hence this leads to the conclusion that these features are rather due to two rows of Pb atoms. They decorate the step edge as drawn in Fig. 8.7 (b), which results in its earlier mentioned single-peaked features seen in the linescan (cf. Fig. 8.5 (d)).

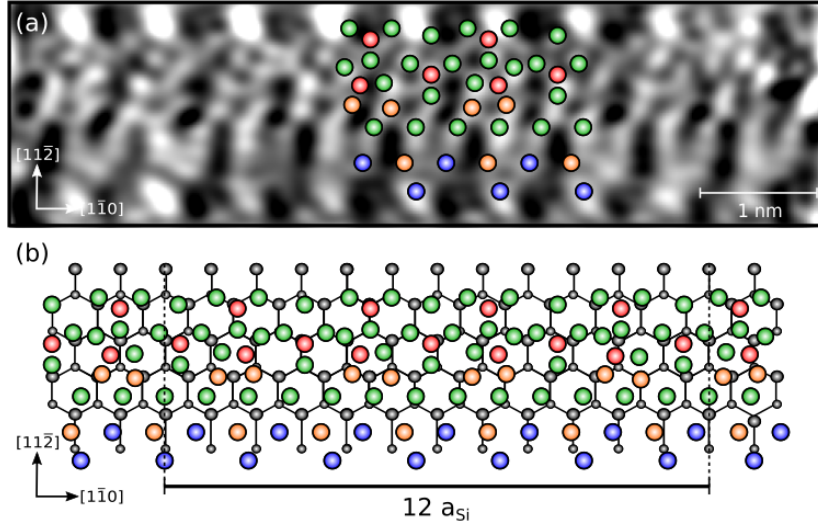


Figure 8.8: (a) Enlargement of the nanowire with Pb excess coverage marked with the orange arrow in Fig. 8.5 (a) ($U = 0.5$ V, $I = 0.3$ nA, $T = 6$ K). Contrast enhancement was done by aligning the height of the lines in the STM picture. (b) Top-view structural model of the (223) facet. On the mini-terrace is a dense Pb- $\sqrt{3}$ phase, consisting of tetramers marked by red and green circles, with a modulation of $12a_{\text{Si}} = 4.61$ nm. Unlike in Fig. 8.7 (b), additional 0.2 ML Pb excess coverage (orange circles) are present, leading to a tilting of some of the tetramers. Along the step edge, the upper chain of Pb atoms (blue circles) is now completely filled, showing a periodicity of slightly less than a_{Si} . Parts of this model are superimposed on (a) to highlight their good agreement.

The same procedure has been carried out to establish a structural model of the terraces covered with excess Pb. The corresponding contrast-enhanced STM image, as well as the resulting model, is shown in Fig. 8.8. In this case, the modulation length of the compressed Pb phase along the terrace is determined to be $12a_{\text{Si}} = 4.61$ nm. Compared to the structure without Pb excess, the unit cell of the Pb reconstruction is a bit larger, like it is expected from the shrinking of the $\sqrt{3}$ diffraction spot-splitting observed for higher coverages [216].

Structurally, two prominent modifications occur. On the step edge, the upper chain of Pb atoms is now completely filled, which changes its periodicity to slightly less than $1a_{\text{Si}}$, and leads to the double-peaked protrusions along the edge. Furthermore, an additional row of Pb atoms is adsorbed on top of the mini-terraces. Since the $(\sqrt{3} \times \sqrt{3})$ reconstruction on these terraces is already quite densely packed even without excess Pb, the additional Pb row induces a tilting of the adjacent row of tetramers. Taking into account the amount of excess Pb atoms on this terraces (marked with orange circles in Fig. 8.8 (b)), a total coverage change of approximately $\delta\theta \approx 0.2$ ML compared to the previously discussed terrace (cf. Fig. 8.7) is calculated. Since the excess Pb atoms accumulate on every second terrace, an overall coverage of $\delta\theta = 0.1$ ML is present on the (223) faceted part of the surface.

In order to highlight the small differences between the nanowires without and with Pb excess coverage, both of their STM images are partly superimposed by the structural models and displayed in Fig. 8.9. Arrows mark exemplarily the positions of one row of Pb atoms in the direction across the wire. Thus, both the additional Pb row on the mini-terrace as well

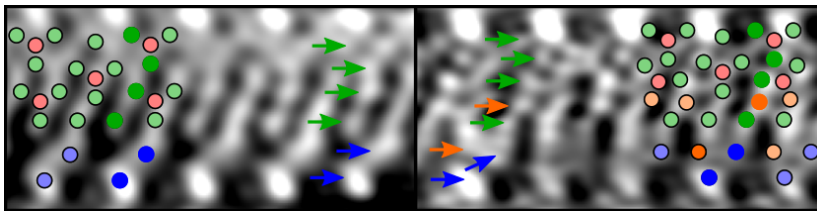


Figure 8.9: Comparison of the nanowires without (left) and with (right) Pb excess coverage ($U = 0.5$ V, $I = 0.3$ nA, $T = 6$ K, cf. Figs. 8.7 and 8.8). Parts of the corresponding structural models are superimposed. Arrows mark similar positions as the highly colored circles of the structural models to highlight the differences between both nanowire types. Pb excess atoms are drawn in orange.

as the filling of the upper Pb chain along the step edge can be clearly identified.

8.2 Electronic properties

In the scope of this work, the electronic structure was probed by means of STS. In Fig. 8.10 (a), $I(V)$ spectra are shown, taken either on the (223) faceted parts covered by 1.3 ML Pb nanowires, or on the wider (111) terraces with a SIC reconstruction on top. All spectra are averaged over several curves measured at multiple positions on the sample. The results for two temperatures, 6 K and 80 K, are plotted in order to allow a comparison between the electronic properties below and above the phase transition. In this connection, it is noteworthy, that despite a measured temperature value close to the phase transition temperature of 78 K, the samples are still in the high-temperature phase. This was ensured by comparing the data with spectra taken well above T_c , i.e., at RT, which had the same shape but showed a strong increase in noise.

According to the $I(V)$ spectra, for $T > T_c$ the nanowires are metallic. Lowering the temperature to $T < T_c$ leads to the opening of a gap and thus a semiconductor-like $I(V)$ curve. For the SIC phase on wider (111) terraces, the $I(V)$ curves at both temperatures follow the same trend as the data acquired on nanowires.

In order to enhance the visibility of states close to E_F , normalized dI/dV curves were calculated by dividing the simultaneously recorded dI/dV data by the fraction I/V . At 80 K, the nanowires show three pronounced states at 25 mV, -20 mV, and -70 mV and a finite zero bias conductance, while for the (111) terraces one sharp peak is visible at 45 mV and two rather broad ones in the vicinity of $V = 0$ and at -50 mV (see Fig. 8.10 (b)). Upon cooling down to 6 K, a gap is opened (see Fig. 8.10 (c)), redistributing the LDOS to higher bias voltages, while the filled states at -70 mV and -50 meV, respectively, remain at the same position. In order to model the BCS-like gap features in Fig. 8.10 (c), Bardeen-Cooper-Schrieffer (BCS) theory [231] and an additional broadening with a linewidth Γ associated with inelastic electron-electron scattering [232] was used,

$$dI/dV \propto \operatorname{Re} \frac{V + i\Gamma}{\sqrt{(V + i\Gamma)^2 - \Delta^2}}. \quad (8.2.1)$$

Albeit this equation is usually used in the context of superconductivity and it does not fit to the entire recorded dI/dV data, it seems adequate since it provides a good description of the

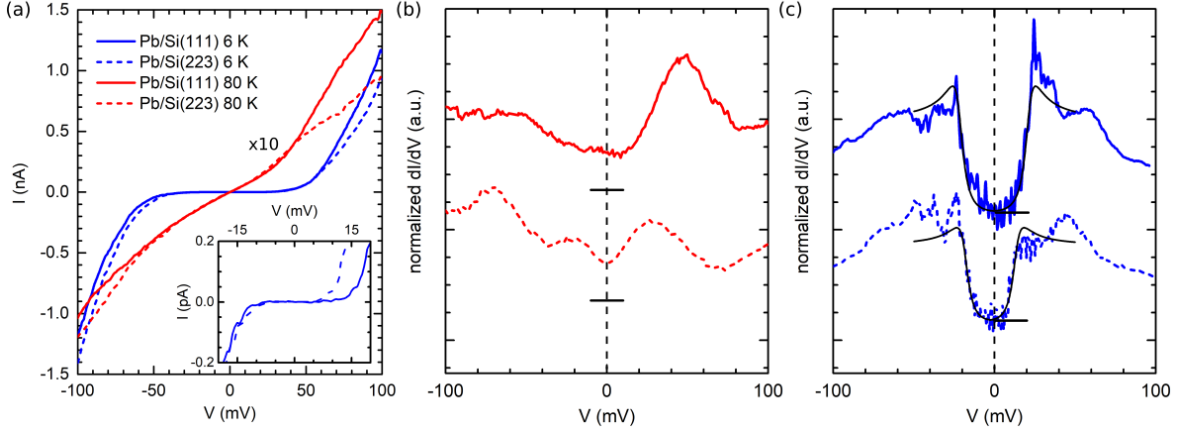


Figure 8.10: (a) Averaged $I(V)$ spectra taken on the SIC-Pb/Si(111) phase (solid lines) and the Pb/Si(223) nanowires (dashed lines). Measurements were done either at 6 K (blue) or at 80 K (red). The latter curves are magnified by a factor of 10. Inset: enlargement of the curves taken at 6 K around $V = 0$. The corresponding normalized dI/dV curves are shown in (b) and (c), shifted vertically for clarity, the horizontal black lines mark the origin for each curve. E_F is highlighted by the vertical black line. In (b) fits of the insulating gap are indicated in black.

insulating gap. It yields a gap size of $2\Delta = (31.8 \pm 0.5)$ mV for the nanowires on the (223) faceted parts, which is in the same order as the gap size $2\Delta \approx 20$ meV previously observed in ARPES in the direction perpendicular to the nanowires. A slightly larger value of $2\Delta = (43.0 \pm 0.4)$ mV is calculated for the (111) terraces, while the linewidth is $\Gamma = (4.5 \pm 0.4)$ mV for both cases.

Besides, using the BCS ratio of 4.4 obtained for the SIC Pb phase on Si(111) [233], the critical temperature of the Pb nanowires yields

$$T_c = \frac{2\Delta}{4.4k_B} \approx 84 \text{ K}, \quad (8.2.2)$$

which is close to the phase transition temperature of 78 K obtained in transport measurements [42, 44].

All in all, the results for the nanowires at higher temperatures are in good agreement with the transport data seen in Fig. 8.1 (b), as well as ARPES data displayed in Figs. 8.11 (a) and (b), which shows a finite intensity at E_F and an increase in intensity upon higher binding energies [112]. However, a significant deviation occurs for $T < T_c$. In contrast to STS, both the transport measurements and ARPES detect contributions originating from the metallic nanowires. The conductance in the direction along the nanowires is reported to increase below T_c [42, 44] and ARPES reveals a small but finite intensity at E_F in addition to an increase in spectral weight a few tenth of an eV away from E_F corresponding to the insulating state seen in STS (cf. Fig. 8.11 (c)) [112].

This apparent contradiction can be solved by taking into account the resolution in k -space of ARPES and STS. The MDCs depicted in Fig. 8.11 (c) were taken along the edge of the SBZ from the Pb/Si(557) nanowire structure [112]. On the other hand, the current measured by means of STS is dominated by electronic states at $\bar{\Gamma}$, i.e., the momentum parallel to

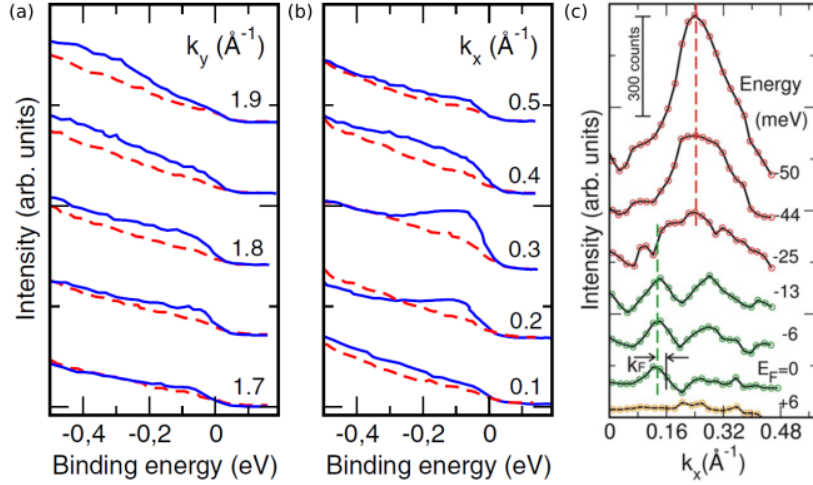


Figure 8.11: EDCs taken along (a) k_y at $k_x = 0 \text{ \AA}^{-1}$ and (b) k_x at $k_y = 1.8 \text{ \AA}^{-1}$ at temperatures of $T = 40 \text{ K}$ (blue line) and $T = 100 \text{ K}$ (red line). (c) Sequence of MDCs along k_x at $k_y = 2.25 \text{ \AA}^{-1}$ at different energies around E_F ($T = 40 \text{ K}$). All images were taken from Ref. [112]

the surface k_{\parallel} is around zero. Only if there are no states available, states with non-zero momentum participate in the tunneling process [120, 234]. This is quantified by a modified inverse decay length of the tunneling current [120, 121, 234]

$$\kappa = \sqrt{\frac{2m}{\hbar^2} \frac{\phi_{\text{tip}} + \phi_{\text{sample}}}{2} - E + \frac{eV}{2} + k_{\parallel}^2}, \quad (8.2.3)$$

which, in contrast to Equation 3.1.3, takes into account k_{\parallel} . Here, ϕ_{tip} and ϕ_{sample} are the workfunctions of tip and sample and E is the energy of the state relative to E_F . Obviously, electrons located at the $\bar{\Gamma}$ points have the smallest value of κ and an increase in k_{\parallel} leads to a reduction in the measured current. Concerning the SBZ shown in Fig. 2.13(d), the insulating state in the direction perpendicular to the nanowires has a parallel momentum of $k_{[\bar{1}\bar{1}0]} = 0.1 \text{ \AA}^{-1}$, while the metallic state closest to $\bar{\Gamma}$ has a momentum of $k_{[11\bar{2}]} = 0.16 \text{ \AA}^{-1}$. In this case, κ is increased by about 20 % for the metallic state at E_F compared to the insulating state located at an energy of $E \approx 20 \text{ meV}$. This leads to a further reduction in intensity of the metallic state in addition to the considerable difference of spectral weight for the metallic states compared to the insulating state seen by ARPES (see Fig. 8.11) [112].

It can be concluded, that the metallic state is not accessible directly at E_F utilizing STS, but it is only detectable if higher bias voltages are applied. At E_F , the tunneling current originating from this state is merely in the order of the noise of the measurements, and thus its contribution cannot be resolved in terms of a finite zero bias voltage. Nevertheless, the non-flat but instead slightly curved gap edges might be on account of the increase in the intensity of the metallic states at small bias voltages.

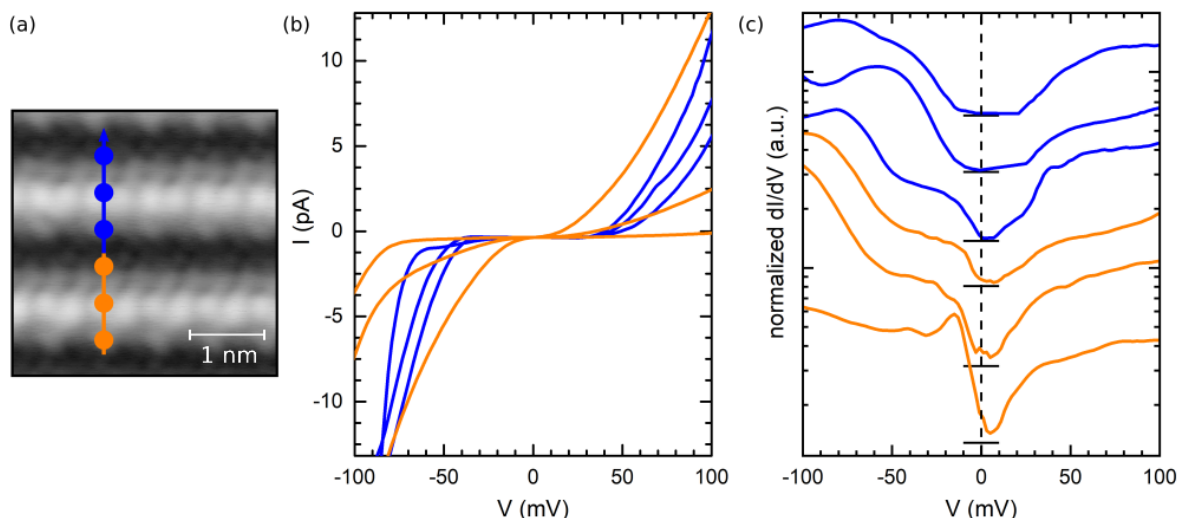


Figure 8.12: (a) High resolution STM image showing two Pb nanowires, the lower one with Pb excess coverage ($U = 0.5$ V, $I = 0.3$ nA, $T = 6$ K). (b) Averaged $I(V)$ spectra taken at different positions as indicated by the dots and the arrow in (a). Curves measured at the wires with (without) Pb excess coverage are drawn in orange (blue). (c) Corresponding normalized dI/dV curves, shifted vertically according to the measurement positions highlighted in (a). The horizontal black lines indicate the origin for each curve and E_F is marked by the dashed black line.

8.2.1 Tunability via Pb excess coverage

So far, the electronic properties of the nanowires were measured only for the case of 1.3 ML Pb coverage, i.e., without additional Pb added to the surface. This raises the question, to what extent Pb excess coverage is able to tune the local density of states of the nanowires. Therefore, spatially resolved STS measurements were performed on terraces with different Pb coverages. In Fig. 8.12 (a), a STM picture of two nanowires is displayed. The upper one is covered by 1.3 ML arranged in the reconstruction shown in Fig. 8.7, while on the lower one a excess Pb coverage of $\delta\theta \approx 0.2$ ML is present (cf. Fig. 8.8). The blue or orange dots indicate the positions STS data was acquired on, at terraces without or with Pb excess coverage, respectively.

The $I(V)$ curves obtained on these positions are plotted in Fig. 8.12 (b). As expected from Fig. 8.10 (a), the blue curves originating from the terrace without Pb excess coverage show a gap. In comparison, an extra amount of Pb atoms added on the mini-terraces indeed changes its electronic properties. This is observable looking at the orange-colored spectra in Fig. 8.12 (b), which clearly show a closing of the gap, resulting in a metallic behavior. More insights are given by normalized dI/dV curves displayed in Fig. 8.12 (c). Regarding the terrace without Pb excess coverage, for the spectra taken on top of the mini-terrace, the insulating gap is in the same order of size as already shown in Fig. 8.10 (c). However, the gap size already decreases for the curve averaged over spectra taken at the step edge in the vicinity of the nanowire with excess Pb. The latter curve even shows a close resemblance to the curves taken on top of the mini-terrace, where additional Pb is present. Here, the local density of states exhibits an additional state close to E_F , which does not exist if only

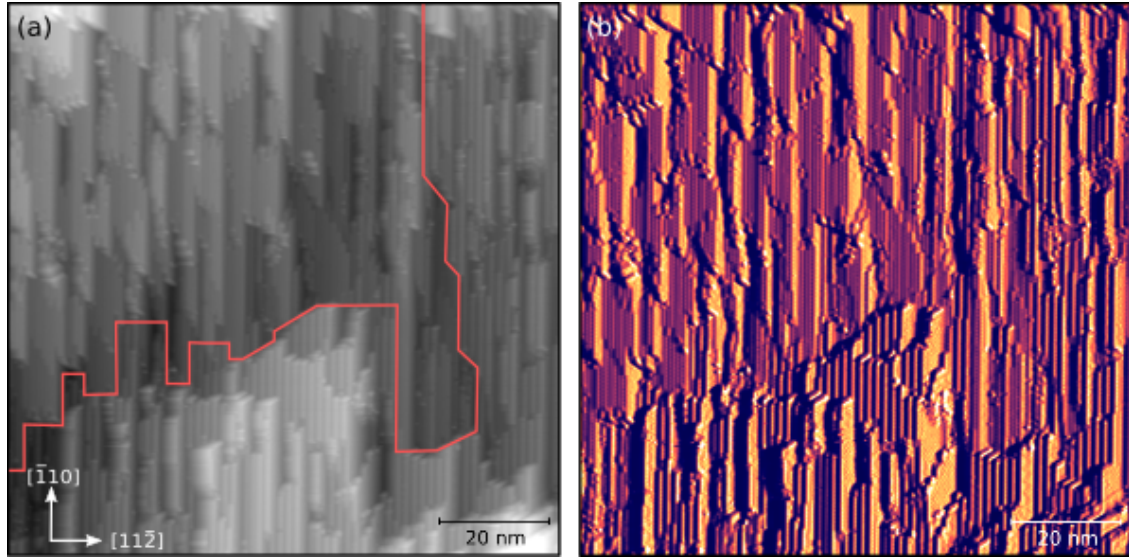


Figure 8.13: (a) Topography and (b) corresponding current images acquired simultaneously by STM ($V = 1$ V, $I = 0.3$ nA, $T = 6$ K). The orange line in (a) marks the boundary between the two phases coexisting on the surface.

nanowires without extra Pb coverage present. At the step edge of the lower terrace, this state gets even more pronounced with its tail crossing E_F . Hence, the additional Pb atoms induce a metallic in-gap state mainly present on the step edge of the terrace they are on. Nevertheless, it is still noticeable on the mini-terrace, and even influencing the electronic properties of the adjacent step edge. This leads to the conclusion that in this case the switching between 1D and 2D conductance at T_c is strongly damped, eventually resulting in a breakdown of the insulating SODW state for surfaces with each terrace covered by $\delta\theta \approx 0.2$ ML, in accordance with previous studies [41, 235].

8.3 High coverage nanowires

During the investigation of Pb nanowires with an extra amount of Pb added to the surface, a second type of nanowires was identified on the surface. Large scale STM images (see Fig. 8.13) show a minority phase coexisting with the previously discussed kind of nanowires on some parts of the sample. In the topographic image, this second phase only appears blurred, while the domains of both phases can be distinguished clearly in the corresponding current image, that was acquired simultaneously during the measurement.

An enlarged area of the second phase is presented in Fig. 8.14 (a). This phase preserves the (223) faceting as seen for the 1.3 ML wires, as the distance between adjacent steps remains at a value of approximately 1.58 nm (cf. 8.14 (b)). However, the STM image shows that the mini-terraces are covered by two rows of bright protrusions, both having a spacing of 0.7 nm. Furthermore, a modulation of ~ 4 nm is still observable along the terraces. This leads to the conclusion that these protrusions are induced by a second layer of Pb atoms that cover the 1.3 ML nanowires. Therefore, they can be considered as high coverage nanowires with $\theta \approx 1.6$ ML.

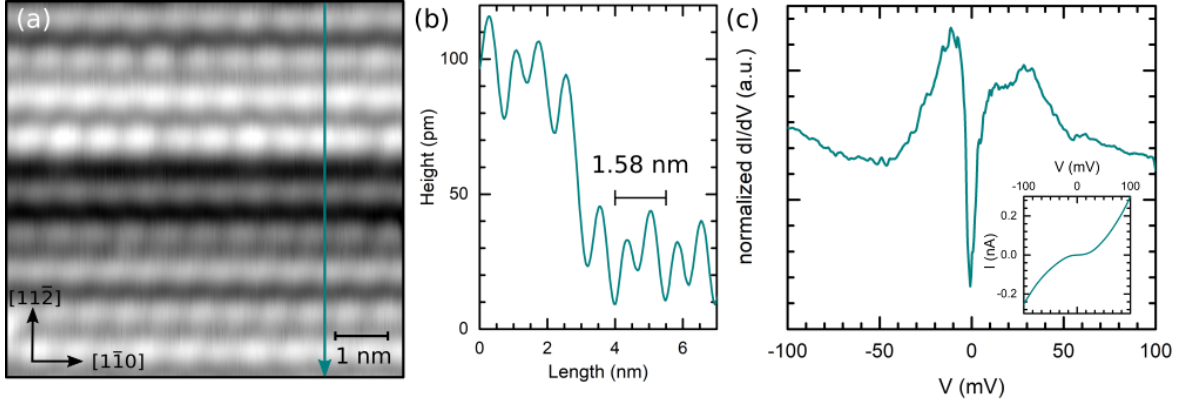


Figure 8.14: (a) STM image of the Pb high coverage nanowires ($V = 1$ V, $I = 0.3$ nA, $T = 6$ K). The arrow indicates the direction of the linescan displayed in (b). (c) Normalized dI/dV spectrum, the corresponding $I(V)$ curve is shown in the inset.

In contrast to the 1.3 ML nanowires, the high coverage nanowires are conducting even at low temperatures. The normalized dI/dV spectrum, which was averaged over several curves taken at different positions along the wires, reveal a finite DOS up to E_F at a temperature of 6 K. This is in accordance with STS measurements presented in chapter 8.2.1, which already deduced that the insulating SODW state breaks down for terraces covered by an excess amount of $\delta\theta = 0.2$ ML Pb.

8.4 Summary and conclusion

In the scope of this chapter, the structural and electronic properties of the Pb/Si(557) surface covered by 1.3 ML Pb were investigated, and the changes on them triggered by the addition of Pb excess coverage. Since the Pb/Si(557) undergoes a refacetting to local (223) faceted nanowire parts separated by wider (111) terraces, both orientations were studied.

On the wider (111) terraces, two different phases were identified. On the one hand, a single-domain SIC-Pb phase similar to the 2D SIC-Pb/Si(111) phase present at coverages around 1.3 ML. On the other hand, a minority phase exists on terraces with a certain width around 3 nm. It comprises of a densely packed ($\sqrt{3} \times \sqrt{3}$) reconstruction that is modulated due to different adsorption sites of the Pb tetramers.

The modulated Pb- $\sqrt{3}$ phase was also observed on top of the (111) mini-terraces of the (223) faceted parts, while Pb atoms at the step edges have roughly a $2a_{Si}$ periodicity. Any Pb excess coverage tended to fill up the Pb row at the step edges, and formed an additional Pb row on top of the mini-terrace, resulting in an even more compressed $\sqrt{3}$ reconstruction. Structural models for both cases were proposed based on high-resolution STM images.

Electronically, on both the nanowires and the wider (111) terraces undergo a metal-insulator transition below 78 K. The resulting band gap has a size of $2\Delta = (31.8 \pm 0.5)$ meV or $2\Delta = (43.0 \pm 0.4)$ meV, respectively. Furthermore, it has been demonstrated that the insulating low-temperature state of the nanowires vanishes if a Pb excess coverage of $\delta\theta \approx 0.2$ ML is added to the nanowires. It can be concluded, that primarily the additional Pb atoms decorating the step edges lead to a breakdown of the SODW in this system. Adding even more Pb

on the surface leads to the formation of domains with high coverage nanowires, which have a second Pb layer on top of the mini-terraces and stay metallic even at low temperatures.

Part III

Conclusion

Summary and outlook

In the scope of this thesis, materials with reduced dimensionalities, such as 2D and quasi-1D systems, were intensively studied with a focus on effects induced by finite size or SOC. This leads to the observation of the spin texture existing in the low-temperature 2D Mott insulating phase of α -Sn/Si(111). For the analysis of quasi-1D systems, metallic atomic nanowires were grown by self-assembly on both flat and vicinal silicon substrates. The main findings concerning the investigated systems will be summarized in the following, and a short outlook regarding future research possibilities will be provided at the end of this chapter.

In/Si(111)-(4 × 1) reconstruction

In the context of quasi-1D atomic nanowires, the In/Si(111)-(4 × 1) reconstruction is one of the most intensively studied systems. Upon cooling below ~ 120 K, it undergoes a Peierls-like metal-insulator phase transition. Due to the doubling of the size both along and across the nanowires, the low-temperature phase structurally exhibits a (8 × 2) unit cell. This phase transition does not occur on a specific temperature value but rather shows a thermal hysteresis behavior, as T_c varies during subsequent heating and cooling cycles [84, 88, 96]. Besides, transport measurements performed on slightly inclined silicon substrates, with 2° miscut towards the $[\bar{1}\bar{1}2]$ direction, already showed a vanishing of the hysteresis of the sheet conductivity due to a shift of the onset temperature of the phase transition upon heating, T_2 , to lower values, while upon cooling the critical temperature remained constant [88].

A detailed investigation of the influence of spatial confinement on the phase transition temperature caused by the presence surface steps was addressed in chapter 5. The surface state conductivity was probed via transport measurements. They indeed confirmed a vanishing of the thermal hysteresis for samples with a high density of steps, i.e., with a miscut of 4° , but additionally displayed a shift of T_1 and T_2 to significantly lower temperatures compared to flat substrates.

It can be concluded that the step edges can affect the phase transition temperature both during cooling and heating. Upon heating, this is explained by the destabilization of the (8 × 2) phase due to the reduction of interchain coupling in the vicinity of the step edge, which is observable even for a low number of steps present on the surface [88]. Since during cooling the low-temperature phase nucleates inside the (4 × 1) domains, an influence of the finite terrace sizes is only detectable for a sufficiently high density of steps. In particular, if

the merely three (4×1) In nanowires fit onto the terrace, the formation of (8×2) domains is forced to set in close to the step edges, and thus is influenced as well by the decrease of interchain coupling present there resulting in a lowering of the phase transition temperature.

α -Sn phase on Si(111)

The investigations on the α -Sn phase grown on Si(111) are discussed in detail in chapter 6. It is made up of $1/3$ ML Sn forming a structural 2D ($\sqrt{3} \times \sqrt{3}$) reconstruction on top of the substrate. So far, it has been considered a prototypical Mott system, as it shows an isostructural Mott metal-insulator phase transition below a critical temperature of $T_c \approx 70$ K due to strong electronic correlation effects [66, 206]. Since the spin-orbit gap for Sn atoms is relatively small compared to, e.g., Pb, because it scales with Z^4 , the influence of SOC on this system only recently came into the focus of research.

As it turns out, the intrinsic spin-orbit interaction is not negligible in the low-temperature phase. By means of spin- and angle-resolved photoemission, a spin-resolved band structure was now identified. It originates from a row-wise antiferromagnetic order with a ($2\sqrt{3} \times \sqrt{3}$) symmetry [21]. This spin unit cell occurs if Sn atoms of the structural ($\sqrt{3} \times \sqrt{3}$) reconstruction are associated with a spin, and every other row of Sn atoms carries the same spin. Generally, three rotational domains are present on the surface, and thus the superposition of their band structures was measured by ARPES. This results in a rather broad appearance of the surface state that is responsible for the MIT, as the three domains disperse slightly different if measured along high symmetry directions.

Based on the spin components directly obtained by SARPES and theoretical calculations [205], a model of the spin-resolved bandstructure was proposed. Accordingly, the SOC induces a small Rashba-type spin-splitting of the surface state, which is around $\Delta k \approx 0.05 \text{ \AA}^{-1}$. Hence, the rectangular SBZ of the ($2\sqrt{3} \times \sqrt{3}$) spin structure comprises two almost circularly shaped bands with opposite spin directions, which are located around the \bar{Y} points. Furthermore, corresponding to the acquired data of the spin orientation, an in-plane spin ordering is expected for this antiferromagnetic phase. All in all, on account of the analysis presented in this thesis, the low-temperature phase of α -Sn may rather be termed as a weakly spin-orbit coupled Mott system.

Formation of Sn-induced nanowires on vicinal silicon surfaces

Regarding the fascinating properties of the 2D α -Sn system caused by the influence of SOC on the Mott insulating low-temperature phase and the wealth of peculiar effects observed on nanowires, Sn-induced nanowires on silicon substrates obviously are a promising candidate for revealing finite-size effects in electronically correlated systems. Therefore, a detailed feasibility study on the growth of such nanowires on Si(557) is presented in chapter 7.

Employing STM and LEED, three distinct phases were identified, which are formed at different Sn coverages. For $\theta \approx 0.6$ ML, the surface orientation changes to local (223) facets separated by wider (111) terraces. Unlike for Pb/Si(557), where the formation of (223) facets is favored due to nesting conditions, this refacetting is solely induced by the formation of the two-layered high coverage ($2\sqrt{3} \times 2\sqrt{3}$) reconstruction on the (111) terraces and the resulting destabilization of the triple steps of the bare Si(557) substrate. On the (223) faceted parts, only a highly defective atomic chain structure is found instead of a well-defined reconstruction.

The long-range ordering is neither improved by adding extra amounts of Sn nor by changing the inclination angle of the substrate in order to decrease the number of (111) terraces. Further adsorbed Sn atoms tend to accumulate on the (111) terraces, which consequently increase in width. Eventually, step bunching occurs and the surface is dominated by large (111) terraces entirely covered by a $(2\sqrt{3} \times 2\sqrt{3})$ reconstruction.

For the low coverage Sn nanowires, i.e., $\theta < 0.5$ ML, the initial surface structure of Si(557) is preserved, and a homogeneously stepped array of approximately 3 nm wide α -Sn nanowires is formed. Since this structure is particularly interesting concerning electronic investigations, the band structure was probed at low temperatures by ARPES. A metallic surface state in the direction across the nanowires was clearly revealed, while the system remained insulating along the wires. Responsible for the quenching of the Mott-gap across the wires might either be doping of the Mott phase via step edges or the finite width of the nanowires, which is comparable in size to the coherence length of the Mott state.

Pb nanowires on a vicinal silicon substrate

For the growth of Pb nanowires analyzed in chapter 8, a vicinal Si(557) substrate was used as well as a template. Upon adsorption of 1.3 ML Pb, the triple-stepped surface of the bare substrate is destabilized and facets into local (223) oriented parts, which are separated by wider (111) terraces. On the latter, two distinct phases coexist. The majority of terraces is covered by a single-domain SIC- $(\sqrt{3} \times \sqrt{3})$ phase consisting of Pb tetramers adsorbed either on T_4 or H_3 lattice sites of the underlying Si substrate. On (111) terraces with a width of about 3 nm, a modulated Pb- $\sqrt{3}$ phase is present. A structural model of it was proposed based on high-resolution STM images, comprising of Pb tetramers, which are arranged in a more densely packed fashion than for the SIC phase with a total Pb coverage of 1.44 – 1.46 ML. Hence, their adsorption sites vary slightly, giving rise to a superstructure with a length between 2 and 2.4 nm.

On the (223) facets, a similar modulated Pb- $\sqrt{3}$ reconstruction is formed on top of mini-(111) terraces but having a length of about 4 nm, as revealed by STM measurements. Besides, the step edges are covered by two rows of Pb atoms with a spacing 0.70 nm, instead of the formerly assumed dimerized Si bonds. Addition of excess coverage up to $\delta\theta = 0.2$ ML leads to two prominent structural changes, namely the filling up of one of the Pb rows on the step edge, and the formation of an extra Pb row squeezed in between the Pb tetramers on the mini-(111) terrace. If even more Pb is added to the surface, it tends to accumulate in a second layer on top of the Pb tetramers. These high coverage nanowires coexist in separated domains with the single-layered nanowires.

Electronically, the 1.3 ML nanowires are well-known to undergo a MIT below $T_c \approx 78$ K due to the formation of an insulating SODW in the direction across the nanowires [41]. According to STS data, a finite DOS at E_F exists above T_c , while it vanishes upon cooling due to the opening of an insulating gap with the size of $2\Delta = (31.8 \pm 0.5)$ meV, which is in good agreement with previously reported ARPES results [112]. Upon adsorption of excess Pb, a metallic state located at the step edge remains stable even at low temperatures. Eventually, this leads to a complete breakdown of the insulating SODW phase for an extra coverage of $\delta\theta = 0.2$ ML. Consequently, the double-layered nanowires do not show a phase transition at 78 K either but rather stay metallic as well.

Conclusion

This thesis provides a detailed study on the finite-size effects and SOC on low-dimensional systems. On account of spatial confinement, electron-phonon interaction is reduced. This has a major influence on Peierls-like phase transitions, leading to a shift of the critical temperature to lower values. Besides, in case of electronically correlated systems, phase transitions can even be suppressed, if their coherence length exceeds the finite width of the confined area.

Furthermore, for Pb/Si(557), SOC is strongly enhanced compared to the 2D Pb SIC phase on Si(111). This is due to the finite size of the nanowires and the resulting Fermi nesting condition, which give rise to the SODW. It has been shown, that it is not only caused by the (223) faceted surface, but the well-ordered Pb nanowires are essential as well. Albeit the 2D α -Sn phase shows a similar Rashba-splitting of the surface state, Sn does not form any long-range ordered structure on (223) facets as it is merely induced by the formation of extended (111) terraces.

Outlook

The investigations presented in the scope of this thesis revealed a plethora of possibilities for tuning metal-insulator transitions of low dimensional metallic films on silicon substrates by means of finite-size effects and SOC. In this connection, the phase transition can be either shifted to lower temperatures, e.g. by means of spatial confinement in the case of In/Si(111), or even suppressed, as seen for excess Pb atoms adsorbed on Pb/Si(557) as well as for the confined α -Sn phase. So far, all of these approaches have in common, that the system's properties are altered without the addition of other materials onto the surface.

Indeed, it is already well-known, that adsorbates, such as hydrogen or oxygen, may delicately influence the electronic structure, and thus change the temperature for the occurrence of the structural phase transition e.g. of In/Si(111) [37–39]. Besides, the choice of adsorbates is not merely restricted to single atoms. For example, noninvasive charge transfer doping is feasible by physisorption of molecular layers, as recently shown for graphene [236]. In particular, molecule classes such as phthalocyanine (Pc) can be functionalized by variation of both the size and the charge state of the core atom [237]. Moreover, if the central atom exceeds the size of the cavity of the Pc molecule, it arranges in a shuttlecock fashion, which can be reversely switched from up to down configuration [238]. Therefore, they seem to be a promising candidate for tailoring the electronic properties of future devices in nanoelectronics.

Concerning this topic, a first feasibility check was already done by evaporation of MnPc molecules on top of Pb nanowires grown on Si(557) (cf. chapter 8). In fact, the molecules form well-ordered close-packed layers on top of the Pb/Si(557). As depicted in the STM images presented in Figs. 9.1 (a)-(c), the surface orientation featuring (223) facets and wider (111) is maintained, indicating a noninvasive coupling to the surface, which preserves the underlying Pb reconstruction. On top of the (111) terraces, the MnPc is ordered in a square arrangement with a width of approximately 1.3 nm, which differs only slightly from the value reported for the nearly quadratic lattice of MnPc on Pb(111), i.e., 1.4 nm [239]. A similar spacing between adjacent molecules is observed on top of the (223) oriented parts. Since the size of the MnPc molecule is comparable to the Pb nanowire width, a single row of molecules is adsorbed on top of every wire.

Besides, the electronic properties of the system were probed utilizing STS, as seen in Fig.

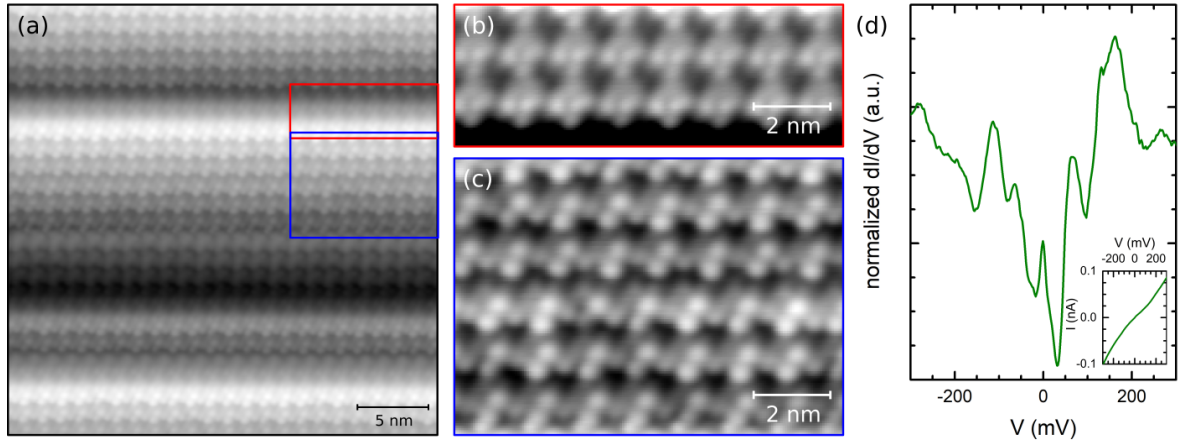


Figure 9.1: (a) Overview STM image of MnPc evaporated on Pb/Si(557) ($U = 0.2$ V, $I = 0.1$ nA, $T = 6$ K). Enlargement of the molecules adsorbed on (b) the wider (111) terraces and (c) the (223) oriented parts are highlighted with red and blue rectangles, respectively. (d) Normalized dI/dV spectrum averaged over several curves obtained on the center of MnPc molecules on the (223) facets. The inset shows the corresponding $I(V)$ curve.

9.1(d). At temperatures well below the phase transition temperature of Pb/Si(557), the system clearly remains metallic. This leads to the conclusion that the adsorption of MnPc on the Pb nanowires preserves the structural properties while altering the electronic landscape by either suppression of the insulating low-temperature SODW phase or the addition of molecule-induced surface states inside the gap.

Apart from the evaporation of entire monolayers of molecules onto quasi-1D systems, a further approach of tuning the nanowire's properties is by adsorption of single molecules, and the subsequent increase of coverage. This certainly would give more insight into the range of the molecule's influence, as well as its specific adsorption sites on top of the chains.

Part IV
Appendix

Bibliography

- [1] G. E. MOORE: Cramming more components onto integrated circuits, Reprinted from *Electronics*, volume 38, number 8, April 19, 1965, pp.114 ff. *IEEE Solid-State Circuits Society Newsletter*, vol. 11(3) (Sept. 2006), pp. 33–35. ISSN: 1098-4232 (cit. on p. 3). DOI: 10.1109/N-SSC.2006.4785860.
- [2] R. R. SCHALLER: Moore’s law: past, present and future. *IEEE Spectrum*, vol. 34(6) (June 1997), pp. 52–59. ISSN: 0018-9235 (cit. on p. 3). DOI: 10.1109/6.591665.
- [3] C. A. MACK: Fifty Years of Moore’s Law. *IEEE Transactions on Semiconductor Manufacturing*, vol. 24(2) (May 2011), pp. 202–207. ISSN: 0894-6507 (cit. on p. 3). DOI: 10.1109/TSM.2010.2096437.
- [4] F. XIE et al.: Quasi-Solid-State Single-Atom Transistors. *Advanced Materials*, vol. 30(31) (June 2018), p. 1801225 (cit. on p. 3). DOI: 10.1002/adma.201801225.
- [5] M. FUECHSLE et al.: A single-atom transistor. *Nature Nanotechnology*, vol. 7 (Feb. 2012), pp. 242–246 (cit. on p. 3). DOI: 10.1038/nnano.2012.21.
- [6] Z. DURRANI et al.: Room-temperature single dopant atom quantum dot transistors in silicon, formed by field-emission scanning probe lithography. *Journal of Applied Physics*, vol. 124(14) (Nov. 2018), p. 144502 (cit. on p. 3). DOI: 10.1063/1.5050773.
- [7] F.-Q. XIE et al.: Independently Switchable Atomic Quantum Transistors by Reversible Contact Reconstruction. *Nano Letters*, vol. 8(12) (Nov. 2008), pp. 4493–4497 (cit. on p. 3). DOI: 10.1021/nl1802438c.
- [8] G. S. SNIDER and R. S. WILLIAMS: Nano/CMOS architectures using a field-program-

- mable nanowire interconnect. *Nanotechnology*, vol. 18(3) (Jan. 2007), p. 035204 (cit. on p. 3).
DOI: 10.1088/0957-4484/18/3/035204.
- [9] J. JIU and K. SUGANUMA: Metallic Nanowires and Their Application. *IEEE Transactions on Components, Packaging and Manufacturing Technology*, vol. 6(12) (Dec. 2016), pp. 1733–1751. ISSN: 2156-3950 (cit. on p. 3).
DOI: 10.1109/TCPMT.2016.2581829.
- [10] T. SANNICOLO et al.: Metallic Nanowire-Based Transparent Electrodes for Next Generation Flexible Devices: a Review. *Small*, vol. 12(44) (Oct. 2016), pp. 6052–6075 (cit. on p. 3).
DOI: 10.1002/smll.201602581.
- [11] D. S. GINLEY, H. HOSONO, and D. C. PAINE: *Handbook of Transparent Conductors*. Springer, Boston, MA, 2010 (cit. on p. 3).
DOI: 10.1007/978-1-4419-1638-9.
- [12] D. S. HECHT, L. HU, and G. IRVIN: Emerging Transparent Electrodes Based on Thin Films of Carbon Nanotubes, Graphene, and Metallic Nanostructures. *Advanced Materials*, vol. 23(13) (Feb. 2011), pp. 1482–1513 (cit. on p. 3).
DOI: 10.1002/adma.201003188.
- [13] D. LANGLEY et al.: Flexible transparent conductive materials based on silver nanowire networks: a review. *Nanotechnology*, vol. 24(45) (Oct. 2013), p. 452001 (cit. on p. 3).
DOI: 10.1088/0957-4484/24/45/452001.
- [14] C. MAYOUSSE et al.: Improvements in purification of silver nanowires by decantation and fabrication of flexible transparent electrodes. Application to capacitive touch sensors. *Nanotechnology*, vol. 24(21) (Apr. 2013), p. 215501 (cit. on p. 3).
DOI: 10.1088/0957-4484/24/21/215501.
- [15] C. CELLE et al.: Highly flexible transparent film heaters based on random networks of silver nanowires. *Nano Research*, vol. 5(6) (June 2012), pp. 427–433. ISSN: 1998-0000 (cit. on p. 3).
DOI: 10.1007/s12274-012-0225-2.
- [16] B. J HINCH, C KOZIOL, J. P TOENNIES, and G ZHANG: Evidence for Quantum Size Effects Observed by Helium Atom Scattering during the Growth of Pb on Cu(111). *Europhysics Letters (EPL)*, vol. 10(4) (Oct. 1989), pp. 341–346 (cit. on p. 3).
DOI: 10.1209/0295-5075/10/4/010.
- [17] K. BUDDE, E. ABRAM, V. YEH, and M. C. TRINGIDES: Uniform, self-organized, seven-step height Pb/Si(111) – (7 × 7) islands at low temperatures. *Phys. Rev. B*, vol. 61 (Aug. 16, Apr. 2000), R10602–R10605 (cit. on p. 3).
DOI: 10.1103/PhysRevB.61.R10602.

-
- [18] W. WITCZAK-KREMPA, G. CHEN, Y. B. KIM, and L. BALENTS: Correlated Quantum Phenomena in the Strong Spin-Orbit Regime. *Annual Review of Condensed Matter Physics*, vol. 5 (2013), p. 57 (cit. on pp. 3, 10, 11, 67, 69).
DOI: 10.1146/annurev-conmatphys-020911-125138.
- [19] P. HÖPFNER et al.: Three-Dimensional Spin Rotations at the Fermi Surface of a Strongly Spin-Orbit Coupled Surface System. *Phys. Rev. Letters*, vol. 108(18) (Apr. 2012), p. 186801 (cit. on p. 3).
DOI: 10.1103/PhysRevLett.108.186801.
- [20] S. GLASS et al.: Triangular Spin-Orbit-Coupled Lattice with Strong Coulomb Correlations: Sn Atoms on a SiC(0001) Substrate. *Phys. Rev. Letters*, vol. 114(24) (June 2015), p. 247602 (cit. on p. 3).
DOI: 10.1103/PhysRevLett.114.247602.
- [21] G. LI et al.: Magnetic order in a frustrated two-dimensional atom lattice at a semiconductor surface. *Nature Communications*, vol. 4 (Mar. 2013), p. 1620 (cit. on pp. 3, 5, 11, 60–63, 69, 71, 100).
DOI: 10.1038/ncomms2617.
- [22] R. BLATT and D. WINELAND: Entangled states of trapped atomic ions. *Nature*, vol. 453 (June 2008), pp. 1008–1015 (cit. on p. 4).
DOI: 10.1038/nature07125.
- [23] S. MURMANN et al.: Antiferromagnetic Heisenberg Spin Chain of a Few Cold Atoms in a One-Dimensional Trap. *Phys. Rev. Letters*, vol. 115(21) (Nov. 2015), p. 215301 (cit. on p. 4).
DOI: 10.1103/PhysRevLett.115.215301.
- [24] H. OHNISHI, Y. KONDO, and K. TAKAYANAGI: Quantized conductance through individual rows of suspended gold atoms. *Nature*, vol. 395 (Oct. 1998), pp. 780–783 (cit. on p. 4).
DOI: 10.1038/27399.
- [25] H. OKINO et al.: Influence of defects on transport in quasi-one-dimensional arrays of chains of metal atoms on silicon. *Phys. Rev. B*, vol. 76(19) (Nov. 2007), p. 195418 (cit. on pp. 4, 18, 27).
DOI: 10.1103/PhysRevB.76.195418.
- [26] T. UETAKE et al.: Anisotropic conductivity of the Si(111)4 × 1-In surface: Transport mechanism determined by the temperature dependence. *Phys. Rev. B*, vol. 86 (Aug. 3, July 2012), p. 035325 (cit. on pp. 4, 27, 29, 53).
DOI: 10.1103/PhysRevB.86.035325.
- [27] F. EDLER, I. MICCOLI, H. PFNÜR, and C. TEGENKAMP: Space charge layer effects

- in silicon studied by in situ surface transport. *Journal of Physics: Condensed Matter*, vol. 31(21) (Mar. 2019), p. 214001 (cit. on pp. 4, 13, 27).
DOI: 10.1088/1361-648x/ab094e.
- [28] J. M. CARPINELLI, H. H. WEITERING, E. W. PLUMMER, and R. STUMPF: Direct observation of a surface charge density wave. *Nature*, vol. 381 (May 1996), p. 398 (cit. on p. 4).
DOI: 10.1038/381398a0.
- [29] A. MASCARAQUE, J. AVILA, E. G. MICHEL, and M. C. ASENSIO: Fermi surface and electronic structure of Pb/Ge(111). *Phys. Rev. B*, vol. 57(23) (June 1998), pp. 14758–14765 (cit. on pp. 4, 60).
DOI: 10.1103/PhysRevB.57.14758.
- [30] R. E. PEIERLS: *Quantum Theory of Solids*. Clarendon Press, Oxford, 1955. ISBN: 9780198507819 (cit. on pp. 4, 7, 14, 15).
DOI: 10.1093/acprof:oso/9780198507819.001.0001.
- [31] H. W. YEOM et al.: Instability and Charge Density Wave of Metallic Quantum Chains on a Silicon Surface. *Phys. Rev. Letters*, vol. 82(24) (June 1999), pp. 4898–4901 (cit. on pp. 4, 15).
DOI: 10.1103/PhysRevLett.82.4898.
- [32] S. WIPPERMANN and W. G. SCHMIDT: Entropy Explains Metal-Insulator Transition of the Si(111)-In Nanowire Array. *Phys. Rev. Letters*, vol. 105(12) (Sept. 2010), p. 126102 (cit. on p. 4).
DOI: 10.1103/PhysRevLett.105.126102.
- [33] S. V. RYJKOV, T. NAGAO, V. G. LIFSHITS, and S. HASEGAWA: Phase transition and stability of Si(111)-8×2'-In surface phase at low temperatures. *Surface Science*, vol. 488(1) (2001), pp. 15–22. ISSN: 0039-6028 (cit. on p. 4).
DOI: 10.1016/S0039-6028(01)01145-1.
- [34] S. S. LEE et al.: Adsorbate-Induced Pinning of a Charge-Density Wave in a Quasi-1D Metallic Chains: Na on the In/Si(111)-(4×1) Surface. *Phys. Rev. Letters*, vol. 88(19) (Apr. 2002), p. 196401 (cit. on p. 4).
DOI: 10.1103/PhysRevLett.88.196401.
- [35] H. SHIM et al.: Control of phase transition in quasi-one-dimensional atomic wires by electron doping. *Applied Physics Letters*, vol. 94(23) (2009), p. 231901 (cit. on p. 4).
DOI: 10.1063/1.3143719.
- [36] H. MORIKAWA, C. C. HWANG, and H. W. YEOM: Controlled electron doping into metallic atomic wires: Si(111)4×1-In. *Phys. Rev. B*, vol. 81(7) (Feb. 2010), p. 075401 (cit. on p. 4).
DOI: 10.1103/PhysRevB.81.075401.

-
- [37] G. LEE et al.: Roles of defects induced by hydrogen and oxygen on the structural phase transition of Si(111) 4×1 -In. *Phys. Rev. B*, vol. 80(7) (Aug. 2009), p. 075411 (cit. on pp. 4, 102).
DOI: 10.1103/PhysRevB.80.075411.
- [38] T. SHIBASAKI et al.: Phase transition temperatures determined by different experimental methods: Si(111) 4×1 -In surface with defects. *Phys. Rev. B*, vol. 81(3) (Jan. 2010), p. 035314 (cit. on pp. 4, 102).
DOI: 10.1103/PhysRevB.81.035314.
- [39] H. W. YEOM, D. M. OH, S. WIPPERMANN, and W. G. SCHMIDT: Impurity-Mediated Early Condensation of a Charge Density Wave in an Atomic Wire Array. *ACS Nano*, vol. 10 (2016), pp. 810–814 (cit. on pp. 4, 102).
DOI: 10.1021/acsnano.5b05925.
- [40] J. CRAIN and F. HIMPSEL: Low-dimensional electronic states at silicon surfaces. *Applied Physics A*, vol. 82(3) (Feb. 2006), pp. 431–438. ISSN: 1432-0630 (cit. on p. 4).
DOI: 10.1007/s00339-005-3365-3.
- [41] C. BRAND et al.: Observation of correlated spin-orbit order in a strongly anisotropic quantum wire system. *Nature Communications*, vol. 6 (Sept. 2015), p. 8118 (cit. on pp. 4, 20–22, 69, 72, 75, 81, 94, 101).
DOI: 10.1038/ncomms9118.
- [42] C. TEGENKAMP et al.: Anisotropic conductance of Pb-induced chain structures on Si(557) in the monolayer regime. *The European Physical Journal B - Condensed Matter and Complex Systems*, vol. 43(4) (Feb. 2005), pp. 557–564. ISSN: 1434-6036 (cit. on pp. 4, 21, 81, 82, 91).
DOI: 10.1140/epjb/e2005-00090-x.
- [43] C. TEGENKAMP and H. PFNÜR: Switching between one- and two-dimensional conductance: Coupled chains in the monolayer of Pb on Si(557). *Surface Science*, vol. 601(13) (July 2007), pp. 2641–2646. ISSN: 0039-6028 (cit. on pp. 4, 5, 81, 86, 87).
DOI: 10.1016/j.susc.2006.11.068.
- [44] H. PFNÜR et al.: Correlation of geometrical and electronic properties in metallic nanowires. *Physica status solidi b*, vol. 247(10) (Sept. 2010), pp. 2509–2521 (cit. on pp. 4, 81, 82, 91).
DOI: 10.1002/pssb.201046103.
- [45] M. CZUBANOWSKI, H. PFNÜR, and C. TEGENKAMP: Atomic chain ordering with ultra-long periods: Pb/Si(557). *Surface Science*, vol. 603(19) (2009), pp. L121–L124. ISSN: 0039-6028 (cit. on pp. 4, 5, 81).
DOI: 10.1016/j.susc.2009.08.013.
- [46] F. MING et al.: Realization of a Hole-Doped Mott Insulator on a Triangular Silicon

- Lattice. *Phys. Rev. Letters*, vol. 119(26) (Dec. 2017), p. 266802 (cit. on pp. 5, 13, 14, 71, 78).
DOI: 10.1103/PhysRevLett.119.266802.
- [47] F. GEBHARD: *The Mott Metal-Insulator Transition. Models and Methods*. Ed. by G. HÖHLER et al. Springer Tracts in Modern Physics 137. Springer Verlag, 1997. ISBN: 978-3-540-14858-6 (cit. on p. 7).
DOI: 10.1007/3-540-14858-2.
- [48] F. BLOCH: Bemerkung zur Elektronentheorie des Ferromagnetismus und der elektrischen Leitfähigkeit. *Zeitschrift für Physik*, vol. 57(7) (July 1929), pp. 545–555 (cit. on p. 7).
DOI: 10.1007/BF01340281.
- [49] A. H. WILSON and P. A. M. DIRAC: The theory of electronic semi-conductors. *Proceedings of the Royal Society A*, vol. 133(822) (Oct. 1931), pp. 458–491 (cit. on pp. 7, 8).
DOI: 10.1098/rspa.1931.0162.
- [50] A. H. WILSON and P. A. M. DIRAC: The theory of electronic semi-conductors.-II. *Proceedings of the Royal Society A*, vol. 134(823) (Nov. 1931), pp. 277–287 (cit. on p. 7).
DOI: 10.1098/rspa.1931.0196.
- [51] P. W. ANDERSON: Absence of Diffusion in Certain Random Lattices. *Physical Review*, vol. 109(5) (Mar. 1958), pp. 1492–1505. ISSN: 0022-4596 (cit. on p. 7).
DOI: 10.1103/PhysRev.109.1492.
- [52] N. F. MOTT: *Metal-Insulator Transitions*. 2nd ed. London: Taylor & Francis, 1990. ISBN: 9781466576452 (cit. on pp. 7, 8).
- [53] J. H. de BOER and E. J. W. VERWEY: Semi-conductors with partially and with completely filled 3d-lattice bands. *Proceedings of the Physical Society*, vol. 49(4S) (1937), p. 59 (cit. on p. 8).
DOI: 10.1088/0959-5309/49/4S/307.
- [54] N. F. MOTT and R PEIERLS: Discussion of the paper by de Boer and Verwey. *Proceedings of the Physical Society*, vol. 49(4S) (1937), p. 72 (cit. on p. 8).
DOI: 10.1088/0959-5309/49/4S/308.
- [55] N. F. MOTT: The Basis of the Electron Theory of Metals, with Special Reference to the Transition Metals. *Proceedings of the Physical Society. Section A*, vol. 62(7) (1949), p. 416 (cit. on p. 8).
DOI: 10.1088/0370-1298/62/7/303.
- [56] N. F. MOTT: The transition to the metallic state. *The Philosophical Magazine: A*

-
- Journal of Theoretical Experimental and Applied Physics*, vol. 6(62) (1961), pp. 287–309 (cit. on p. 8).
DOI: 10.1080/14786436108243318.
- [57] M. C. GUTZWILLER: Effect of Correlation on the Ferromagnetism of Transition Metals. *Phys. Rev. Letters*, vol. 10(5) (Mar. 1963), pp. 159–162 (cit. on pp. 8, 9).
DOI: 10.1103/PhysRevLett.10.159.
- [58] J. HUBBARD and B. H. FLOWERS: Electron correlations in narrow energy bands. *Proceedings of the Royal Society A*, vol. 276(1365) (Nov. 1963), pp. 238–257 (cit. on p. 8).
DOI: 10.1098/rspa.1963.0204.
- [59] J. HUBBARD and B. H. FLOWERS: Electron correlations in narrow energy bands. *Proceedings of the Royal Society A*, vol. 277(1369) (Jan. 1964), pp. 237–259 (cit. on p. 8).
DOI: 10.1098/rspa.1964.0019.
- [60] A. L. FETTER and J. D. WALECKA: *Quantum Theory of Many-Particle Systems*. Dover Books on Physics. Dover Publications, 2003. ISBN: 9780486134758 (cit. on p. 9).
URL: https://books.google.de/books?id=t5_DAgAAQBAJ.
- [61] M. IMADA, A. FUJIMORI, and Y. TOKURA: Metal-insulator transitions. *Rev. Mod. Physics*, vol. 70(4) (Oct. 1998), pp. 1039–1263 (cit. on p. 10).
DOI: 10.1103/RevModPhys.70.1039.
- [62] P. A. HÖPFNER: “Two-Dimensional Electron Systems at Surfaces”. PhD thesis. Julius-Maximilians-Universität Würzburg, 2012 (cit. on pp. 10, 58).
- [63] W. NOLTING: *Grundkurs Theoretische Physik 5/2. Quantenmechanik - Methoden und Anwendungen*. 8th ed. Springer-Verlag, 2015. ISBN: 978-3-662-44230-2 (cit. on p. 10).
DOI: 10.1007/978-3-662-44230-2.
- [64] A. LANDÉ: Termstruktur und Zeemaneffekt der Multipletts. *Zeitschrift für Physik*, vol. 15(1) (Dec. 1923), pp. 189–205. ISSN: 0044-3328 (cit. on p. 11).
DOI: 10.1007/BF01330473.
- [65] I. V. HERTEL and C.-P. SCHULZE: *Atome, Moleküle und optische Physik 1. Atomphysik und Grundlagen der Spektroskopie*. Springer Lehrbuch. Berlin, Heidelberg: Springer Verlag, 2008. ISBN: 978-3-540-30617-7 (cit. on p. 11).
DOI: 10.1007/978-3-540-30617-7.
- [66] S. MODESTI et al.: Insulating Ground State of Sn/Si(111)–($\sqrt{3}\times\sqrt{3}$)R30°. *Phys. Rev. Letters*, vol. 98(12) (Mar. 2007), p. 126401 (cit. on pp. 11, 60, 77, 100).
DOI: 10.1103/PhysRevLett.98.126401.

- [67] R. WINKLER: *Spin-Orbit Coupling Effects in Two-Dimensional Electron and Hole Systems*. Springer Tracts in Modern Physics 191. Berlin, Heidelberg: Springer, 2003. Chap. The Extended Kane Model, pp. 21–34. ISBN: 978-3-540-36616-4 (cit. on pp. 11, 32).
DOI: 10.1007/978-3-540-36616-4_3.
- [68] J. C. PHILLIPS: *Bonds and bands in semiconductors*. New York, London: Academic Press, 1973. ISBN: 0125533500 (cit. on pp. 11, 32).
- [69] Y. CAO et al.: Hallmarks of the Mott-metal crossover in the hole-doped pseudospin-1/2 Mott insulator Sr_2IrO_4 . *Nature Communications*, vol. 7 (Apr. 2016), p. 11367 (cit. on p. 12).
DOI: 10.1038/ncomms11367.
- [70] A. DAMASCELLI, Z. HUSSAIN, and Z.-X. SHEN: Angle-resolved photoemission studies of the cuprate superconductors. *Rev. Mod. Physics*, vol. 75(2) (Apr. 2003), pp. 473–541 (cit. on pp. 12, 71).
DOI: 10.1103/RevModPhys.75.473.
- [71] G. AMOW, N. RAJU, and J. GREEDAN: Metal–Insulator Phenomena in Strongly Correlated Oxides. The Vacancy-Doped Titanate Perovskites, $\text{Nd}_{(1-x)}\text{TiO}_3$ and $\text{Sm}_{(1-x)}\text{TiO}_3$. *Journal of Solid State Chemistry*, vol. 155(1) (2000), pp. 177–188. ISSN: 0022-4596 (cit. on pp. 12, 71).
DOI: 10.1006/jssc.2000.8932.
- [72] T. F. QI et al.: Spin-orbit tuned metal-insulator transitions in single-crystal $\text{Sr}_2\text{Ir}_{1-x}\text{Rh}_x\text{O}_4$ ($0 \leq x \leq 1$). *Phys. Rev. B*, vol. 86(12) (Sept. 2012), p. 125105 (cit. on p. 12).
DOI: 10.1103/PhysRevB.86.125105.
- [73] T. HOGAN et al.: First-Order Melting of a Weak Spin-Orbit Mott Insulator into a Correlated Metal. *Phys. Rev. Letters*, vol. 114(25) (June 2015), p. 257203 (cit. on p. 13).
DOI: 10.1103/PhysRevLett.114.257203.
- [74] G. AFFELDT et al.: Spectral weight suppression near a metal-insulator transition in a double-layer electron-doped iridate. *Phys. Rev. B*, vol. 95(23) (June 2017), p. 235151 (cit. on pp. 12, 71).
DOI: 10.1103/PhysRevB.95.235151.
- [75] L. LI et al.: Tuning the $J_{\text{eff}} = \frac{1}{2}$ insulating state via electron doping and pressure in the double-layered iridate $\text{Sr}_3\text{Ir}_2\text{O}_7$. *Phys. Rev. B*, vol. 87(23) (June 2013), p. 235127 (cit. on p. 12).
DOI: 10.1103/PhysRevB.87.235127.
- [76] J. D. MOTTRAM, A. THANAILAKIS, and D. C. NORTHROP: P-type surface layers on

-
- n-type silicon heat-cleaned in UHV. *Journal of Physics D: Applied Physics*, vol. 8(11) (1975), pp. 1316–1320 (cit. on p. 13).
DOI: 10.1088/0022-3727/8/11/010.
- [77] M. LIEHR, M. RENIER, R. A. WACHNIK, and G. S. SCILLA: Dopant redistribution at Si surfaces during vacuum anneal. *Journal of Applied Physics*, vol. 61(9) (1987), pp. 4619–4625 (cit. on pp. 13, 29, 53).
DOI: 10.1063/1.338372.
- [78] S. BENSALAH, J.-P. LACHARME, and C. A. SÉBENNE: Effect of vacuum annealings on the electronic properties of clean Si(111) surfaces. *Phys. Rev. B*, vol. 43(18) (June 1991), pp. 14441–14446 (cit. on p. 13).
DOI: 10.1103/PhysRevB.43.14441.
- [79] U. KRIEG et al.: Origin of metallicity in atomic Ag wires on Si(557). *New Journal of Physics*, vol. 17(4) (Apr. 2015), p. 043062 (cit. on pp. 14, 71).
DOI: 10.1088/1367-2630/17/4/043062.
- [80] S. KAGOSHIMA: Peierls Phase Transition. *Japanese Journal of Applied Physics*, vol. 20(9) (Sept. 1981), pp. 1617–1634 (cit. on p. 15).
DOI: 10.1143/JJAP.20.1617.
- [81] S. KAGOSHIMA, H. NAGASAWA, and T. SAMBONGI: *One-Dimensional Conductors*. Springer Series in Solid-State Sciences 72. Berlin, Heidelberg: Springer Verlag, 1988. ISBN: 978-3-642-83179-9 (cit. on p. 15).
DOI: 10.1007/978-3-642-83179-9.
- [82] T. FRIGGE et al.: Optically excited structural transition in atomic wires on surfaces at the quantum limit. *Nature*, vol. 544 (Mar. 2017), p. 207 (cit. on p. 15).
DOI: 10.1038/nature21432.
- [83] C. W. NICHOLSON et al.: Beyond the molecular movie: Dynamics of bands and bonds during a photoinduced phase transition. *Science*, vol. 362(6416) (2018), pp. 821–825. ISSN: 0036-8075 (cit. on p. 15).
DOI: 10.1126/science.aar4183.
- [84] F. KLASING et al.: Hysteresis proves that the In/Si(111) (8×2) to (4×1) phase transition is first-order. *Phys. Rev. B*, vol. 89(12) (Mar. 2014), p. 121107 (cit. on pp. 16–18, 47, 50, 55, 56, 99).
DOI: 10.1103/PhysRevB.89.121107.
- [85] S. J. PARK et al.: Direct Evidence of the Charge Ordered Phase Transition of Indium Nanowires on Si(111). *Phys. Rev. Letters*, vol. 93(10) (Sept. 2004), p. 106402 (cit. on pp. 16, 17).
DOI: 10.1103/PhysRevLett.93.106402.

- [86] J. GUO, G. LEE, and E. W. PLUMMER: Intertwined Electronic and Structural Phase Transitions in the In/Si(111) Interface. *Phys. Rev. Letters*, vol. 95(4) (July 2005), p. 046102 (cit. on p. 17).
DOI: 10.1103/PhysRevLett.95.046102.
- [87] C. KUMPF et al.: Low-Temperature Structure of Indium Quantum Chains on Silicon. *Phys. Rev. Letters*, vol. 85(23) (Dec. 2000), pp. 4916–4919 (cit. on p. 16).
DOI: 10.1103/PhysRevLett.85.4916.
- [88] S. HATTA, T. NOMA, H. OKUYAMA, and T. ARUGA: Electrical conduction and metal-insulator transition of indium nanowires on Si(111). *Phys. Rev. B*, vol. 95 (Aug. 19, May 2017), p. 195409 (cit. on pp. 16, 18–20, 47, 50, 55, 56, 99).
DOI: 10.1103/PhysRevB.95.195409.
- [89] T. TANIKAWA, I. MATSUDA, T. KANAGAWA, and S. HASEGAWA: Surface-State Electrical Conductivity at a Metall. Insulator Transition On Silicon. *Phys. Rev. Letters*, vol. 93(1) (July 2004), p. 016801 (cit. on p. 17).
DOI: 10.1103/PhysRevLett.93.016801.
- [90] U. GERSTMANN et al.: Rashba splitting and relativistic energy shifts in In/Si(111) nanowires. *Phys. Rev. B*, vol. 89(16) (Apr. 2014), p. 165431 (cit. on pp. 17, 18).
DOI: 10.1103/PhysRevB.89.165431.
- [91] A. A. SARANIN et al.: Analysis of surface structures through determination of their composition using STM: Si(100) 4×3 -In and Si(111) 4×1 -In reconstructions. *Phys. Rev. B*, vol. 60(20) (Nov. 1999), p. 14372 (cit. on p. 17).
DOI: 10.1103/PhysRevB.60.14372.
- [92] A. V. ZOTOV et al.: Quantitative STM investigation of the phase formation in sub-monolayer In/Si(111) system. *Applied Surface Science*, vol. 159–160 (2000), pp. 237–242 (cit. on p. 17).
- [93] J. R. AHN et al.: Mechanism of Gap Opening in a Triple-Band Peierls System: In Atomic Wires on Si. *Phys. Rev. Letters*, vol. 93(10) (Sept. 2004), p. 106401 (cit. on p. 17).
DOI: 10.1103/PhysRevLett.93.106401.
- [94] G. LEE, J. GUO, and E. W. PUMMER: Real-Space Observation of Nanoscale Inhomogeneities and Fluctuations in a Phase Transition of a Surface Quasi-One-Dimensional System: In/Si(111). *Phys. Rev. Letters*, vol. 95 (Sept. 2005), p. 116103 (cit. on p. 17).
DOI: 10.1103/PhysRevLett.95.116103.
- [95] S. J. PARK, H. W. YEOM, J. R. AHN, and I. W. LYO: Atomic-Scale Phase Coexistence and Fluctuation at the Quasi-One-Dimensional Metal-Insulator-Transition. *Phys. Rev. Letters*, vol. 95 (Sept. 2005), p. 126102 (cit. on p. 17).
DOI: 10.1103/PhysRevLett.95.126102.

-
- [96] H. SHIM, Y. JEON, J. YEO, and G. LEE: Homogeneous and heterogeneous nucleations in the surface phase transition: Si(111) 4×1 -In. *New Journal of Physics*, vol. 17(6) (June 2015), p. 063026 (cit. on pp. 18, 20, 47, 50, 55, 56, 99).
DOI: 10.1088/1367-2630/17/6/063026.
- [97] J. L. STEVENS, M. S. WORTHINGTON, and I. S. T. TSONG: 4×1 reconstruction of indium deposited on vicinal Si(111) surfaces. *Phys. Rev. B*, vol. 47(3) (Jan. 1993), pp. 1453–1459 (cit. on pp. 18, 19, 48).
DOI: 10.1103/PhysRevB.47.1453.
- [98] T. ABUKAWA et al.: Surface electronic structure of a single-domain Si(111) 4×1 -In surface: a synchrotron radiation photoemission study. *Surface Science*, vol. 325(1) (Feb. 1995), pp. 33–44. ISSN: 0039-6028 (cit. on pp. 18, 51).
DOI: 10.1016/0039-6028(94)00693-8.
- [99] K FLEISCHER et al.: Atomic indium nanowires on Si(111): the (4×1) – (8×2) phase transition studied with reflectance anisotropy spectroscopy. *Applied Surface Science*, vol. 234(1) (July 2004). The Ninth International Conference on the Formation of Semiconductor Interfaces, pp. 302–306. ISSN: 0169-4332 (cit. on p. 18).
DOI: 10.1016/j.apsusc.2004.05.114.
- [100] A. A. STEKOLNIKOV et al.: Hexagon versus Trimer Formation in In Nanowires on Si(111): Energetics and Quantum Conductance. *Phys. Rev. Letters*, vol. 98(2) (Jan. 2007), p. 026105 (cit. on p. 20).
DOI: 10.1103/PhysRevLett.98.026105.
- [101] P. S. RISEBOROUGH, B. COQBLIN, and S. G. MAGALHÃES: Phase transition arising from the underscreened Anderson lattice model: A candidate concept for explaining hidden order in URu₂Si₂. *Phys. Rev. B*, vol. 85(16) (Apr. 2012), p. 165116 (cit. on p. 20).
DOI: 10.1103/PhysRevB.85.165116.
- [102] P. S. RISEBOROUGH, S. MAGALHÃES, and E. CALEGARI: Signatures of broken spin-rotational invariance in the “Hidden Ordered” compound URu₂Si₂? *Philosophical Magazine*, vol. 94(32-33) (Aug. 2014), pp. 3820–3837 (cit. on p. 20).
DOI: 10.1080/14786435.2014.952256.
- [103] T. DAS: Spin-orbit density wave induced hidden topological order in URu₂Si₂. *Scientific Reports*, vol. 2 (Aug. 2012), p. 596 (cit. on pp. 20, 81).
DOI: 10.1038/srep00596.
- [104] T. T. M. PALSTRA et al.: Superconducting and Magnetic Transitions in the Heavy-Fermion System URu₂Si₂. *Phys. Rev. Lett.* Vol. 55(24) (Dec. 1985), pp. 2727–2730 (cit. on p. 20).
DOI: 10.1103/PhysRevLett.55.2727.

- [105] J. MYDOSH and P. OPPENEER: Hidden order behaviour in URu₂Si₂ (A critical review of the status of hidden order in 2014). *Philosophical Magazine*, vol. 94(32-33) (May 2014), pp. 3642–3662 (cit. on p. 20).
DOI: 10.1080/14786435.2014.916428.
- [106] V. TRIPATHI, P. CHANDRA, and P. COLEMAN: Sleuthing hidden order. *Nature Physics*, vol. 3 (Feb. 2007), pp. 78–80 (cit. on p. 20).
DOI: 10.1038/nphys524.
- [107] T. DAS: Interaction Induced Staggered Spin-Orbit Order in Two-Dimensional Electron Gas. *Phys. Rev. Letters*, vol. 109(24) (Dec. 2012), p. 246406 (cit. on pp. 20, 21, 81).
DOI: 10.1103/PhysRevLett.109.246406.
- [108] T. DAS: Staggered Spin-Orbit Order: A New Paradigm of Broken Symmetry Phase of Matter. *Journal of Superconductivity and Novel Magnetism*, vol. 26(5) (May 2013), pp. 1673–1677. ISSN: 1557-1947 (cit. on p. 20).
DOI: 10.1007/s10948-012-2008-0.
- [109] T. DAS: Tuning directional dependent metal–insulator transitions in quasi-1D quantum wires with spin–orbit density wave instability. *Journal of Physics: Condensed Matter*, vol. 28(29) (June 2016), p. 294001 (cit. on pp. 20, 21).
DOI: 10.1088/0953-8984/28/29/294001.
- [110] T. DAS: A Pedagogic Review on Designing Model Topological Insulators. *Journal of the Indian Institute of Science*, vol. 96(2) (Apr. 2016), pp. 77–105 (cit. on pp. 20, 21).
URL: <http://journal.library.iisc.ernet.in/index.php/iisc/article/view/4606>.
- [111] C. TEGENKAMP et al.: Switching Between One and Two Dimensions: Conductivity of Pb-Induced Chain Structures on Si(557). *Phys. Rev. Letters*, vol. 95(17) (Oct. 2005), p. 176804 (cit. on p. 21).
DOI: 10.1103/PhysRevLett.95.176804.
- [112] C. TEGENKAMP et al.: Coupled Pb Chains on Si(557): Origin of One-Dimensional Conductance. *Phys. Rev. Letters*, vol. 100(7) (Feb. 2008), p. 076802 (cit. on pp. 21, 75, 91, 92, 101).
DOI: 10.1103/PhysRevLett.100.076802.
- [113] C. TEGENKAMP et al.: Fermi Nesting between Atomic Wires with Strong Spin-Orbit Coupling. *Phys. Rev. Letters*, vol. 109(26) (Dec. 2012), p. 266401 (cit. on pp. 21, 22, 32).
DOI: 10.1103/PhysRevLett.109.266401.
- [114] G. BINNIG, H. ROHRER, C. GERBER, and E. WEIBEL: Tunneling through a controllable vacuum gap. *Applied Physical Letters*, vol. 40 (Jan. 1982), p. 178 (cit. on p. 23).
DOI: 10.1063/1.92999.

-
- [115] G. BINNIG, H. ROHRER, C. GERBER, and E. WEIBEL: Surface Studies by Scanning Tunneling Microscopy. *Phys. Rev. Letters*, vol. 49(1) (July 1982), pp. 57–61 (cit. on p. 23).
DOI: 10.1103/PhysRevLett.49.57.
- [116] J. SCHMEIDEL: “Molekulare Elektronik: Struktur und Transportverhalten von einzelnen Ferrocen Molekülen auf Metall-Halbleiter Oberflächen”. PhD thesis. Gottfried Wilhelm Leibniz Universität Hannover, May 2011 (cit. on p. 23).
- [117] J. BARDEEN: Tunnelling from a Many-Particle Point of View. *Phys. Rev. Letters*, vol. 6 (1961), p. 57 (cit. on p. 24).
DOI: 10.1103/PhysRevLett.6.57.
- [118] J. TERSOFF and D. HAMANN: Theory and Application for the Scanning Tunneling Microscope. *Phys. Rev. Letters*, vol. 50 (1983), p. 1998 (cit. on p. 24).
DOI: 10.1103/PhysRevLett.50.1998.
- [119] J. TERSOFF and D. HAMANN: Theory of the scanning tunneling microscope. *Phys. Rev. B*, vol. 31 (1985), p. 805 (cit. on p. 24).
DOI: 10.1103/PhysRevB.31.805.
- [120] H. ZANDVLIET and A. VAN HOUSELT: Scanning Tunneling Spectroscopy. *Annual Rev. of Analytical Chemistry*, vol. 2 (2009), p. 37 (cit. on pp. 24, 25, 92).
DOI: 10.1146/annurev-anchem-060908-155213.
- [121] R. FEENSTRA, J. A. STROSCIO, and A. FEIN: Tunneling spectroscopy of the Si(111)2 × 1 surface. *Surface Science*, vol. 181(1) (1987), pp. 295–306. ISSN: 0039-6028 (cit. on pp. 25, 92).
DOI: 10.1016/0039-6028(87)90170-1.
- [122] I MICCOLI, F EDLER, H PFNÜR, and C TEGENKAMP: The 100th anniversary of the four-point probe technique: the role of probe geometries in isotropic and anisotropic systems. *Journal of Physics: Condensed Matter*, vol. 27(22) (May 2015), p. 223201 (cit. on pp. 25–27).
DOI: 10.1088/0953-8984/27/22/223201.
- [123] T. KANAGAWA et al.: Anisotropy in Conductance of a Quasi-One-Dimensional Metallic Surface State Measured by a Square Micro-Four-Point Probe Method. *Phys. Rev. Letters*, vol. 91(3) (July 2003), p. 036805 (cit. on pp. 26, 27).
DOI: 10.1103/PhysRevLett.91.036805.
- [124] F. EDLER: “Electronic transport in quasi-1D atomic wires”. PhD thesis. Gottfried Wilhelm Leibniz Universität Hannover, Apr. 2018 (cit. on pp. 27, 42, 43, 53).
DOI: 10.15488/3174.
- [125] J. W. MAYER, O. J. MARSH, G. A. SHIFRIN, and R. BARON: Ion Implantation of

- Silicon: II. Electrical Evaluation using Hall-Effect Measurements. *Canadian Journal of Physics*, vol. 45(12) (1967), pp. 4073–4089 (cit. on p. 27).
DOI: 10.1139/p67-340.
- [126] I. SHIRAKI et al.: Micro-four-point Probes in a UHV Scanning Electron Microscope for in-situ Surface-Conductivity Measurements. *Surface Review and Letters*, vol. 07(05n06) (2000), pp. 533–537 (cit. on p. 27).
DOI: 10.1142/S0218625X00000592.
- [127] N. D. ARORA, J. R. HAUSER, and D. J. ROULSTON: Electron and hole mobilities in silicon as a function of concentration and temperature. *IEEE Transactions on Electron Devices*, vol. 29(2) (Feb. 1982), pp. 292–295. ISSN: 0018-9383 (cit. on p. 28).
DOI: 10.1109/T-ED.1982.20698.
- [128] T. HIRAHARA et al.: Direct measurement of the Hall effect in a free-electron-like surface state. *Phys. Rev. B*, vol. 73 (Aug. 23, June 2006), p. 235332 (cit. on p. 29).
DOI: 10.1103/PhysRevB.73.235332.
- [129] S. S. LI: The dopant density and temperature dependence of hole mobility and resistivity in boron doped silicon. *Solid-State Electronics*, vol. 21(9) (Sept. 1978), pp. 1109–1117. ISSN: 0038-1101 (cit. on p. 29).
DOI: 10.1016/0038-1101(78)90345-3.
- [130] T. LICHTENSTEIN: “Plasmons in Gold-Induced Quantum Wires”. PhD thesis. Gottfried Wilhelm Leibniz Universität Hannover, Aug. 2017 (cit. on p. 30).
URL: <https://edocs.tib.eu/files/e01dh17/896515478.pdf>.
- [131] D. WOODRUFF and T. DELCHAR: *Modern techniques of surface science*. Ed. by R. W. CAHN, E. A. DAVIS, and I. M. WARD. Cambridge Solid State Science Series. Cambridge University Press, 1986 (cit. on p. 30).
- [132] M. SEAH and W. DENCH: Quantitative Electron Spectroscopy of Surfaces: A Standard Data Base for Electron Inelastic Mean Free Paths in Solids. *Surface Interface Analysis*, vol. 1 (1979), p. 2 (cit. on p. 30).
DOI: 10.1002/sia.740010103.
- [133] M. HORN-VON HOEGEN: Growth of semiconductor layers studied by spot profile analysing low energy electron diffraction. *Zeitschrift für Kristallographie*, vol. 214 (1999), p. 591 (cit. on pp. 30, 49).
DOI: 10.1524/zkri.1999.214.10.591and10.1524/zkri.1999.214.11.684.
- [134] H. HERTZ: Ueber einen Einfluss des ultravioletten Lichtes auf die electrische Entladung. *Annalen der Physik*, vol. 267(8) (1887), pp. 983–1000 (cit. on p. 31).
DOI: 10.1002/andp.18872670827.

-
- [135] W. HALLWACHS: Ueber den Einfluss des Lichtes auf electrostatisch geladene Körper. *Annalen der Physik*, vol. 269(2) (1888), pp. 301–312 (cit. on p. 31).
DOI: 10.1002/andp.18882690206.
- [136] A. EINSTEIN: Über einen die Erzeugung und Verwandlung des Lichtes betreffenden heuristischen Gesichtspunkt. *Annalen der Physik*, vol. 322(6) (1905), pp. 132–148 (cit. on p. 31).
DOI: 10.1002/andp.19053220607.
- [137] U. FANO: Spin Orientation of Photoelectrons Ejected by Circularly Polarized Light. *Phys. Rev.* Vol. 178 (1969), p. 131 (cit. on p. 31).
DOI: 10.1103/PhysRev.178.131.
- [138] U. FANO: Spin-orbit coupling: a weak force with conspicuous effects. *Comment. At. Mol. Phys.* Vol. 2 (1970), p. 30 (cit. on p. 32).
- [139] Y. A. BYCHKOV and E. I. RASHBA: Properties of a 2D electron gas with lifted spectral degeneracy. *JETP Letters*, vol. 39(2) (Jan. 1984), pp. 78–81 (cit. on p. 32).
DOI: 10.1088/0022-3719/17/33/015.
- [140] Y. A. BYCHKOV and E. I. RASHBA: Oscillatory effects and the magnetic susceptibility of carriers in inversion layers. *Journal of Physics C: Solid State Physics*, vol. 17(33) (1984), p. 6039 (cit. on p. 32).
DOI: 10.1088/0022-3719/17/33/015.
- [141] R. GROSS and A. MARX: *Festkörperphysik*. 2. Auflage. De Gruyter Oldenbourg, Berlin, Boston, 2014. ISBN: 978-3-11-035869-8 (cit. on p. 32).
DOI: 10.1524/9783110358704.
- [142] L. PETERSEN and P. HEDEGÅRD: A simple tight-binding model of spin-orbit splitting of sp-derived surface states. *Surface Science*, vol. 459(1) (July 2000), pp. 49–56. ISSN: 0039-6028 (cit. on p. 32).
DOI: 10.1016/S0039-6028(00)00441-6.
- [143] C. BRAND et al.: Spin-resolved band structure of a densely packed Pb monolayer on Si(111). *Phys. Rev. B*, vol. 96(3) (July 2017), p. 035432 (cit. on pp. 32, 67, 84).
DOI: 10.1103/PhysRevB.96.035432.
- [144] S. VAJNA et al.: Higher-order contributions to the Rashba-Bychkov effect with application to the Bi/Ag(111) surface alloy. *Phys. Rev. B*, vol. 85 (Augs. 7, Feb. 2012), p. 075404 (cit. on p. 32).
DOI: 10.1103/PhysRevB.85.075404.
- [145] K. SHANAVAS: Overview of theoretical studies of Rashba effect in polar perovskite surfaces. *Journal of Electron Spectroscopy and Related Phenomena*, vol. 201 (2015).

- Special issue on electron spectroscopy for Rashba spin-orbit interaction, pp. 121–126.
ISSN: 0368-2048 (cit. on p. 33).
DOI: 10.1016/j.elspec.2014.08.005.
- [146] R. FEDER: *Polarized Electrons in Surface Physics*. Ed. by R. FEDER. World Scientific, Singapore, 1985. Chap. Principles and Theory of Electron Scattering and Photoemission (cit. on pp. 32, 34).
- [147] I. KIRSCHNER: *Polarized Electrons at Surfaces*. Ed. by G. HÖHLER. Vol. 106. Springer Verlag, Heidelberg, 1985 (cit. on p. 32).
- [148] E. TAMURA, W. PIEPKE, and R. FEDER: New Spin-Polarization Effect in Photoemission from Nonmagnetic Surfaces. *Phys. Rev. Lett.* Vol. 59 (1987), p. 934 (cit. on pp. 32, 34).
DOI: 10.1103/PhysRevLett.59.934.
- [149] E. TAMURA and R. FEDER: Spin Polarization in Normal Photoemission by Linearly Polarized Light from Nonmagnetic (001) Surfaces. *Europhys. Lett.* Vol. 16 (1991), p. 695 (cit. on pp. 32, 34).
DOI: 10.1209/0295-5075/16/7/015.
- [150] E. TAMURA, W. PIEPKE, and R. FEDER: Spin-resolved photoemission from (111) surfaces of Pd, Ir and Pt by circularly polarized light: theory and comparison with experiments. *J. Phys.: Condens. Matter*, vol. 1 (1989), p. 6469 (cit. on p. 32).
DOI: 10.1088/0953-8984/1/36/015.
- [151] U. HEINZMANN and J.-H. DIL: Spin-orbit -induced photoelectron spin polarization in angle-resolved photoemission from both atomic and condensed matter targets. *J. Phys.: Condens. Matter*, vol. 24 (Apr. 2012), p. 173001 (cit. on p. 33).
DOI: 10.1088/0953-8984/24/17/173001.
- [152] U. HEINZMANN and N. A. CHEREPKOV: *VUV and Soft X-ray Photoionization*. Ed. by U. BECKER and D. A. SHIRLEY. Physics of Atoms and Molecules. Boston, MA: Springer, 1996. Chap. Spin Polarization in Photoionization and references therein, pp. 521–559. ISBN: 978-1-4613-0315-2 (cit. on p. 33).
DOI: 10.1007/978-1-4613-0315-2_15.
- [153] U. HEINZMANN: An apparatus for the production of circularly polarized VUV radiation. *J. Phys. E: Sci. Instrum.* Vol. 10 (1977), p. 1001 (cit. on p. 33).
DOI: 10.1088/0022-3735/10/10/016.
- [154] H. MAASS: “Spin-dependence of angle-resolved photoemission from spin-orbit split surface states”. PhD thesis. Julius-Maximilians-Universität Würzburg, 2016 (cit. on p. 33).
URL: https://opus.bibliothek.uni-wuerzburg.de/files/15102/Maass_Henriette_spin-orbit_split.pdf.

-
- [155] J. SÁNCHEZ-BARRIGA et al.: Photoemission of Bi₂Se₃ with Circularly Polarized Light: Probe of Spin Polarization or Means for Spin Manipulation? *Phys. Rev. X*, vol. 4 (2014), p. 011046 (cit. on p. 33).
DOI: 10.1103/PhysRevX.4.011046.
- [156] F. MEIER et al.: Interference of spin states in photoemission from Sb/Ag(111) surface alloys. *J. Phys.: Condens. Matter*, vol. 23 (2011), p. 072207 (cit. on p. 34).
DOI: 10.1088/0953-8984/23/7/072207.
- [157] F. MEIER et al.: Quantitative vectorial spin analysis in angle-resolved photoemission: Bi/Ag(111) and Pb/Ag(111). *Phys. Rev. B*, vol. 77 (2008), p. 165431 (cit. on p. 34).
DOI: 10.1103/PhysRevB.77.165431.
- [158] K. YAJI et al.: Spin-dependent quantum interference in photoemission process from spin-orbit coupled states. *Nat. Comm.* Vol. 8 (2017), p. 14588 (cit. on pp. 34, 35).
DOI: 10.1038/ncomms14588.
- [159] C. JOZWIAK et al.: Photoelectron spin-flipping and texture manipulation in a topological insulator. *Nat. Phys.* Vol. 9 (2013), p. 293 (cit. on p. 35).
DOI: 10.1038/NPhys2572.
- [160] C. M. SCHNEIDER and J. KIRSCHNER: Spin- and angle-resolved photoelectron spectroscopy from solid surfaces with circularly polarized light. *Critical Reviews in Solid State and Materials Sciences*, vol. 20(3) (1995), pp. 179–283 (cit. on p. 36).
DOI: 10.1080/10408439508241252.
- [161] J. GARBE and J. KIRSCHNER: Spin-dependent photoemission intensities from platinum (111). *Phys. Rev. B*, vol. 39 (Auszg. 14, May 1989), pp. 9859–9864 (cit. on p. 36).
DOI: 10.1103/PhysRevB.39.9859.
- [162] F. FRENTZEN et al.: Spin-resolved photoemission by circularly polarized light from Au on Ag(111): experiment and theory. *Zeitschrift für Physik B Condensed Matter*, vol. 100(4) (Dec. 1996), pp. 575–582. ISSN: 1431-584X (cit. on p. 36).
DOI: 10.1007/s002570050164.
- [163] RHK TECHNOLOGY, INC.: *UHV 700 – Variable Temperature Ultra-High Vacuum Scanning Tunneling Microscope – User’s Guide*. Document Version 1.0. July 2006 (cit. on pp. 37, 38).
- [164] J. P. IBE et al.: On the electrochemical etching of tips for scanning tunneling microscopy. *Journal of Vacuum Science & Technology A*, vol. 8(4) (1990), pp. 3570–3575 (cit. on p. 37).
DOI: 10.1116/1.576509.
- [165] A.-S. LUCIER: “Preparation and Characterization of Tungsten Tips Suitable for Molec-

- ular Electronics Studies”. MA thesis. McGill University, Montréal, Canada, Feb. 2004 (cit. on p. 37).
URL: <http://www.physics.mcgill.ca/~peter/theses/lucier.pdf>.
- [166] SCIENTA OMICRON GMBH: *LT STM User’s Guide*. Document Version 4.2. Aug. 2015 (cit. on pp. 38, 39).
- [167] STANFORD RESEARCH SYSTEMS, INC.: *Model SR830 – DSP Lock-In Amplifier – User’s Guide*. Document Version 2.5. Oct. 2011 (cit. on p. 39).
- [168] M. HOESCH et al.: Spin-polarized Fermi surface mapping. *J. Electron Spectrosc. Relat. Phenom.* Vol. 124 (2002), p. 263 (cit. on pp. 39–41).
DOI: 10.1016/S0368-2048(02)00058-0.
- [169] N. F. MOTT: The scattering of fast electrons by atomic nuclei. *Proc. R. Soc. Lond. A*, vol. 124 (1929), p. 425 (cit. on p. 40).
DOI: 10.1098/rspa.1929.0127.
- [170] V. N. PETROV, M. LANDOLT, M. S. GALAKTIONOV, and B. V. YUSHENKOV: A new compact 60 kV Mott polarimeter for spin polarized electron spectroscopy. *Rev. Sci. Instrum.* Vol. 68 (1997), p. 4385 (cit. on p. 40).
DOI: 10.1063/1.1148400.
- [171] M. FANCIULLI: “Spin polarization and attosecond time delay in photoemission from solids”. PhD thesis. École polytechnique fédérale de Lausanne, 2018 (cit. on p. 40).
URL: https://infoscience.epfl.ch/record/255089/files/EPFL_TH8469.pdf.
- [172] N. SHERMAN: Coulomb Scattering of Relativistic Electrons by Point Nuclei. *Phys. Review*, vol. 103 (Ausc. 6, Sept. 1956), pp. 1601–1607 (cit. on p. 41).
DOI: 10.1103/PhysRev.103.1601.
- [173] J. BARINGHAUS: “Mesoscopic transport phenomena in epitaxial graphene nanostructures: a surface science approach”. PhD thesis. Gottfried Wilhelm Leibniz Universität Hannover, Nov. 2015 (cit. on p. 42).
URL: <https://edocs.tib.eu/files/e01dh15/839487312.pdf>.
- [174] H. JAKSCH and J.-P. VERMEULEN: New Developments in Gemini® Fesem Technology. *Microscopy Today*, vol. 13(2) (Mar. 2005), 8–11 (cit. on p. 42).
DOI: 10.1017/S1551929500051397.
- [175] C. SEIDEL: “Die Oberfläche von atomaren Wolframspitzen zur Anwendung in Tunnelprozessen - eine Analyse mit Feldionenmikroskopie”. MA thesis. Gottfried Wilhelm Leibniz Universität Hannover, Dec. 2014 (cit. on p. 42).
- [176] J. A. WOOD et al.: Iridium single atom tips fabricated by field assisted reactive gas

-
- etching. *Applied Surface Science*, vol. 367 (Mar. 2016), pp. 277–280. ISSN: 0169-4332 (cit. on p. 42).
DOI: 10.1016/j.apsusc.2016.01.080.
- [177] M. KAWAJI, S. BABA, and A. KINBARA: Superstructures of submonolayer indium films on silicon (111)7 surfaces. *Applied Physics Letters*, vol. 34(11) (June 1979), pp. 748–749 (cit. on p. 47).
DOI: 10.1063/1.90659.
- [178] K. JITHESH, GOVIND, U. WAGHMARE, and S. SHIVAPRASAD: Experimental deduction of In/Si(111) 2D phase diagram and ab initio DFT modeling of $2\sqrt{3}$ phase. *Applied Surface Science*, vol. 256(2) (Oct. 2009). *Physics at Surfaces and Interface*, pp. 348–352 (cit. on p. 47).
DOI: 10.1016/j.apsusc.2009.04.123.
- [179] W. R. INC.: *Mathematica, Version 11.3*. Champaign, IL, 2018 (cit. on p. 53).
- [180] M. ABOELFOTOH: Temperature dependence of the Schottky-barrier height of tungsten on n-type and p-type silicon. *Solid-State Electronics*, vol. 34(1) (Jan. 1991), pp. 51–55. ISSN: 0038-1101 (cit. on p. 55).
DOI: [https://doi.org/10.1016/0038-1101\(91\)90200-I](https://doi.org/10.1016/0038-1101(91)90200-I).
- [181] U. ÖZDEMİR: *Rastertunnelmikroskopie Messungen an Sn/Si(111)*. Bachelor’s Thesis, Leibniz Universität Hannover. 2016 (cit. on p. 57).
- [182] M. JÄGER et al.: α -Sn phase on Si(111): Spin texture of a two-dimensional Mott state. *Phys. Rev. B*, vol. 98(16) (Oct. 2018), p. 165422 (cit. on pp. 57, 71, 79).
DOI: 10.1103/PhysRevB.98.165422.
- [183] T. ICHIKAWA: Structural study of ultrathin Sn layers deposited onto Ge(111) and Si(111) surfaces by RHEED. *Surface Science*, vol. 140(1) (1984), pp. 37–63. ISSN: 0039-6028 (cit. on pp. 57, 58, 73).
DOI: 10.1016/0039-6028(84)90380-7.
- [184] P. ESTRUP and J MORRISON: Studies of monolayers of lead and tin on Si(111) surfaces. *Surface Science*, vol. 2 (1964), pp. 465–472. ISSN: 0039-6028 (cit. on pp. 57, 77).
DOI: 10.1016/0039-6028(64)90088-3.
- [185] C. TÖRNEVIK et al.: Adsorption of Sn on Si(111) 7×7 : reconstructions in the monolayer regime. *Surface Science*, vol. 314(2) (1994), pp. 179–187. ISSN: 0039-6028 (cit. on pp. 58, 59, 73, 77).
DOI: 10.1016/0039-6028(94)90005-1.
- [186] G. PROFETA et al.: Structural and electronic properties of the Sn/Si(111) $\sqrt{3} \times \sqrt{3}R30^\circ$ surface. *Phys. Rev. B*, vol. 62(3) (2000), pp. 1556–1559 (cit. on p. 58).
DOI: 10.1103/PhysRevB.62.1556.

- [187] C. TÖRNEVIK, M. HAMMAR, N. G. NILSSON, and S. A. FLODSTRÖM: Epitaxial growth of Sn on Si(111): A direct atomic-structure determination of the $(2\sqrt{3} \times 2\sqrt{3})R30^\circ$ reconstructed surface. *Phys. Rev. B*, vol. 44(23) (1991), pp. 13144–13147 (cit. on pp. 58, 73).
DOI: 10.1103/PhysRevB.44.13144.
- [188] X. LIN, I. CHIZHOV, H. MAI, and R. WILLIS: Scanning tunneling spectroscopy examination of surface electronic structures of Si(111) $(2\sqrt{3} \times 2\sqrt{3})30^\circ$ -Sn surface. *Applied Surface Science*, vol. 104-105 (1996). Proceedings of the Fifth International Conference on the Formation of Semiconductor Interfaces, pp. 223–227. ISSN: 0169-4332 (cit. on p. 58).
DOI: 10.1016/S0169-4332(96)00148-1.
- [189] L. OTTAVIANO et al.: Structural and electronic properties of the Sn/Si(111)- $(2\sqrt{3} \times 2\sqrt{3})R30^\circ$ surface revised. *Surface Science*, vol. 554(2) (2004), pp. 109–118. ISSN: 0039-6028 (cit. on p. 58).
DOI: 10.1016/j.susc.2004.02.019.
- [190] S. YI et al.: Atomic and electronic structure of doped Si(111) $(2\sqrt{3} \times 2\sqrt{3})R30^\circ$ -Sn interfaces. *Phys. Rev. B*, vol. 97(19) (May 2018), p. 195402 (cit. on pp. 58, 73).
DOI: 10.1103/PhysRevB.97.195402.
- [191] K. CONWAY et al.: The structure of the Si(111) $(\sqrt{3} \times \sqrt{3})R30^\circ$ -Sn surface determined using X-ray diffraction. *Surface Science*, vol. 215(3) (1989), pp. 555–565. ISSN: 0039-6028 (cit. on p. 58).
DOI: 10.1016/0039-6028(89)90275-6.
- [192] H. MORIKAWA, I. MATSUDA, and S. HASEGAWA: STM observation of Si(111)- $\alpha - \sqrt{3} \times \sqrt{3}$ -Sn at low temperature. *Phys. Rev. B*, vol. 65(20) (2002), p. 201308 (cit. on pp. 59, 60).
DOI: 10.1103/PhysRevB.65.201308.
- [193] L. OTTAVIANO, A. V. MELECHKO, S. SANTUCCI, and E. W. PLUMMER: Direct Visualization of Defect Density Waves in 2D. *Phys. Rev. Letters*, vol. 86(9) (2001), pp. 1809–1812 (cit. on p. 59).
DOI: 10.1103/PhysRevLett.86.1809.
- [194] R. I. G. UHRBERG et al.: Electronic structure of Sn/Si(111) $\sqrt{3} \times \sqrt{3}$: Indications of a low-temperature phase. *Phys. Rev. B*, vol. 62(12) (2000), pp. 8082–8086 (cit. on pp. 59, 60).
DOI: 10.1103/PhysRevB.62.8082.
- [195] L. OTTAVIANO, M. CRIVELLARI, L. LOZZI, and S. SANTUCCI: STM investigation of the α -Sn/Si(111) phase at 120 K. *Surface Science*, vol. 445(1) (2000), pp. L41–L46. ISSN: 0039-6028 (cit. on p. 59).
DOI: 10.1016/S0039-6028(99)00974-7.

-
- [196] A. CHARRIER et al.: Contrasted electronic properties of Sn-adatom-based $(\sqrt{3} \times \sqrt{3})R30^\circ$ reconstructions on Si(111). *Phys. Rev. B*, vol. 64(11) (2001), p. 115407 (cit. on p. 59).
DOI: 10.1103/PhysRevB.64.115407.
- [197] S. JEMANDER et al.: An STM study of the surface defects of the $(\sqrt{3} \times \sqrt{3})$ -Sn/Si(111) surface. *Surface Science*, vol. 475(1) (2001), pp. 181–193. ISSN: 0039-6028 (cit. on p. 59).
DOI: 10.1016/S0039-6028(00)01100-6.
- [198] L. OTTAVIANO et al.: Mechanism of the short range ordering in a 2D binary alloy. *Surface Science*, vol. 501(1) (2002), pp. L171–L176. ISSN: 0039-6028 (cit. on p. 59).
DOI: 10.1016/S0039-6028(01)01980-X.
- [199] W. KAMINSKI et al.: Si-substitutional defects on the α -Sn/Si(111)- $(\sqrt{3} \times \sqrt{3})$ surface. *Applied Surface Science*, vol. 234(1) (2004). The Ninth International Conference on the Formation of Semiconductor Interfaces, pp. 286–291. ISSN: 0169-4332 (cit. on p. 59).
DOI: 10.1016/j.apsusc.2004.05.083.
- [200] J. M. CARPINELLI, H. H. WEITERING, and E. PLUMMER: Charge rearrangement in the $\text{Ge}_x\text{Pb}_{1-x}/\text{Ge}(111)$ interface. *Surface Science*, vol. 401(3) (1998), pp. L457–L463. ISSN: 0039-6028 (cit. on p. 59).
DOI: 10.1016/S0039-6028(98)00146-0.
- [201] J. M. CARPINELLI et al.: Surface Charge Ordering Transition: α Phase of Sn/Ge(111). *Phys. Rev. Letters*, vol. 79(15) (1997), pp. 2859–2862 (cit. on pp. 59, 60).
DOI: 10.1103/PhysRevLett.79.2859.
- [202] A. V. MELECHKO, J. BRAUN, H. H. WEITERING, and E. W. PLUMMER: Two-Dimensional Phase Transition Mediated by Extrinsic Defects. *Phys. Rev. Letters*, vol. 83(5) (1999), pp. 999–1002 (cit. on p. 59).
DOI: 10.1103/PhysRevLett.83.999.
- [203] H. H. WEITERING et al.: Defect-Mediated Condensation of a Charge Density Wave. *Science*, vol. 285(5436) (1999), pp. 2107–2110. ISSN: 0036-8075 (cit. on p. 59).
DOI: 10.1126/science.285.5436.2107.
- [204] O. CUSTANCE et al.: Low temperature phases of Pb/Si(111). *Surface Science*, vol. 482-485 (2001), pp. 1399–1405. ISSN: 0039-6028 (cit. on p. 60).
DOI: 10.1016/S0039-6028(01)00774-9.
- [205] J.-H. LEE, X.-Y. REN, Y. JIA, and J.-H. CHO: Antiferromagnetic superexchange mediated by a resonant surface state in Sn/Si(111). *Phys. Rev. B*, vol. 90(12) (Sept. 2014). supplement, p. 125439 (cit. on pp. 60–63, 65, 68, 69, 77, 79, 100).
DOI: 10.1103/PhysRevB.90.125439.

- [206] A. B. ODOBESCU, A. A. MAIZLAKH, N. I. FEDOTOV, and S. V. ZAITSEV-ZOTOV: Electronic correlation effects and Coulomb gap in the Si(111)-($\sqrt{3} \times \sqrt{3}$)-Sn surface. *Phys. Rev. B*, vol. 95(19) (May 2017), p. 195151 (cit. on pp. 60, 100). DOI: 10.1103/PhysRevB.95.195151.
- [207] J.-H. LEE, H.-J. KIM, and J.-H. CHO: Ferrimagnetic Slater Insulator Phase of the Sn/Ge(111) Surface. *Phys. Rev. Letters*, vol. 111(10) (Sept. 2013), p. 106403 (cit. on p. 60). DOI: 10.1103/PhysRevLett.111.106403.
- [208] D. I. BADRTDINOV, S. A. NIKOLAEV, M. I. KATSNELSON, and V. V. MAZURENKO: Spin-orbit coupling and magnetic interactions in Si(111):C,Si,Sn,Pb. *Phys. Rev. B*, vol. 94(22) (Dec. 2016), p. 224418 (cit. on p. 60). DOI: 10.1103/PhysRevB.94.224418.
- [209] S. HEINZE et al.: Real-Space Imaging of Two-Dimensional Antiferromagnetism on the Atomic Scale. *Science*, vol. 288(5472) (2000), pp. 1805–1808. ISSN: 0036-8075 (cit. on p. 67). DOI: 10.1126/science.288.5472.1805.
- [210] M. JÄGER et al.: Formation of Sn-Induced Nanowires on Si(557). *physica status solidi (b)*, vol. (June 2019), p. 1900152 (cit. on p. 72). DOI: 10.1002/pssb.201900152.
- [211] P. NITA, G. ZAWADZKI, M. KRAWIEC, and M. JAŁOCHOWSKI: Structural and electronic properties of double Pb chains on the Si(553)-Au surface. *Phys. Rev. B*, vol. 84(8) (Aug. 2011), p. 085453 (cit. on p. 74). DOI: 10.1103/PhysRevB.84.085453.
- [212] M. JAŁOCHOWSKI et al.: Correlation between morphology, electron band structure, and resistivity of Pb atomic chains on the Si(5 5 3)-Au surface. *Journal of Physics: Condensed Matter*, vol. 28(28) (May 2016), p. 284003. ISSN: 1361-648X (cit. on p. 74). DOI: 10.1088/0953-8984/28/28/284003.
- [213] B. HAFKE et al.: Two-dimensional interaction of spin chains in the Si(553)-Au nanowire system. *Phys. Rev. B*, vol. 94(16) (Oct. 2016), p. 161403 (cit. on p. 75). DOI: 10.1103/PhysRevB.94.161403.
- [214] J. N. CRAIN et al.: Chains of gold atoms with tailored electronic states. *Phys. Rev. B*, vol. 69(12) (Mar. 2004), p. 125401 (cit. on p. 75). DOI: 10.1103/PhysRevB.69.125401.
- [215] U. KRIEG, C. BRAND, C. TEGENKAMP, and H. PFNÜR: One-dimensional collective excitations in Ag atomic wires grown on Si(557). *J. Phys.: Condens. Matter*, vol. 25 (2013), p. 014013 (cit. on pp. 75, 77). DOI: 10.1088/0953-8984/25/1/014013.

-
- [216] M. CZUBANOWSKI et al.: Adsorbate induced refacetting: Pb chains on Si(557). *New Journal of Physics*, vol. 9(9) (Sept. 2007), pp. 338–347 (cit. on pp. 75, 81, 82, 86–89). DOI: 10.1088/1367-2630/9/9/338.
- [217] A. BASKI, S. ERWIN, and L. WHITMAN: The structure of silicon surfaces from (001) to (111). *Surface Science*, vol. 392(1) (1997), pp. 69–85. ISSN: 0039-6028 (cit. on p. 75). DOI: 10.1016/S0039-6028(97)00499-8.
- [218] A. KIRAKOSIAN et al.: Atomically accurate Si grating with 5.73 nm period. *Applied Physics Letters*, vol. 79(11) (Sept. 2001), pp. 1608–1610 (cit. on p. 75). DOI: 10.1063/1.1401788.
eprint: <https://doi.org/10.1063/1.1401788>.
- [219] H. MORIKAWA, K. S. KIM, D. Y. JUNG, and H. W. YEOM: Scanning tunneling microscopy observation of Pb-induced superstructures on Si(557). *Phys. Rev. B*, vol. 76(16) (Oct. 2007), p. 165406 (cit. on pp. 77, 83). DOI: 10.1103/PhysRevB.76.165406.
- [220] A. PERGAMENT: Metal-insulator transition: the Mott criterion and coherence length. *Journal of Physics: Condensed Matter*, vol. 15(19) (May 2003), pp. 3217–3223. ISSN: 1361-648X (cit. on p. 79). DOI: 10.1088/0953-8984/15/19/322.
- [221] M. KOPCIUSZYŃSKI et al.: Pb nanoribbons on the Si(553) surface. *Phys. Rev. B*, vol. 88(15) (Oct. 2013), p. 155431 (cit. on p. 81). DOI: 10.1103/PhysRevB.88.155431.
- [222] M. KOPCIUSZYŃSKI, P. ŁUKASIK, R. ZDYB, and M. JAŁOCHOWSKI: Ordering of the Si(553) surface with Pb atoms. *Applied Surface Science*, vol. 305 (June 2014), pp. 139–142. ISSN: 0169-4332 (cit. on p. 81). DOI: 10.1016/j.apsusc.2014.03.009.
- [223] M. KOPCIUSZYŃSKI, M. KRAWIEC, R. ZDYB, and M. JAŁOCHOWSKI: Purely one-dimensional bands with a giant spin-orbit splitting: Pb nanoribbons on Si(553) surface. *Scientific Reports*, vol. 7 (Apr. 2017), p. 46215 (cit. on p. 81). DOI: 10.1038/srep46215.
- [224] M. JÄGER: “Rastertunnelmikroskopie an niedrigdimensionalen Bleistrukturen auf Halbleiteroberflächen”. MA thesis. Leibniz Universität Hannover, Jan. 2015 (cit. on pp. 83, 85).
- [225] S. STEPANOVSKY et al.: The dense $\alpha - \sqrt{3} \times \sqrt{3}$ Pb/Si(111) phase: A comprehensive STM and SPA-LEED study of ordering, phase transitions and interactions. *Surface Science*, vol. 600(7) (2006), pp. 1417–1430. ISSN: 0039-6028 (cit. on pp. 83, 84). DOI: 10.1016/j.susc.2005.12.041.

- [226] M. HUPALO, J. SCHMALIAN, and M. C. TRINGIDES: “Devil’s Staircase” in Pb/Si(111) Ordered Phases. *Phys. Rev. Lett.* Vol. 90(21) (May 2003), p. 216106 (cit. on pp. 83, 84).
DOI: 10.1103/PhysRevLett.90.216106.
- [227] T.-L. CHAN et al.: First-principles studies of structures and stabilities of Pb/Si(111). *Phys. Rev. B*, vol. 68(4) (July 2003), p. 045410 (cit. on pp. 83, 84).
DOI: 10.1103/PhysRevB.68.045410.
- [228] L. SEEHOFER, G. FALKENBERG, D. DABOUL, and R. L. JOHNSON: Structural study of the close-packed two-dimensional phases of Pb on Ge(111) and Si(111). *Phys. Rev. B*, vol. 51(19) (May 1995), pp. 13503–13515 (cit. on pp. 83, 84).
DOI: 10.1103/PhysRevB.51.13503.
- [229] M. HUPALO et al.: Atomic models, domain-wall arrangement, and electronic structure of the dense Pb/Si(111) – $\sqrt{3} \times \sqrt{3}$ phase. *Phys. Rev. B*, vol. 66 (Oct. 2002), p. 161410 (cit. on p. 84).
DOI: 10.1103/PhysRevB.66.161410.
- [230] I.-S. HWANG, R. E. MARTINEZ, C. LIU, and J. A. GOLOVCHENKO: Soft incommensurate reconstruction on Pb/Si(111): Structure, stress modulation, and phase transition. *Phys. Rev. B*, vol. 51(15) (Apr. 1995), pp. 10193–10196 (cit. on p. 85).
DOI: 10.1103/PhysRevB.51.10193.
- [231] J. BARDEEN, L. N. COOPER, and J. R. SCHRIEFFER: Theory of Superconductivity. *Phys. Rev.* Vol. 108 (Aug. 5, Dec. 1957), pp. 1175–1204 (cit. on p. 90).
DOI: 10.1103/PhysRev.108.1175.
- [232] R. C. DYNES, J. P. GARNO, G. B. HERTEL, and T. P. ORLANDO: Tunneling Study of Superconductivity near the Metal-Insulator Transition. *Phys. Rev. Letters*, vol. 53 (Aug. 25, Dec. 1984), pp. 2437–2440 (cit. on p. 90).
DOI: 10.1103/PhysRevLett.53.2437.
- [233] T. ZHANG et al.: Superconductivity in one-atomic-layer metal films grown on Si(111). *Nature Physics*, vol. 6 (Jan. 2010), p. 104 (cit. on p. 91).
DOI: 10.1038/nphys1499.
- [234] C. CASTENMILLER et al.: Combined I(V) and dI(V)/dz scanning tunneling spectroscopy. *AIP Advances*, vol. 8(7) (July 2018), p. 075013 (cit. on p. 92).
DOI: 10.1063/1.5034422.
- [235] C. TEGENKAMP et al.: Pb nanowires on vicinal Si(111) surfaces: Effects of refacetting on transport. *Phys. Rev. B*, vol. 82(20) (Nov. 2010), p. 205413 (cit. on p. 94).
DOI: 10.1103/PhysRevB.82.205413.
- [236] A. N. MEHTA et al.: Understanding noninvasive charge transfer doping of graphene: a

comparative study. *Journal of Materials Science: Materials in Electronics*, vol. 29(7) (Apr. 2018), pp. 5239–5252. ISSN: 1573-482X (cit. on p. 102).
DOI: 10.1007/s10854-017-8443-8.

- [237] J. M. GOTTFRIED: Surface chemistry of porphyrins and phthalocyanines. *Surface Science Reports*, vol. 70(3) (Nov. 2015), pp. 259–379. ISSN: 0167-5729 (cit. on p. 102).
DOI: 10.1016/j.surfrep.2015.04.001.
- [238] J. D. BARAN and J. A. LARSSON: Inversion of the shuttlecock shaped metal phthalocyanines MPc (M = Ge, Sn, Pb)—a density functional study. *Phys. Chem. Chem. Physics*, vol. 12(23) (Apr. 2010), pp. 6179–6186 (cit. on p. 102).
DOI: 10.1039/B924421B.
- [239] D. HAO et al.: Self-assembly of manganese phthalocyanine on Pb(111) surface: A scanning tunneling microscopy study. *The Journal of Chemical Physics*, vol. 134(15) (Apr. 2011), p. 154703 (cit. on p. 102).
DOI: 10.1063/1.3579493.

Publication List

- [1] H. PFNÜR et al.: Between one and two dimensions: Pb/Si(557) close to monolayer coverage. *Surface Science*, vol. 643 (Jan. 2016). Present challenges in surface science, a special issue in honour of Dietrich Menzel, pp. 79 –86. ISSN: 0039-6028.
DOI: 10.1016/j.susc.2015.08.007.
- [2] M. JÄGER et al.: α -Sn phase on Si(111): Spin texture of a two-dimensional Mott state. *Phys. Rev. B*, vol. 98(16) (Oct. 2018), p. 165422.
DOI: 10.1103/PhysRevB.98.165422.
- [3] T. N. NGUYEN et al.: Noninvasive coupling of PbPc monolayers to epitaxial graphene on SiC(0001). *Surface Science*, vol. 686 (Aug. 2019), pp. 45 –51. ISSN: 0039-6028.
DOI: 10.1016/j.susc.2019.04.003.
- [4] M. JÄGER et al.: Formation of Sn-Induced Nanowires on Si(557). *physica status solidi (b)*, vol. (June 2019), p. 1900152.
DOI: 10.1002/pssb.201900152.

Curriculum Vitae

PERSONAL INFORMATION:

NAME Monika Jäger
DATE OF BIRTH 21.09.1990 in Neustadt am Rübenberge

EDUCATION:

Since Feb. 2015 Doctoral Studies, Gottfried Wilhelm Leibniz Universität Hannover
2012 – 2015 Master of Science, Technical Physics, Gottfried Wilhelm Leibniz Universität Hannover
 Thesis: *Rastertunnelmikroskopie an niedrigdimensionalen Bleistrukturen auf Halbleiteroberflächen*
2009 – 2012 Bachelor of Science, Physics, Georg-August-Universität Göttingen
 Thesis: *Phasendiagramm, Bildungsenthalpien und -entropien sehr dünner Palladium-Wasserstoff Schichten*
2002 – 2009 Abitur, Marion-Dönhoff-Gymnasium, Nienburg/Weser

Danksagung

An dieser Stelle möchte ich mich herzlich bei allen bedanken, die mich während der Zeit meiner Promotion unterstützt haben und damit zum Gelingen dieser Arbeit beigetragen haben.

Zuallererst ist danke ich Prof. Dr. Christoph Tegenkamp für die tolle Betreuung meiner Promotion, die vielen Diskussionen über meine Ergebnisse und die konstruktive Kritik an meinen Interpretationen, die diese Arbeit erst möglich gemacht hat.

Desweiteren möchte ich mich bei Prof. Dr. Herbert Pfnür für das Interesse am Fortgang meiner Arbeit bedanken, sowie für das Stellen von kritischen Fragen, die mir manchmal eine neue Sichtweise auf meine Daten eröffneten. Ihm und Prof. Dr. Harold Zandvliet danke ich auch sehr für die Übernahme des Korreferats dieser Arbeit.

Ein sehr großer Dank gilt allen meinen Arbeitskollegen für die angenehme Arbeitsatmosphäre und die gute Zusammenarbeit, insbesondere aber Johannes Aprojanz und Diana Slawig, die nachmittags stets Zeit für eine Kaffeepause fanden. Außerdem danke ich der gesamten Expertenrunde dafür, dass man über Physik auch mit einem Glas Bier in der Hand diskutieren kann.

Zuletzt möchte ich mich bei meiner Familie, meinen Freunden und meinem Mann Lorenz bedanken, dass sie mich während dieser Zeit stets vollkommen unterstützt haben und immer geduldig waren, wenn ich ihnen von meiner Arbeit erzählen wollte.

Vielen Dank!